# SPARSITY-BASED METHODS FOR CARDIAC MAGNETIC RESONANCE IMAGE RECONSTRUCTION AND ANALYSIS

**By**

**YANG YU**

**A dissertation submitted to the**

**Graduate School—New Brunswick**

**Rutgers, The State University of New Jersey**

**in partial fulfillment of the requirements**

**for the degree of**

**Doctor of Philosophy**

**Graduate Program in Computer Science**

**written under the direction of**

**Dimitris Metaxas**

**and approved by**

_____

_____

_____

_____

**New Brunswick, New Jersey**

**October, 2015**

## ABSTRACT OF THE DISSERTATION

# Sparsity-based Methods for Cardiac Magnetic Resonance Image Reconstruction and Analysis

**By YANG YU**

**Dissertation Director:**

**Dimitris Metaxas**

In signal processing, sparseness means that there are only small amounts of non-zero elements. This property has been widely observed in various types of signals. However, the data sparseness is hard to be regularized due to its non-convex nature. The recent development of the compressed sensing technique builds a theoretical connection between the sparse constraint and its convex relaxation. This discovery motivates us to explore different types of sparse properties for the generation and analysis of the cardiac magnetic resonance images (MRIs). In this work, our proposed a series of sparse optimization algorithms have been applied to cardiac image reconstruction, segmentation and motion tracking problems for fast and robust analyzing the cardiac data.

The cardiac imaging is a challenging problem to MRI due to its fast motion. We proposed a novel calibration-less algorithm to accelerate the generation of dynamic MR images with both compressed sensing and parallel imaging. In addition

to the temporal signal, which usually provides more data redundancy than spatial signals, the strong correlations among signals from different coils are utilized to form joint sparse constraints. A general optimization framework is presented to solve the problem under different types of temporal sparse constraints efficiently.

We then apply the sparse constraint to the cardiac muscle motion tracking. The 3D deformable heart model is built by simulating its motion in a cardiac cycle based on tagged MRI. The tagged MR data is widely used to reveal the internal myocardial motion. However, the automated tagging line detection results are very noisy due to the poor image quality. To alleviate this issue, we introduce a new family of sparse deformable models based on the sparseness of the detection noise. Our new models track the heart motion robustly, and the resulting strains are consistent with those calculated from manual labels.

# Acknowledgements

I would like to sincerely thank all those people who have helped me get to this point in my academic career. First and foremost, I would like to thank my Ph.D. advisor Professor Dimitris Metaxas. His insight into computer vision greatly influenced my way of doing research. His enthusiasm on research encouraged me to overcome many difficulties along years. I simply would not have been able to get this point otherwise.

I would also like to thank the other members of my doctoral committee: Prof. Ahmed Elgammal, Prof. Kostas bekris, and Prof. Xiaolei Huang (Lehigh University) for their advice, help and valuable suggestions regarding this dissertation. It is an honor for me to have each of them serves in my committee.

Special thanks to all other professors and researchers with whom I collaborated to produce the work presented in this thesis, as well as work published or presented elsewhere. More specially, I thank Prof. Leon Axel (New York Univesrity) for his help on cardiac-related topics. He has provided very useful insight and advice in several of my papers, and I really appreciate his thoughtful input.

I also need to thank all my other professors at Rutgers (in alphabetical order) who, through their courses, contributed to my success by enriching my brain with valuable knowledge and skills, which I applied directly or indirectly to my research: Prof. Eric Allender, Prof. Alex Borgida, Prof. Apostolos Gerasoulis, Prof. Louis Steinberg, who supervised me while I was a Teaching Assistant, Prof. Michael Fredman, Prof. Casimir Kulikowski, Prof. Badri Nath, Prof. Vladimir Pavlovic, Prof. Gerard Richter, and Prof. Mario Szegedy.

I would like to acknowledge my labmates at CBIM, without whom, much of the work in this thesis would have been impossible.

Lastly, I acknowledge that in the course of my study, while making progress towards my Ph.D. I have published to various conferences and journals a large portion of the work, which I collectively present in a unified fashion in this thesis [120, 121, 122, 123, 125, 126].

# Dedication

This dissertation is dedicated to my parents for their endless love and support.

# Table of Contents

# List of Tables

# List of Illustrations

# Chapter 1
# Introduction

Cardiovascular disease (CVD), also called heart disease, is the leading cause of death globally. The number of deaths resulted from CVD keeps increasing in recent years from 12.3 million deathes (25.8%) in 1990 to 17.3 million (31.5%) in 2013. Cardiovascular disease is also a great burden to the United States. About 610,000 people die of heart disease in US every year, which is 1 in every 4 deaths. Meanwhile, there are about 735,000 Americans have a heart attack every year. This makes CVD also a major cause of disability [68].

Like many other diseases, the heart attacks are preventable if people act early enough. There are several major warning signs and symptoms for heart attacks, such as chest pain or discomfort, upper body pain or discomfort in the arms, back neck, jaw, or upper stomach, shortness of breath, and nausea, lightheadedness, or cold sweats. However, most of these symptoms are mistaken for less severe problems. People may think they are just too tired, and miss the chances of early actions. As a result, there are about 47% of sudden cardiac deaths occur outside a hospital. Therefore, it is critical to provide easy-to-use cardiac function examination tools to the potential patients.

## 1.1 Cardiac Imaging

Cardiac imaging is a technique that produces images of the heart structure and motion directly. It provides visual information about the heart that help doctors to

localize pathologies and evaluate the need for further treatment. Nowadays, there are a number of techniques available for cardiac imaging. The most frequently used 3D cardiac imaging methods are Echocardiography, Computed Tomography (CT) and Magnetic Resonance Imaging (MRI). Different modalities have their intrinsic advantages and disadvantages for cardiac imaging.

Echocardiography uses ultrasound to create images of the heart. It is one of the most widely used diagnostic tests in cardiology. It provides a relatively low cost method to visualize the heart motion in real-time. The ultrasound equipments are more compact than the current CT and MRI systems. Meanwhile, the ultrasonography is generally considered a safe imaging modality. This makes echocardiography a good choice for preliminary cardiac examination. However, image quality of echocardiography is often worse than CT and MRI. It is hard to extract fine cardiac structures from ultrasound images.

Cardiac CT provides much better spatial resolution of the heart imaging. The recent developments on cardiac CT allow a multi-detector CT scanner to successfully capture the detailed endocardial structures, including the papillary muscles and trabeculae. However, the radiation and contrast exposures of cardiac CT are always sources of significant concern. X-radiation (X-ray) is the fundamental tool for CT imaging. Multiple times of X-ray imaging are required in order to acquire a complete representation of a cardiac model. Therefore, cardiac CT can result in a relatively high radiation exposure. By comparison, each cardiac CT scan carried out is equivalent to approximately 100-600 chest X-rays or over 3 years of background radiation. People commonly concern about the possibility of an increased cancer risk due to the high radiation doses, and are likely to against the risk if there is not a significant health problem. The iodine-containing contrast agent may be used to improve the image quality for cardiac CT. However, the contrast is harmful to hyperthyroidism and renal function. Meanwhile, some people have the contrast

agent allergy. All these adverse effects prevent cardiac CT from becoming routine in clinical practice.

Cardiac MRI is a more established technique for cardiac imaging [35, 44]. It provides good spatial and temporal resolution of the heart in a whole cardiac cycle. The anatomical and functional information about the heart is generated without the need for contrast medium or invasive techniques. The magnetic field, which is the main energy source of MRI, is considered safe for most people, except patients have implant devices, such as artificial cardiac pacemaker. Although there are several good properties for MRI as mentioned above, it requires a long acquisition time to produce good images. One common practice for cardiac imaging is using retrospective electrocardiography (ECG) gating. In this technique, each portion of the heart is imaged more than once while an ECG trace is recorded. The ECG is then used to correlated the MRI data with their corresponding phases of cardiac contraction. Once this correlation is complete, the corresponding data are combined together to reconstruct the frame at each phase. During the acquisition of these cardiac cycles, the patients are required to hold their breath to reduce any additional movement other than heart. The movement due to respiration will produce image artifacts similar to motion blur. The whole imaging process will take tens of seconds. The whole MRI procedure requires several times of breath holding like this, which may be very challenging for old and weak patients. Therefore, it will help many patients if we can reduce or even remove the requirements for breath holding for cardiac MRI.

## 1.2 Cardiac MRI Reconstruction and Analysis

Cardiac MRI becomes a more important heart disease diagnosis tool in recent years, since it provides accurate and reproducible assessment of global and ventricular regional function. In this thesis, we will focus on the cardiac MRI data and work on the problem of better reconstruction and analysis of the cardiac images from various aspects.

The MRI reconstruction becomes an active area in recent year due to the development of compressed sensing techniques [11, 12, 13]. The single MRI image reconstruction has been used as the initial sample to demonstrate the power of compressed sensing for sparse signal reconstruction [58, 59]. Cardiac MRI presents additional problem for MRI reconstruction. First, a sequence of dynamic cardiac images are required to reveal the motion properties of the heart. Second, the parallel imaging technique is widely used in current cardiac imaging system. The dynamic MRI data, like cardiac motion introduce the temporal dimension to the data. This additional dimension normally contains more redundant information than the spatial dimensions since most organs deform smoothly along time or even stay still. This observation is also true for natural images, where the videos are more likely to have higher compressed rates than images. In this thesis, we exploit the temporal sparse constraints to reconstruct the dynamic MR image with higher accuracy. The parallel MR imaging technique is widely used on modern MRI system, while its special properties have not been well studied for compressed sensing based MRI reconstruction. In addition to the sparse constraints on single MRI image, the relation among different sensors can be further modeled with structured sparse constraint and solved collaboratively. By combining the techniques mentioned above, we have not only improved the reconstruction algorithm for dynamic cardiac imaging, but also allow the patient to breath normally during the

MRI acquisition, which makes the cardiac MRI available to more patients under serious condition.

As more and more MRI images are collected, one critical question is how to effectively utilize the images for clinical diagnosis. The qualitative evaluation requires rich experience from domain expert, while the quantitative evaluation often requires tedious labelling to get good estimation. Therefore, an automatical system to estimate key cardiac measurements based on image information is very important for promoting the cardiac MRI. In this thesis, we present a cardiac MR image analysis system to estimate the key heart motion properties. The system uses the routine 2D cardiac MRI images as input, and generate a 3D left ventricle model based on our proposed sparse deformable models, which reveals the local heart kinetic properties dynamically.

## 1.3 Main Contribution

The main contributions of this thesis are summarized as following:

1. We have proposed a novel reconstruction algorithm for dynamic parallel MRI. The correlations among signals from multiple coils are exploited with structured sparse constraints. The optimization problems under different temporal sparse regularizers are solved under our uniform framework with quadratic convergence rate. The proposed method is extended to reconstruct the cardiac MR images with respiration motions.

2. We have built a complete 3D left ventricle (LV) motion analysis system based 2D cardiac images. The 3D static LV model is built based on 2D cardiac images with arbitrary directions. Then the cardiac motion are first estimated on all 2D slices based on tagging lines, and then the motion information on 2D

slices drives the 3D LV deformable model. The global and local strains are estimated based on the LV deformation.

3. Sparse deformable models are proposed to robustly estimate the 3D heart motion based on noisy observations. Various types of noise may be produced during the early steps of cardiac MR image processing. The sparse deformable models decompose the noise as Gaussian noise and sparse outliers and solve the problem with sparsity based constraints.

## 1.4 Organization

The reminder of this thesis is organized as follows.

Chapter 2 first reviews the compressed sensing technique and its application to MRI. Then our proposed structured sparse model is introduced in detail to solve dynamic parallel MRI for heart. A new framework is present to solve this problem. Finally, the method is extended for breathing-free cardiac MRI.

Chapter 3 presents our cardiac image analysis system in detail. The system contains the following components: the heart segmentation, the tagging line motion tracking, the 3D LV deformation reconstruction, and the motion feature analysis.

Chapter 4 introduces the sparse deformable models for motion tracking. The method is then used on cardiac motion analysis to reconstruct 3D deformable models.

Finally, we summarized the contributions of this work, along with a discussion of limitations and future work in Chapter 5.

# Chapter 2

# Calibrationless Parallel Dynamic MRI with Joint Temporal Sparsity

In this chapter, we propose a novel calibrationless method for parallel dynamic magnetic resonance imaging (MRI) reconstruction, which overcomes the limitations posed by traditional MRI reconstruction methods that require accurate coil calibration. Thus, calibrationless methods, which remove the requirement of coil sensitivity profiles for MRI reconstruction, are suitable for dynamic MRI. Dynamic MRI contains rich temporal redundant information, i.e., the pixel intensities change smoothly over time. This property can be modeled as various types of temporal sparse priors, in the Fourier transform domain, or in the image domain using finite differences. In addition, the temporally changing patterns of pixels are similar in the various coils, since their signals are different due to the coil sensitivity profiles. Therefore, we model the parallel dynamic MRI problems as joint temporal sparsity tasks, and develop a class of algorithms to solve them efficiently. Experiments on parallel dynamic MRI datasets demonstrate that our proposed methods outperform the state-of-the-art parallel MRI reconstruction algorithms.

## 2.1 Compressed Sensing in MRI

Information theory is considered founded by Claude Shannon due to his fundamental work in this area. One of his main contribution is the Shannon sampling theory [90]. It expresses the sampling rate must be at least twice the maximum

frequency present in the signal to reconstruct the original function. This theory guides the development of almost all types of digital imaging devices, including the MRI machine. The sampling rate of MRI is considered cannot be improved based on the sampling theory, since it has already touched the boundary. However, the theory does not rule out that the sampling rate can be lower than the bound it provides when the signal is under additional constraint. People did not find any non-trivial constraint that is general enough for all image data until a recent experiment with surprisingly positive results. Researchers found that the synthetic image with partial Fourier domain samples can be almost perfectly reconstructed under total variation regularization. This discover motivates researchers to find a large category of constraints and establish a new research area, compressed sensing.

The key idea of compressed sensing is exploiting the sparsity of the signal. The theory states that the sparse signal can be recovered from far fewer samples than required by the Shannon sampling theorem [90], where the sparse signal means that the signal has only a few non-zero terms. In a $n$-dimensional space, a vector is called $k$-sparse vector if it has only $k$ non-zero elements. Intuitively, the sparse signals lay on only a group of orthogonal $k$-dimensional subspaces embedded in the $n$-dimensional space. They are definitely more complex than a given $k$-dimensional subspace, since the position of the non-zero terms are unknown. However, they are proved to be much simpler than the full $n$-dimensional vector when $k \ll n$. The position of one non-zero term can be encoded with $O(\log(n))$ bits and its value can be encoded with $O(1)$ bit. Therefore, a $k$-sparse vector can be encoded with length $O(k + k\log(n))$ bit by combining all the position and value information of the $k$ non-zero terms. This representation is more compact than the full $n$-dimensional signal when $k$ is small enough. Although a trivial method is present to encode $k$-sparse signal with a compact format, the representation is not

very interest. This is because that the position of non-zero term is hard to locate. A exhaust search may be required to fined the non-zero positions. This means that the cost is not reduced for data acquisition. The theory of compressed sensing is established based on the definition of a group of measurements, which is used to encode the sparse signal, and reconstruct the sparse signal based on these measurements.

Assuming we expect to reconstruct a signal $\mathbf{z} \in \mathbb{R}^n$, and know only a group of linear measurements $\mathbf{y} \in \mathbb{R}^m$, where $m < n$, the linear relation is defined as:

$$\mathbf{y} = \Phi\mathbf{z}, \tag{2.1}$$

where $\Phi \in \mathbb{R}^{m \times n}$ is the sensing matrix with all the rows being orthonormal with each other. This is a quite general setup. If the sensing matrix $\Phi$ is an identity matrix, then $\mathbf{y}$ is a vector of sampled values of $\mathbf{z}$. This simple setting is the typical acquisition method for most imaging system, like a digital camera. In the MRI reconstruction problem, $\Phi$ is defined by the Fourier transform. If all the Fourier coefficiences, which are called k-space signals are acquired, then the inverse Fourier transform can be used to reconstruct the MR image. However, the acqusition of the k-space signal is a sequential process. This means that more k-space signal acqusition requires longer time. Therefore, a simple idea to reduce the MRI acquisition time is reducing the number of samples in the k-space. The reconstruction problem based on partial k-space signal is an under-constrained problem with infinite many different solutions. The image cannot be correctly reconstructed based on Shannon sampling theorem. The compressed sensing technique solve this under constrained problem based on additional constraint, the sparseness of the signal.

The sparseness of vector $\mathbf{z}$ is defined based on some orthonormal bases. Given an orthonormal base $\Psi$, the signal $\mathbf{z}$ is expanded into the space defined by $\Psi$ as:

$$\mathbf{z} = \Psi \mathbf{x} \tag{2.2}$$

The signal $\mathbf{z}$ is sparse if it has a sparse expansion $\mathbf{x}$, where $\mathbf{x}$ can discard the small coefficients without much perceptual loss. Formally speaking, consider $\mathbf{z}_k$ obtained by keeping only the terms corresponding to the $k$ largest terms of the $\mathbf{x}$ in the expansion. By definition, $\mathbf{z}_k = \Psi \mathbf{x}_k$, where $\mathbf{x}_k$ is the vector with all but the largest $k$ set to zero. This vector $\mathbf{x}_k$ is strictly sparse. We will call $k$-sparse for such objects with at most $k$ nonzero terms. Since $\Psi$ is an orthonormal transform, we have $\|\mathbf{z} - \mathbf{z}_k\|_2 = \|\mathbf{x} - \mathbf{x}_k\|_2$, and the signal $\mathbf{z}$ is sparse or compressible means the sorted magnitudes of $\mathbf{x}$ decay quickly, then $\mathbf{z}$ is well approximated by $\mathbf{z}_k$ based on $l_2$ norm. This idea is close related to the image compression methods, like JPEG-2000. They often compress the images by discarding small coefficients under some transformation that can sparsify the image data.

Since $\Psi$ is an orthonormal transformation, we have:

$$\mathbf{y} = \Phi \Psi \mathbf{x} \tag{2.3}$$

We can always consider this problem as an optimization problem of $\mathbf{x}$. We further substitute $\Phi\Psi$ with one matrix $A$ and the relation between observation and result becomes:

$$\mathbf{y} = A\mathbf{x}. \tag{2.4}$$

The theory of compressed sensing is built based on a good property of $A$, which is call incoherent. The coherence of the matrix $A$ is defined as:

$$\mu(A) = \sqrt{n} \max(|A|) \tag{2.5}$$

where $\max(|A|)$ is the maximum value of the absolute value of all the elements in matrix $A$. The coherence measures the largest correlation between the vector

before the transformation $\mathbf{x}$ and after the transformation $\mathbf{y}$. The small correlation means that any terms in $\mathbf{y}$ is related to all terms in $\mathbf{x}$ with even weights. The incoherent transform actually requires that $\mathbf{y}$ is a good measurement to all the terms in vector $\mathbf{x}$ instead of partial measurement. In the extreme condition, if $A$ is the identity matrix, then it is a strong coherent matrix. The only way to correctly reconstruct $\mathbf{x}$ is having all the $n$ measurements. Several types of transformation have the incoherent property. Especially, the partial Fourier transform used in compressed sensing is incoherent.

In order to solve the compressed sensing problem, we can minimize the number of non-zero terms in $\mathbf{x}$ while make sure the reconstructed signal $\mathbf{x}$ matches the observation $\mathbf{y}$. This is the following optimization function:

$$\begin{aligned} &\underset{\mathbf{x}}{\operatorname{argmin}} \|\mathbf{x}\|_0 \\ &s.t. A\mathbf{x} = \mathbf{y} \end{aligned} \tag{2.6}$$

where $\|\cdot\|_0$ is the $l_0$-norm, which is the number of non-zero terms. The target of this function is find a sparse vector that matches the target function best. However, this straightforward formulation is hard to solve. It is proved to be NP-hard, which means that it cannot be solved in polynomial time now. All the known solutions will have the same time complexity as enumerating all the possible combinations of non-zero terms at most. The computing time is exponentially with the number of terms in $\mathbf{x}$. Therefore, it is not an efficient method in practice.

One practical method to solve $l_0$-norm regularized optimization problem is relax $l_0$-norm to $l_1$-norm, which is defined as $\|\mathbf{x}\|_1 = \sum_i |x_i|$. Therefore, the optimization problem is relaxed as:

$$\begin{aligned} &\underset{\mathbf{x}}{\operatorname{argmin}} \|\mathbf{x}\|_1 \\ &s.t. A\mathbf{x} = \mathbf{y} \end{aligned} \tag{2.7}$$

The $l_1$ relaxation is easier to be solved than the original $l_0$ norm regularized problem, since it is convex. Therefore, this relaxed problem is solvable by various convex optimization algorithms that are all solved in polynomial time. However, can the solution of the relaxed problem match well with the original result? The following theory of compressed sensing [12] shows that the result will be the same as that of the original problem with high probability.

**Theorem 1.** *Suppose that the coefficient sequence* $\mathbf{x}$ *is k-sparse. Select m measurements based on sensing matrix A with all the rows orthonormal with each other. Then if*

$$m \geq C \cdot \mu(A) \cdot k \cdot \log n \tag{2.8}$$

*for some positive constant C. The solution to Equation 2.7 is exact with overwhelming probability.*

Generally, the number of measurements required for the reconstruction is related to the sparseness of the signal and the incoherent property of the sensing matrix $A$.

One extension of Theorem 1 is applied the compressed sensing to piece-wise constant signal. Supposing the signal only changes at sparse location, the finite difference of the signal is sparse. It can be consider as the sparseness of the gradient. The signal can be recovered with the following optimization function based on [11] Corollary 1.4:

$$\begin{aligned} &\underset{\mathbf{x}}{\operatorname{argmin}} \sum_{i \in (1,\ldots,n-1)} |\mathbf{x}_{i+1} - \mathbf{x}_i| \\ &s.t. A\mathbf{x} = \mathbf{y} \end{aligned} \tag{2.9}$$

The finite difference in the high dimensional space is the total variation, which is widely used for MR image reconstruction [59].

Equation 2.7 requires that the signal $\mathbf{x}$ exactly matches the observation $\mathbf{y}$. However, this is a too-strong assumption in most practical problems. The observation $\mathbf{y}$ may also contain noises. The true signal may be just approximately sparse with all but the largest $k$ terms very small. In order to deal with these kinds of near optimum conditions, we need to introduce the concept of restricted isometry property (RIP) [12]. For each integer $k = 1, 2, \ldots$, define the isometry constant $\delta_k$ of a matrix $A$ as the smallest number such that

$$(1 - \delta_k)\|\mathbf{x}\|_2^2 \leq \|A\mathbf{x}\|_2^2 \leq (1 + \delta_k)\|\mathbf{x}\|_2^2 \tag{2.10}$$

holds for all $k$-sparse vectors $\mathbf{x}$. This property means that $A$ approximately preserves the Euclidean length of any $k$-sparse signals. This implies that any $k$-sparse vectors cannot be in the null space of $A$, as the vectors in the null space are not possible to be recovered.

The noisy data then can be reconstructed based on the following $l_1$ minimization with relaxed constraints:

$$\begin{aligned} &\underset{\mathbf{x}}{\operatorname{argmin}} \|\mathbf{x}\|_1 \\ &s.t. \|A\mathbf{x} - \mathbf{y}\| \leq \epsilon \end{aligned} \tag{2.11}$$

where $\epsilon$ bounds the amount of noise in the data.

**Theorem 2.** *Assume that $\delta_{2k} < \sqrt{2} - 1$. Then the solution $\mathbf{x}^*$ to Equation 2.11 obeys*

$$\|\mathbf{x}^* - \mathbf{x}\|_2 \leq C_0 \cdot \frac{\|\mathbf{x} - \mathbf{x}_k\|_1}{\sqrt{k}} + C_1 \cdot \epsilon \tag{2.12}$$

*for some constants $C_0$ and $C_1$.*

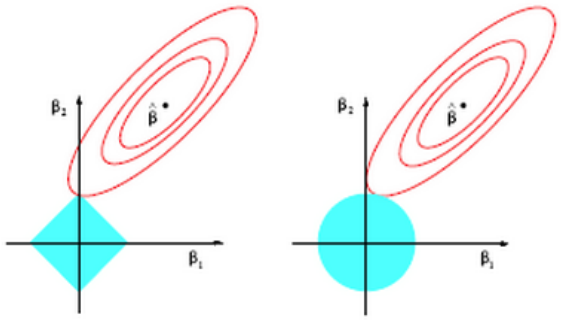


Figure 2.1: Estimation picture of $l_2$-norm (left) and $l_1$-norm (right) regularized regression.

This theorem is published in [14]. It shows that the reconstructed solution $\mathbf{x}^*$ is close to the original signal $\mathbf{x}$, when the original signal $\mathbf{x}$ is close to its $k$-sparse approximation $\mathbf{x}_k$ and the noise in the observation is small. This constrained optimization problem is usually transformed into an unconstrained form of a weighted summation of the data term and the regularization term:

$$\underset{\mathbf{x}}{\operatorname{argmin}} \|\mathbf{y} - A\mathbf{x}\|_2^2 + \lambda \|\Psi\mathbf{x}\|_1 \tag{2.13}$$

where $\lambda$ is the sparse coefficient. Theoretically, for any given $\epsilon$, there is a value of $\lambda$ that the solutions of the two problems in equation 2.11 and equation 2.13 are the same. The only different is how to set these two coefficients in practice. In the following thesis, we are mostly dealing with the problem with the form similar to equation 2.13.

One active argument is that what is the different between the problem in equation 2.13 and the following ridge regression problem:

$$\underset{\mathbf{x}}{\operatorname{argmin}} \|\mathbf{y} - A\mathbf{x}\|_2^2 + \lambda \|\Psi\mathbf{x}\|_2 \tag{2.14}$$

where $l_2$-norm is used instead of $l_1$-norm. The ridge regression has already been

widely used to reduce the influence of outliers and overcome the overfitting. However, instead of encourage sparseness, the reconstructed result with $l_2$-norm regularization is more likely to have all terms as non-zero. This is because of their different shapes. The $l_2$-norm is an isotropic norm, while the $l_1$-norm is anisotropy. The anisotropic structure of the $l_1$-norm makes the solution more likely to contain zero terms. Figure 2.1 provides some insight for the difference between $l_2$- and $l_1$-norm regularization in 2-dimensional problem. We define the object function as:

$$(\boldsymbol{\beta} - \hat{\boldsymbol{\beta}})^T X^T X(\boldsymbol{\beta} - \hat{\boldsymbol{\beta}}) \tag{2.15}$$

where the minimum of the object function is archived at point $\hat{\boldsymbol{\beta}}$, and the red curves are the elliptical contours of this function. The $l_2$- and $l_1$-norm constraints are used to regularize $\boldsymbol{\beta}$ in the blue regions, respectively. The $l_2$-norm constraint defines a circle region, where the probability of having zero terms in the solution is zero. However, the $l_1$-norm constraint defines a rotated square region, where the contours of the object function touch at a corner, corresponding to a zero coefficient. Generally, the $l_1$-norm has corners or edges at positions with zeros terms, where are more likely to be touched by the contours of the object function. Therefore, the $l_1$-norm constraint will encourage sparseness. The difference highlights the importance of intrinsic sparse property for the data. When the data is not sparse, the $l_1$-norm may not be better, or may even be worse than $l_2$-norm regularization. However, the sparsity-based methods become powerful when the data really has the sparse property.

In fact, the success of the theory about compressed sensing motivates many research related to utilizing $l_1$-norm constraints for different types of machine learning and computer vision problems to exploit their sparse properties. However, most of these work cannot be supported by the current compressed sensing theory. Generally the compressed sensing theory focuses on reducing the acquisition cost for the compressible signals. Traditionally, the full signal is fist acquired and

then compressed for storage, like digital image. This is extremely wasteful. Differently, the compressed sensing method reduces the number of sampling by directly acquire just the important information. This will benefit the practical problem that the acquisition has heavy cost, like MRI acquisition. Most sparse-based machine learning problems deal with tasks other than signal reconstruction. They solve more general optimization problem with sparse constraints, where the incoherent property of the sensing matrix is not well studied or the target function is completely different from what we presented here. This is more related to the general statistical learning under $l_1$-norm constraint, like lasso (least absolute shrinkage and selection operator) [103]. The theories for these general problem are more interesting and require further studies.

## 2.2 Parallel MRI Reconstruction

Multi-coil parallel magnetic resonance imaging (MRI) is a powerful technique introduced [96] to accelerate the image acquisition. The image signals from a patient are simultaneously collected by a group of spatially distributed coils with different sensitivity profiles. Each coil, instead of sampling the full k-space, only samples it partially. Since less sampling is required for each coil, the time of the MRI scanning is reduced by parallel imaging without compromising the quality. The MRI image is then reconstructed by combining the information from all the coils based on their sensitivity profiles. In parallel MRI, it is an ill-posed problem to reconstruct both the MRI image and the coil sensitivity maps jointly. Therefore, parallel MRI reconstruction methods, e.g., SMASH [96] and SENSE [86], require estimation of the coil sensitivity profiles before image reconstruction. These methods often proceed in two stages: 1) the calibration stage, in which the sensitivity profiles are explicitly estimated; 2) the reconstruction stage, in which the image is reconstructed based

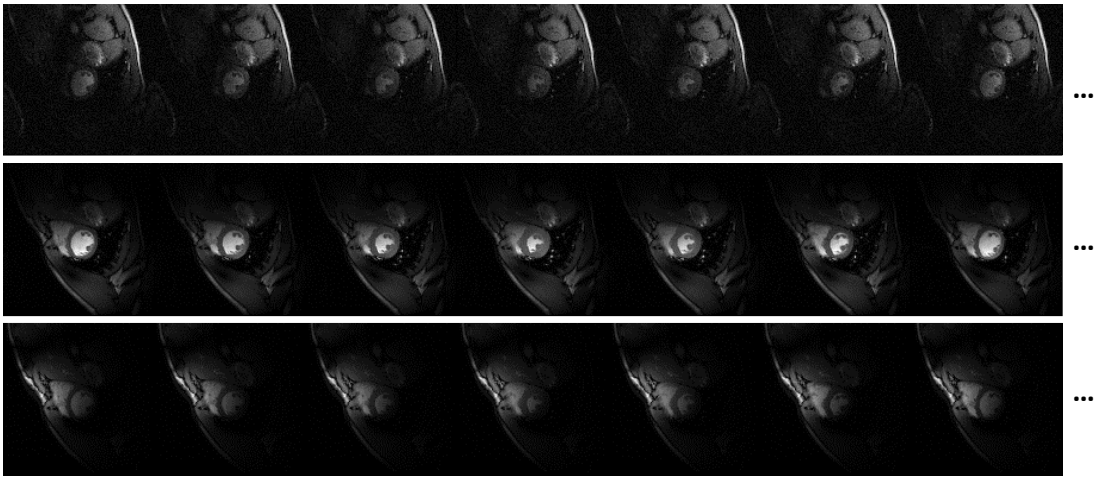

Figure 2.2: Sensitivity encoded images from different coils (rows) and frames (columns).

on the estimated sensitivity maps. A major limitation is that the reconstruction accuracy is sensitive to the calibration accuracy.

In dynamic multi-coil parallel MRI, the cost of the calibration is amplified, since the sensitivity profiles of all coils change due to the patient's movements. Previous work [7, 77, 78] used SENSE [86] to reconstruct the parallel dynamic MRI images, where the explicit coil sensitivity estimations are required at each time frame. This does not only increase the acquisition time, but may also introduce calibration errors due to the patient's movements. For example, in cardiac MRI, patients are required to hold their breath in each scan. The time of the breath holding is limited, so the calibration and reconstruction scans may be acquired in different respiratory periods. However, it is unrealistic to expect the patients to hold their breath while the internal organs of the upper body are at the same position each time. The varying displacement of the chest will cause a misalignment between the scans during the calibration and reconstruction stages. Such movement-caused inconsistencies in the coil sensitivity estimation may result in significant visual artifacts in reconstructed images [8].

To avoid the calibration step for parallel MRI, some calibrationless methods [18,

61, 95] have been proposed recently. Instead of reconstructing the original image directly, they reconstruct the sensitivity encoded images for all the coils. The different coils focus on the same anatomical cross-section during the scan. They produce different images only due to their different sensitivity profiles. Figure 2.2 shows some sample sensitivity encoded images from different coils. Different regions are highlighted due to the coil sensitivity profiles, while the intrinsic image information remains the same. Therefore, all the sensitivity encoded images should have high valued responses to sparsifying transforms at the same positions. Majumdar et al. [61] reconstructed the parallel MRI images based on the fact that the position of the high valued wavelet transform coefficients in different sensitivity encoded coil images remain the same. They applied a group sparse constraint to the wavelet transform coefficients for all the images, and solved the optimization problem with Majorization-Minimization. Chen et al. [18] utilized the spatial total variation as the image constraint, and the images from different coils are reconstructed based on joint total variation. Shin et al. [95] explored the low rank property of the image blocks in the k-space data, and optimized a structured low-rank matrix completion problem to generate coil-by-coil sensitivity encoded images.

In the following section, we will propose a new parallel MRI method for dynamic images, called calibrationless dynamic MRI with joint temporal sparsity. Our method is an extension of the temporal sparse SENSE method [78], which explores the benefit of temporal sparse properties of the MRI sequence. Unlike previous calibrationless methods, we do not assume any spatial sparse constraints.The temporal signal contains more redundancy, due to the smoothness of the displacement field. In addition, the signals among different coils are different, due to their sensitivity profiles. Due to the smoothness of the coil sensitivity maps, the temporal changing patterns of intensities in the various coil images are similar. Therefore, we utilize the smoothness of the temporal changes and the correlation of the coil

images to propose a joint temporal sparse model to reconstruct parallel dynamic images simultaneously. We present two variants using different temporal sparsifying operators. They are compared to the state-of-the-art parallel dynamic MRI reconstruction algorithms, and both show improved performance.

## 2.3 Joint Temporal Sparse MRI Reconstruction

In this section, we first introduce the dynamic MRI reconstruction based on compressed sensing and SENSE [78]. Then we present our calibrationless method, which reconstructs the image without the coil sensitivity profiles. Finally, the optimization algorithms are discussed for two typical temporal sparse constraints in our framework.

### 2.3.1 k-t SPARSE-SENSE

The MRI reconstruction techniques have attracted increasing attention in recent years, due to improved results based on compressed sensing [47, 59]. The key idea for compressed sensing in MRI, is to explore the resulting image compressibility due to the image sparseness under certain transforms, e.g., wavelet. By enforcing these sparse priors, less sampling is required to acquire and reconstruct the MRI image, which is almost lossless. Compressed sensing is suitable for dynamic MRI since there is redundant information in the sequential temporal data. This is very similar to video compression, where the inter-frame encoding is much more efficient than the intra-frame encoding. For example, in k-t SPARSE-SENSE [78], a temporal Fourier transform is used to sparsify the MRI image sequence.

Let $\bar{X} \in \mathbb{R}^{M \times N \times T}$ denote a dynamic MRI image sequence, where the image size is $M \times N$, and the number of frames is $T$. Assuming there are $C$ parallel coils used in the imaging process, under-sampled k-space data $y_{ct}$ are acquired from coil

$c \in \{1, ..., C\}$ at time $t \in \{1, ..., T\}$. The problem of reconstructing $\bar{X}$ is formulated as:

$$\underset{\bar{X}}{\operatorname{argmin}}\{\frac{1}{2}\sum_{c=1}^{C}\sum_{t=1}^{T}\|F_{ct}S_{ct}\bar{X}_t - y_{ct}\|_2^2 + \lambda\sum_{i=1}^{M}\sum_{j=1}^{N}\|\Phi\bar{X}_{ij}\|_1\} \tag{2.16}$$

where $F_{ct}$ is the partial Fourier transform, $\Phi$ is a temporal sparsifying operator on each pixel (e.g., temporal Fourier transform), and $\lambda$ is the sparsity parameter. Before solving Eq. (1), the coil sensitivity profiles $S_{ct}$ are estimated in the calibration stage.

### 2.3.2 Our Approach: Joint Temporal Sparsity

In this section, we present a calibrationless method to reconstruct the image without coil sensitivity estimation. Since the signals on all the coils are acquired from the same anatomical cross section, they are closely correlated with each other. The signals have similar sparse properties for all the coils, i.e., the corresponding transform terms are likely to be zeros or not at the same time. Therefore, we propose joint temporal sparse priors for dynamic MRI reconstruction, to implicitly enforce the relations among different coils. The coil sensitivity profiles are not required for our method, which eliminates a significant source of error in the reconstructed MRI images.

The coil-dependent sensitivity-encoded dynamic images $X \in \mathbb{R}^{M\times N\times T\times C}$ are reconstructed in our proposed calibrationless algorithm, instead of the final image $\bar{X}$. The reason is that each sensitivity-encoded image $X_{ct} = S_{ct}\bar{X}_t$ contains its coil sensitivity profile in itself, and therefore the $S_{ct}$ is not required to be estimated explicitly to solve the reconstruction. In our approach, the problem of reconstructing the sensitivity-encoded images $X$ based on the MRI signals $y_{ct}$ is formulated as:

$$\underset{X}{\operatorname{argmin}}\{\frac{1}{2}\sum_{c=1}^{C}\sum_{t=1}^{T}\|F_{ct}X_{ct} - y_{ct}\|_2^2 + \lambda\sum_{i=1}^{M}\sum_{j=1}^{N}\|\Phi X_{ij}\|_{2,1}\} \tag{2.17}$$

where $\|\cdot\|_{2,1}$ is the $L2,1$ norm, which regularizes the pixel-by-pixel temporal sparseness jointly among coils. Let $Z_{ij} = \Phi X_{ij}$ be the transformed image data at one pixel location for all $C$ coils and $T$ frames. The size of matrix $Z_{ij}$ is $C \times B$, where $B$ is the dimensionality of the transform $\Phi$, e.g., the number of coefficients in the temporal Fourier transform. The $L2,1$ norm can be rewritten as:

$$\|Z_{ij}\|_{2,1} = \sum_{b=1}^{B} \|Z_{ijb}\|_2 = \sum_{b=1}^{B} \left( \sum_{c=1}^{C} |Z_{ijcb}|^2 \right)^{\frac{1}{2}} \tag{2.18}$$

where the column-wise $L2$ norm is first applied to the coil dimension of $Z_{ij}$, and then the row-wise $L1$ norm is applied to the transform's dimension. In this way, the corresponding terms in different coils are likely to be zero or not at the same time. Various types of sparsifying operators can be used for temporal MRI image reconstruction since, as we mentioned, the pixel variation over time is smooth. Typical choices include the temporal Fourier transform and temporal finite differences.

Although the coil sensitivity profiles are removed from the formulation, the coil images are still correlated with each other, based on joint sparse constraints. Finally, since these are sensitivity-encoded images they can be combined via a sum of squares approach [40, 60] to produce the final image.

### 2.3.3 Optimization Algorithm

There are generally two types of joint sparse priors that can be used, based on whether the inverse transform is available. The problem is relatively easy when there is an invertible transform like the temporal Fourier transform, since $X_{ij} = \Phi_F^T Z_{ij}$ can be represented as a function of $Z$. Therefore, we rewrite equation 2.17 using the Fourier transform to solve for $Z$:

$$\underset{Z}{\operatorname{argmin}} \{ \frac{1}{2} \sum_{c=1}^{C} \|F_c \Phi_F^T Z_c - y_c\|_2^2 + \lambda \sum_{i=1}^{M} \sum_{j=1}^{N} \|Z_{ij}\|_{2,1} \} \tag{2.19}$$

This formulation can be directly solved with FISTA [5] which requires solving

the following subproblem for all pixels in each iteration:

$$\underset{Z_{ij}}{\operatorname{argmin}}\{\frac{1}{2}\|Z_{ij}-\tilde{Z}_{ij}\|_2^2+\lambda\|Z_{ij}\|_{2,1}\} \tag{2.20}$$

where $\tilde{Z}_{ij}$ is known at the beginning of the iteration. This subproblem has the following analytical solution:

$$Z_{ijt}=\begin{cases}\frac{\|Z_{ijt}\|_2-\lambda}{\|Z_{ijt}\|_2}Z_{ijt} & \text{if } \|Z_{ijt}\|_2>\lambda \\ 0 & \text{otherwise}\end{cases} \tag{2.21}$$

The problem is more complex when no invertible transform exists, like the finite differences. We still use FISTA to solve the problem, while the subproblem is more complex:

$$\underset{X_{ij}}{\operatorname{argmin}}\{\frac{1}{2}\|X_{ij}-\tilde{X}_{ij}\|_2^2+\lambda\|\Phi_D X_{ij}\|_{2,1}\} \tag{2.22}$$

where $\tilde{X}$ is known for each iteration. Following previous work [4, 56], we consider the dual problem for equation 2.22. Let $P\in\mathbb{R}^{C\times(T-1)}$, which satisfies:

$$\sum_{c=1}^{C}P_{ct}^2\leq 1\quad\forall t,\quad |P_{ct}|\leq 1\quad\forall c,t \tag{2.23}$$

The relation between $X$ and $P$ is defined by a linear operator $\mathcal{L}(P)_{ct}=P_{ct}-P_{c(t-1)}$ and the corresponding inverse operator $\mathcal{L}^T(X)=P$, where $P_{ct}=X_{ct}-X_{ct+1}$. The optimal solution for equation 2.22 is $X=\tilde{X}-\lambda\mathcal{L}(P^*)$, based on [4], where $P^*$ is the optimal solution for the dual problem $\min_P\frac{1}{2}\|\tilde{X}-\lambda\mathcal{L}(P)\|_2^2$. This dual problem can also be solved by FISTA iteratively.

## 2.4 Experiments

The experiments were conducted on cardiac parallel dynamic MRI dataset. The cardiac cine MRI recorded the heart motion during a cardiac cycle for assessment of its function. A Steady State Free Precession (SSFP) pulse sequence with cartesian

Figure 2.3: The visual results of different methods. The first row is five frames from the ground truth. The following two rows are generated using zero filled FFT and k-t SPARSE-SENSE [78]. The final two rows are the results of our calibrationless method with temporal Fourier transform, and finite differences.

sampling was employed for data acquisition on a 1.5T Siemens scanner equipped with the standard 32-element matrix coil array.

We first compare our proposed joint temporal sparse method with k-t SPARSE-SENSE [78], which is a calibration based method. Uniform random sampling masks were used with reduction factor four to under-sample the original k-space

data. Figure 2.3 shows the reconstruction results on five time frames of a cardiac cine MRI sequence. Two types of temporal constraints, Fourier transform and finite differences, are validated in our framework. Both variants of our methods show similar visual results as k-t SPARSE-SENSE. This shows the benefit of the joint sparseness prior for temporal signals. Notice that the coil sensitivity maps, which were provided for k-t SPARSE-SENSE during the reconstruction, are unknown to our methods.

We then compared our proposed method to other calibrationless algorithms quantitatively, including k-t SPARSE-SENSE (publicly available code exists), CaLM MRI [61], and Joint Total Variation [18] (based on our own implementations). Since CaLM MRI and Joint Total Variation were designed for static MR image reconstruction, we simply applied their methods to our dynamic MR images frame by frame. To reduce randomness, we ran each algorithm 10 times to obtain the average results. Table 2.1 shows the average SNRs and computing times for all the methods. The two variants of our proposed method showed consistently better performance than all the other calibrationless algorithms, due to our novel approach, which is based on the temporal sparse priors. CaLM MRI [61] and joint total variation [18] are slower than our temporal sparse constraint approach, since the 2D spatial constraints have higher computing cost. Although k-t SPARSE-SENSE utilized additional coil sensitivity information, it is still slower than our proposed algorithms due to the inefficient optimization algorithm. Our method does not require coil calibration. It leads to further reductions in the time and the motion errors in dynamic MRI acquisitions.

Table 2.1: Comparison of Signal-to-Noise Ratio (SNR) and computing times of different calibrationless MRI reconstruction methods

| Method | SNR (dB) | Time (s) |
|---|---|---|
| k-t SPARSE-SENSE [78] | 22.1 | 362.2 |
| CaLM MRI [61] | 17.8 | 624.5 |
| Joint Total Variation [18] | 19.8 | 497.0 |
| Proposed with Fourier transform | 24.5 | **160.7** |
| Proposed with finite differences | **26.6** | 281.9 |

## 2.5 Conclusions

We have proposed a novel calibrationless algorithm to accelerate the dynamic MRI reconstructions with parallel imaging and compressed sensing. The main novelty is in the use of a joint temporal sparsity approach, which does not require one to estimate the coil calibration. The temporal sparse priors are utilized in a joint way to exploit both signal sparseness and coil correlation. Two typical temporal sparse priors, the Fourier transform and the finite differences, were validated with our proposed joint sparse optimization algorithms. The experiments show that the proposed method outperforms the state-of-art parallel dynamic MRI reconstruction algorithms. In addition, the proposed method is better than other calibrationless algorithms in terms of both accuracy and efficiency and has the potential to improve the efficiency of clinical MRI.

# Chapter 3

# Left Ventricle Motion Analysis using Meshless Deformable Models

Tagged magnetic resonance imaging (MRI) provides a powerful non-invasive technique for revealing the motion of the myocardial wall under normal and diseased conditions of the heart. Importantly, this technique has been implemented on mice, which have been used extensively for studying human heart diseases. Three-dimensional motion and strain analysis of the tagged MR images would provide an import tool for depicting wall motion and contractile function of the heart in 3D fashion. In this section, we propose a framework to reconstruct the left ventricular motion of the mouse heart using tagged MR images. In our framework, the 2D tagging lines are extracted using a Gabor filter bank, and then the contours are automatically delineated using deformable models. Then, the 3D control points are generated from the movement of the tagging lines, and a 3D meshless model is built using modified coherent point drift (CPD) based on the sparse contours. Finally, the meshless model of the left ventricle is driven to deform by the control points with our proposed *nonlinear Laplacian kernel* function. The strain of the myocardial wall is analyzed based on the meshless deformation results. This method is validated using the in vivo MRI tagging data from the mouse heart. The results show that the proposed method effectively quantifies the myocardium strain distribution, which has the potential to detect accurately various kinds of heart diseases.

## 3.1 Introduction

Over the past two decades, experiments utilizing transgenic and knockout mice have significantly advanced the research on cardiovascular diseases, and these models have become an indispensable tool to study the cardiovascular diseases in humans [133]. The majority of such studies have employed ex vivo methods (e.g. immunostaining) for assessing the results of gene manipulation, and, for the heart function, catheter-based measurements of left-ventricular (LV) pressure in isolated Langendorff-perfused hearts are obtained. For the study of ventricular function in particular, noninvasive imaging offers a powerful non-invasively tool for making measurements that directly reflect its complex in vivo physiology.

Tagged magnetic resonance imaging (tMRI) has been widely used to analyze the cardiac wall motion [15]. It has been widely used for the determination of human heart diseases as well as in experimental heart disease models in mice. It visualizes the in-wall deformation of the myocardium in a noninvasive manner. Conventional MRI can only distinguish different tissues. The myocardial wall shows similar intensity. Therefore, there are only a few landmarks on the boundary of the ventricles that can be reliably identified. The MR tagging methods [2, 127] are introduced to increase the number of landmarks to be detected and tracked over a cardiac cycle. By applying spatial variance magnetic field in tissue, one can create line patterns on the MR images. As the tissue moves, the tags will move in the subsequent images. They directly reflect the motion of the tissue within otherwise featureless structures such as the myocardial wall. This helps the expert to analyze the myocardial wall motion and diagnose heart diseases.

A typical cardiac motion analysis system often consist of three parts: heart segmentation, motion tracking and motion analysis. In the first step, both epicardial and endocardial boundaries are delineated to distinguish myocardium and other

tissues. After building the inital heart model, its motion is tracked in a cardiac cycle based on the landmark movements. In the final step, the motion properties, like motion strain, are calculated based on deformable models. These motion properties show the local dynamic information of the heart. This is a direct evaluation of the heart conditions. Although there are already several work in this area [109], cardiac motion analysis is still a hard problem due to the challenging data.

The data acquisition from the mouse heart is usually analyzed based on similar framework. However, it is more challenging for achieving adequate spatial and temporal resolutions compared with the human heart. The mouse heart is about 1000th the size of a human heart and beats much faster at 400-600 beats per minute (bpm) than human heart with 60-80 bpm. Currently available MRI instruments for mouse imaging operate at a higher magnetic field strength (4.7T or above) than clinical MRI scanners but is still unable to provide temporal and spatial resolution in proportion with the mouse heart rate and size. Consequently, a compromise is obtained between tagging spatial and temporal resolution in order to complete the study in reasonable amount of time. As shown in Fig. 3.1a, there are five SA slices which can only cover the equatorial region of the LV. The deformation in the apex and base regions should be estimated by combining the contour and tagging line information. Meanwhile, the distances between the tagging lines are small in Fig. 3.1b. The tagging lines are easily tracked into adjacent ones in the dim images.

In 2D tagged MR images, the tagging lines show the motion of the myocardial wall along the line. Although the tags provide motion information inside the myocardial wall, they destroy the continuity of the myocardial wall boundary. The fragmented edges will cause leaking during the segmentation, so it is very hard to segment tagged MR image directly. During the motion tracking, the more lines on the heart, the more motion details are shown. This requires higher spatial resolution for the MR images, since the density of the tags cannot be larger than

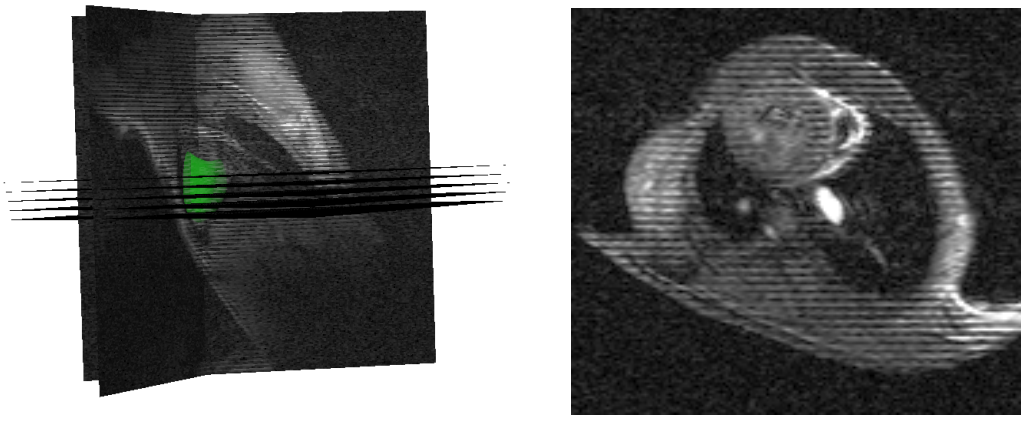

(a) (b)

Figure 3.1: (a) The setting of the MR images with fitted LV model: five SA images parallel placed with equal displacements, and four LA images taken with 45° in between. (b) Tagged SA image. The image resolution is low, and the tagging lines are blurred due to the fast heart beating rate.

the number of pixels in this direction. Meanwhile, the displacement of the tissue should not be larger than the distance between tags in consequence time frame in order to track the tissue motion. Otherwise, there is ambiguity about which one the tag will match. Currently, the tagged MRI methods provide only 2-3 tagging lines on the radial direction of the mouse left ventricle, which is the thickest wall in the whole heart. It is hard to reconstruct the motion, which is not only geometrically reasonable, but also physically correct. In one 2D slice, there are typically two images with tagging lines perpendicular to each other. Based on the tagging line tracking results, the movements of all the intersection points are estimated. In most 2D cardiac motion analysis problem, the intersection point movement will directly be used as control point for deformable models.

The problem becomes more complex when we extend the motion modeling to 3D space. The first problem is that most data is not full 3D volume data. The data often contain only sparse slices with large gaps between them. The MR images from different directions, i.e., short axis and long axis images, are acquired

to improve the resolution on the whole 3D space. Since there is no boundary information in the gaps between slices, the 3D contour is estimated based on the incomplete 2D cues. During the motion tracking, the landmarks are hard to define based on sparse slices. The intersection points defined in 2D slices are not the same material point in a cardiac cycle. The MR image stay at a fixed slice during the acquisition. During the heart movement, the material points will move into and out of the given slice. This means that we cannot capture movement of any particular material point based on only sparse slices. The displacements of control points are often generated based on interpolation. The interpolation step will smooth the model displacement and remove the motion details.

In view of these problem, we propose a complete framework for mouse cardiac motion analysis based on tagged MR images. The extended active contour models are used to extract the contours and tags of the heart in 2D. The 3D cardiac model is built based on coherent point drift (CPD) [71]. The landmark points are estimated based on our method with minimum interpolation. We use physical based meshless deformable models to track the 3D left ventricle motion. The system is applied to mouse data and shows promising result.

## 3.2 Related Work

In recent studies, as the increasing of human MRI data, many methods have been developed to track and measure the cardiac motion [109]. There are two main categories. The first category aims to track the model motion based on feature extraction in spatial domain. The tagging lines and their intersections were usually detected first. Then the myocardial motion was estimated based on their displacements. [118] used the 2D active contour model to track the tagging lines semiautomatically. Then, the LV was represented as a volumetric deformable model, and

driven by the displacement of the tag intersections. [21] employed the Gabor filter banks to detect the local tag intersections, and robust point matching to sparsely track the myocardial motion. The whole model was then deformable based on the intersection point tracking results. When the whole 3D volume sequence of the cardiac motion is available, nonrigid registration method [93] is used to track the heart motion. However, this method cannot be applied to the data with only sparse slices. Optical flow [30] is also used to track the heart motion. The intensity of each pixel will change due to the decay of the magnetic field. This violates the intensity constancy assumption of optical flow. Various methods [30] proposed to estimate the change of the intensity and match the pixels with time-varying intensity. The methods in the second category obtains the deformation field based on the frequency domain information. HARP(Harmonic Phase) [76] analyzed the image in the frequency domain. The tagging technique gave rise to spectral peaks in k-space. The tagging motions were extracted from the inverse Fourier transform of a single peak. Other methods used local sine wave modeling [1] or Gabor filter banks [21] to analyze the image in the frequency domain. These methods cannot handle large tagging movement, and estimate only in-plane motion. Additional information was needed to reconstruct 3D motion with only sparse tagged MR images.

Several methods developed for human data have been applied to murine cardiac motion analysis. The characterization of the murine cardiac mechanical function in normal, infarcted, or genetically engineered mice or rat model subjected to stem cell intervention were reported in [57, 119, 133], and 3D rendering of LV deformation was attempted. For example, recently [131] represented the 3D myocardial deformation based on the movement of material points near the sparse SA slices. By decomposing the heart movement in long-axis (LA) and SA directions, [23] reconstructed the motion of the whole heart based on the combination of the

displacement of intersections in all these components.

Meshless deformable models are first proposed as a substitute to the mesh-based finite element models. Comparing to mesh-based models, meshless models allow larger deformation. No local connection information is recorded in the model. The material points can move far away from their original neighbors. The new neighbors are defined dynamically based on their distances. The meshless models are first used to simulate the fluid as smoothed-particle hydrodynamics (SPH) [38]. Then the methods are extended to deal with object with large deformation [72]. A more extensive introduction for meshless model can be find in [6, 55]. Wong et al. [113] use meshless model to simulate the heart motion based on cardiac physiome model. They introduce the pacemaker cells to generate action potentials at the beginning of a cardiac cycle. The heart deforms due to the stress generated from the electric signal from pacemaker cells. The personalize electromechanical properties of the heart is required for the whole model. In our work, we estimate the heart motion based on solely the MRI data, so no additional electric model is needed.

## 3.3 Cardiac Image Analysis System

We first give a brief overview of our cardiac motion analysis system based on meshless deformable models. Similar to the general framework, we first generate the initial 3D left ventricle model from a group of cine MR images from different directions. We delineate the left ventricle contours in each 2D image, and then project them to 3D space based on the position of each slice in physical space. A standard left ventricle model is deformed with coherent point drift method to fit these 2D contour lines. In this way, we produce a 3D left ventricle model that does

not only match the 2D contour lines, but is also similar to the standard left ventricle model. Then, we deform it with our meshless deformable models. The initial model is represented as a meshless volume. It deforms based on the motion sequences of landmarks calculated based on the tagging line movements in a cardiac cycle. Finally, we calculate the strain on each material point based on moving least square.

### 3.3.1 Initial Model Reconstruction

Left ventricle is first segmented in each 2D image [107]. On the short axis images, left ventricle is normal a ring shape. The blood pool is inside the endocardial boundary and left ventricle muscle is between the epicardial and endocardial boundaries. We first segment the blood pool with graph cut. This will produce the endocardial boundary. Then the ring area close to the blood pool is considered as left ventricle area, while the area far away is background. We apply graph cut again to delineate the epicardial boundary. Graph cut will often produce non-smooth left ventricle boundary due to its connection to the right ventricle and papillary muscles. We use active contour models to refine the boundaries. On the long axis images, left ventricle shows a U-shape with its open to the left atrium or aorta. There are valves between them, while they are often unclear due to their thin structure and fast moving. Similar to short axis image, we use graph cut to segment the left ventricle and active contour models to refine the boundary. The segmentation results are combined together to reconstruct the 3D left ventricle model, and they will also be used for the tagging line tracking on 2D images.

The DICOM information of each MR image contains the position of this image slice in physical space. We use this to project the boundaries back to the 3D space. These 2D boundaries should lie on the surface of the 3D left ventricle model. This

means that the short axis and long axis boundaries should always have intersection points. However, they often do not intersect with each other due to the segmentation errors. We reconstruct the 3D surface model by utilizing a generic left ventricle model. The generic left ventricle model is built from MR images obtained from a healthy volunteer. The heart is manually segmented and validated by experts. This provide a sample for the standard left ventricle shape. We use CPD [71] to deform the generic model to fit all the 2D boundaries generated above. The deformed model will be still similar to a generic model. Meanwhile, it matches the boundaries in each 2D spaces. On the point where different slices provide inconsistent cues, the result will balance their effect. The 3D model is only needed in the initial time frame. This initial model will deform to the following frames based on the landmark motions.

### 3.3.2 Landmark motion tracking

The landmark points are extracted based on the movements of tagging lines in each MR images. We will first track the tagging lines in each image separately. Then we interpolate them to generate the 3D motion on landmark points.

#### Tagging Line Tracking

The tagging lines are generated by a special pulse sequence of initial magnetic field. At the beginning, they are parallel line pattern along one direction inside the image plane. The tags will move with the cardiac tissues and show the muscle movement. We track the tagging lines in each image separately. Each tagging line is defined by a spline. It tracks the location with lowest intensity to follow the tagging line position. Similar to active contour models, the smoothness of the spline is constrained by its first and second derivatives. Meanwhile, we add a repulsive force between tagging lines, since two tags will not intersect with each

other.

**Control Point Generation**

After tracking the 2D tagging lines from tagged MR images, we extract 3D control points from them to drive deformable models. The material points starting at the intersections of the initial SA images are used as the control points in [131]. They propose an iterative interpolation method to linearly approximate the material point displacements from the initial intersections. However, this intuitive method makes the problem harder. The material points on the intersections will move out of the initial slice in the consequence slices. Considering all the material points that projected to the same intersection on the SA at initial frame, they may have very different displacements on SA direction due to contracting and twisting motion of the heart. Therefore, the new position of an intersection point cannot be estimated based on the corresponding intersection point alone. Interpolations are needed in all three directions. In contrast to [131], we map the intersections at each frame back to the initial frame to utilize the special property of tagging planes. The tagging planes are created at initial frame as a flat plane, then bent during the LV deformation. The points on the intersections of tagging lines are always on the intersections of corresponding tagging planes. Due to the flat property of the tagging planes at initial frame, the SA projections of these points are always the intersections at initial frame. Therefore, only the LA position interpolation is needed when it is mapped back to the initial frame. This will improve the accuracy while accelerating the process.

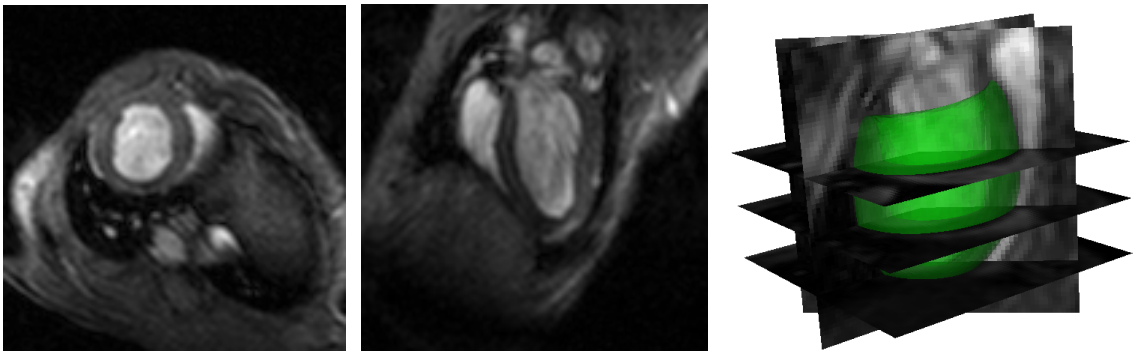

(a) Short axis image (b) Long axis image (c) 3D embedded view

Figure 3.2: The mouse left ventricle has a ring shape on the short-axis images (a) and a U shape on the long-axis images (b). By mapping them to the 3D anatomic space, they intersect with the reconstructed left ventricle model exactly on the left ventricle boundaries (c).

## 3.4 Initial Model Reconstruction

Most of the previous work focuses on left ventricle reconstruction based on short-axis [84, 87, 99]. Since the short-axis images are parallel to each other, they are usually combined to a 3D volume. However, due to the limited number of slices, the inter-slice resolution is usually much lower than intra-slice directions. The distance between slices is about 10 times the pixel distance inside each slice. During the MR image acquisition, the long-axis images usually are first generated to localize the heart position, while they are rarely used for the segmentation for the left ventricle [24, 106]. These images have higher resolution in the long axis, which can help overcome the low inter-slice resolution on short-axis images. Therefore, we utilize both short- and long-axis MR images simultaneously in this work for 3D left ventricle reconstruction. Each image at different position provides different contours of the model. Meanwhile, the consistency among them improves the robustness of the reconstruction.

The short- and long-axis images are instances of the same volume of different orientations. Fradkin et al. [37] utilized their consistency to infer the short-axis image position based on the long-axis segmentation result. However, the spatial

relationship is only used for initialization. The short-axis contours are then deformed independently. The contours after deformation may be inconsistent with the long-axis ones. Koikkalainen et al. [53] reconstructed a 3D heart model based on parallel MR images from the short and long axes. Different from usual long-axis slices, which are radially placed, they acquired parallel images in the long axis. The slices with different orientations are considered as volume data of the same region with different resolutions. A reference model is registered with them simultaneously to overcome the insufficient sampling for each single volume data. Since most long-axis images are not parallel in MR acquisition, their method will require on additional protocol for heart reconstruction. van Assen et al. [108] proposed a left ventricle reconstruction algorithm based on multiple shape priors. Based on active shape models (ASMs), they first build a point distribution model from training shapes, and then fit this model to all the 2D images to refine the segmentation. The images generate forces on the intersection of the 3D model with the corresponding 2D plans. Similarly, sparse shape composition [128] is used to represent shape models based on sparse reconstruction. The methods, like ASM, represent the shapes based on a large number of training samples, but the training shapes are not always available in clinical applications.

To address the limitations in previous efforts to incorporate 2D slices with arbitrary orientations for 3D left ventricle reconstruction, we introduce a new reconstruction framework. The main contributions of the work are as follows. First, all the slices are segmented simultaneously with a 3D left ventricle model. The 2D contours are just the projection of the model on the corresponding images, so we handle the inconsistency among all the contours, i.e., the short- and long-axis contours are not exactly intersected. Second, there are no restrictions on the position and orientation of each slice. Any additional slice will help improve the segmentation accuracy and robustness. Third, only an elastic shape prior [19] is required

in our framework. The reference shape can be generated with one sample data or built manually by expert without any sample. Different from the methods based on multiple shape priors, which ensure that the shape follows a point distribution model, we constrain the non-rigid deformation of the reference shape. The 3D shape regularization term is integrated into all the 2D image segmentations to form a unified problem, which is efficiently solved by our proposed alternating optimization algorithm.

### 3.4.1 Model Reconstruction based on Sparse MR Images with Arbitrary Orientations

Given a group of 2D cardiac MR images $I_i$, which have known transformations $T_i$ to the 3D anatomical coordinate system, we expect to reconstruct a 3D left ventricle shape model $T(S_{ref})$, where $S_{ref}$ is a reference left ventricle model and $T$ is a non-rigid transformation. The projection of the reconstructed model $T(S_{ref})$ onto image $I_i$ is defined as $P_i(T(S_{ref}))$. It should match with the left ventricle area in the image. The fitness of the model to each image $I_i$ is measured by the energy function $E_{img}$. Since the slices are sparse in the 3D volume, the reconstruction problem is under constrained with only the image information. Therefore, we further assume the model is deformed from the reference model $S_{ref}$ with a smooth non-rigid deformation $T$. The model reconstruction is formulated as the following optimization problem:

$$\min_{T}\{\sum_{i} E_{img}(P_i(T(S_{ref})), I_i) + \gamma R(T)\} \tag{3.1}$$

where $E_{img}$ is the energy term for the fitness to each image $I_i$, $R(T)$ is the regularization term for the deformation $T$ and $\gamma$ is a trade-off parameter.

The image energy term $E_{img}$ is defined based on both the shape and appearance information. The conventional active contour models focus only on the boundaries

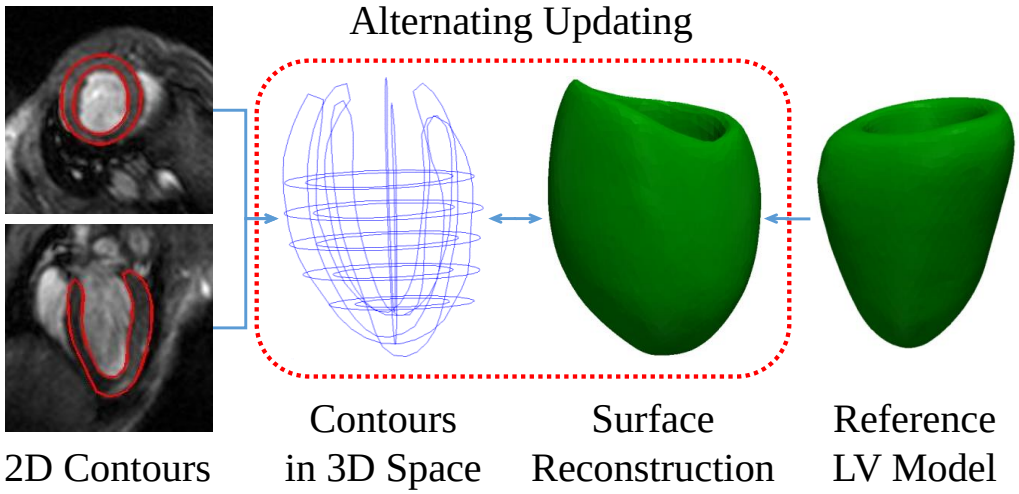


Figure 3.3: The pipeline of our 3D left ventricle system. The 3D surface model is deformed from a reference model to fit 2D contours, while the 2D contours is constrained by both image cues and 3D model prior. They are updated alternatingly to reconstruct the left ventricle model.

of the models. They deform the contours to fit locations that have high probabilities to be boundaries. In our model, we also consider the appearance of the interior region. The appearance statistics are adaptively learned during the deformation. The model is updated based not only on the edge information, but also the region statistics to ensure the appearance consistency of the new territory. The region-based deformable model is defined based on free form deformation. Instead of deformable contours, the whole interior region is deformed to optimize both the edge and the region energy function:

$$E_{img} = E_{edg} + \mu E_{reg} \tag{3.2}$$

where $E_{edg}$ is the edge energy term, $E_{reg}$ is the region energy term and $\mu$ is a constant that balances the contributions from the two terms. In our formulation, we are able to omit the model smoothness term in 2D images since the whole model smoothness is regularized by the smooth non-rigid transformation of the 3D model.

The model is attracted to edge feature with high image gradient via the edge energy term $E_{edg}$. A distance map to the edge feature is built based on gradient vector field [115]. The edge force moves the contour to the minimum of the distance map. Therefore, the edge energy term $E_{edg}$ is defined as:

$$E_{edg} = \int_C \Phi(\mathbf{x}) d\mathbf{x} \tag{3.3}$$

where $C$ is the contour in a 2D image and $\Phi$ is the distance map function.

The probability of each pixel belonging to the model is defined based on the interior intensity distribution from last iteration. The region energy term deform the model toward areas with high probability. It is defined as:

$$E_{reg} = \int_R \log P(\mathbf{x}) d\mathbf{x} \tag{3.4}$$

where $R$ is the interior region of the contour and $P$ is the probability of each pixel as the interior region of the model.

The 2D contours are projections of one 3D left ventricle model to the corresponding images. Therefore, different from the 2D deformation regularization term in previous segmentation algorithms, we employ a 3D shape prior to constrain all the 2D segmentations simultaneously. The 3D model is defined based on the deformation of a reference left ventricle model $T(S_{ref})$. We regularize the non-rigid deformation $T$ to ensure that the new model is still similar to the reference one. The smoothness of transformation $T$ is defined as:

$$R(T) = \int_{\mathbb{R}^3} \frac{\tilde{T}(\tilde{\mathbf{x}})}{\tilde{G}(\tilde{\mathbf{x}})} d\tilde{\mathbf{x}} \tag{3.5}$$

where $G$ is Gaussian kernel function and $\tilde{G}$ is its Fourier transform. Function $\tilde{T}$ indicates the Fourier transform of the deformation function $T$ and $\tilde{\mathbf{x}}$ is a frequency domain variable. Gaussian kernel is used as a low-pass filter to regularize the high

**Algorithm 1** 3D left ventricle reconstruction

**Input**: The sparse images $I_i$ with arbitrary orientation, and the reference left ventricle model $S_{ref}$
**Output**: The data-specific 3D left ventricle model
Initialize the 2D contours $C_i$ with graph cuts
**repeat**
  Transform the contours $C_i$ to 3D anatomic space
  Deform the 3D reference model $S_{ref}$ based on (3.7)
  Find the model-plane intersections $P_i(T(S_{ref}))$
  Deform the contours $C_i$ based on (3.8)
**until** $C_i$ and $T$ converge.

frequency part of the deformation and enforce the smoothness.

### 3.4.2 Deformable Model Implementations

The image forces are only defined on the intersection of the model in each plane. They are not applied directly to the vertices of the model. Therefore, we introduce the contours of the left ventricle on the images $C_i$ and reformulate the energy function as:

$$\min_{C_i,T}\{\sum_i [E_{img}(C_i, I_i) + \lambda D(C_i, P_i(T(S_{ref})))] + \gamma R(T)\} \tag{3.6}$$

where $D$ is the distance between the contour $C_i$ and the projection of the left ventricle model $P_i(T(S_{ref}))$. In this formulation, instead of deforming the reference model directly, the image forces only deform the 2D contours. Therefore, the whole energy function is separated into two parts. The 2D contours and the 3D model can be optimized alternatingly with Algorithm 1.

We initialize the 2D segmentation via graph cuts [9, 10]. It is very effective to generate a coarse segmentation, while it requires lots of interaction to refine the result. In our work, we use a two-stage segmentation for short-axis images based on its donut shape [107]. We use only a few strokes to indicate the blood pool. Then

the left ventricle is automatically segmented with no further interaction. Furthermore, the long-axis images are also segmented via graph cuts, which initialized based on its relative position with short-axis images. The regional segmentation results on all the images are then translated into boundary ones and refined by Metamorphs [107].

The initial contours are first transformed to the 3D anatomic space. Then assuming the contours $C_i$ are fixed, the reference left ventricle model is deformed to the contours. The energy function is reduced to:

$$\min_{T}\{\lambda \sum_{i} D(C_i, P_i(T(S_{ref}))) + \gamma R(T)\} \tag{3.7}$$

We use coherent point drift [71] to optimize (3.7). The result model maintains the shape of the reference model, and balances the differences among the contours in different slices.

The deformed model $T(S_{ref})$ is then projected to the 2D spaces. We use them as shape priors and optimize the contours $C_i$. In this step, the energy function is independent for each slice:

$$\min_{C_i}\{E_{img}(C_i, I_i) + \lambda D(C_i, P_i(T(S_{ref})))\} \tag{3.8}$$

where the distance function $D$ are defined by the distance maps of the model projection on the slices. This will make the contours more consistent with the left ventricle model.

During the alternating optimization, the parameter $\lambda$ will increase to further enforce the consistency between the left ventricle model and all the contours. When $\lambda \to \infty$, the alternating algorithm (3.6) will converge to (3.1).

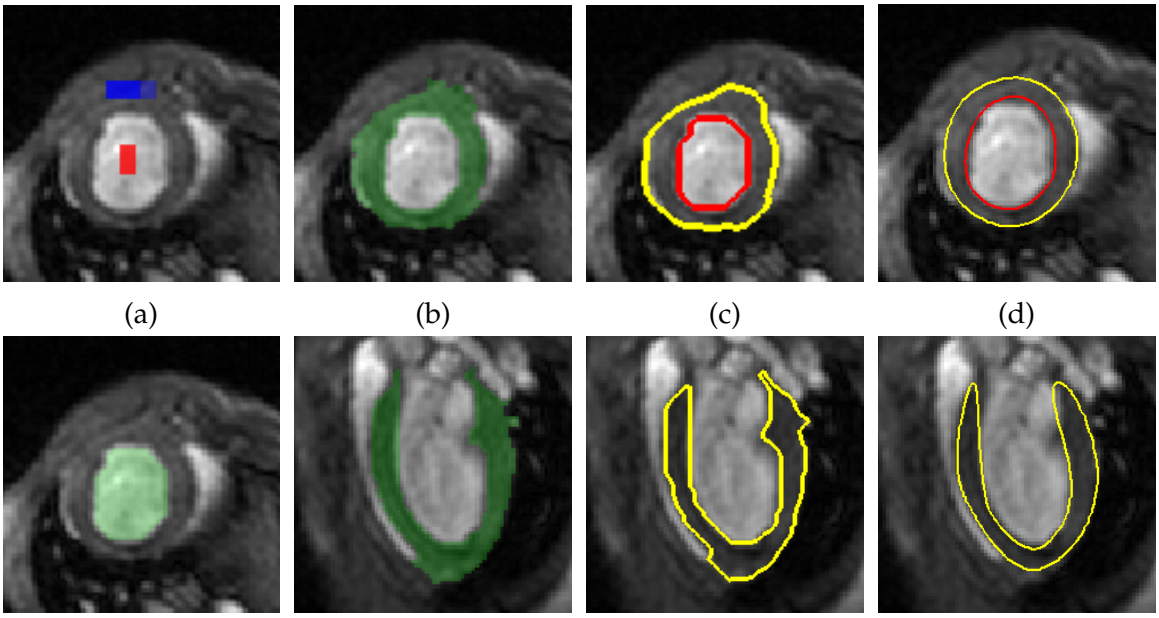

(a) (b) (c) (d)

(e) (f) (g) (h)

Figure 3.4: (a) The initial label for graph cuts, (e) the blood pool segmentation result, (b, f) the left ventricle region (green) from graph cuts on both short- and long-axis images, (c, g) the boundaries based on graph cuts and (d, h) the finial result based on our framework.

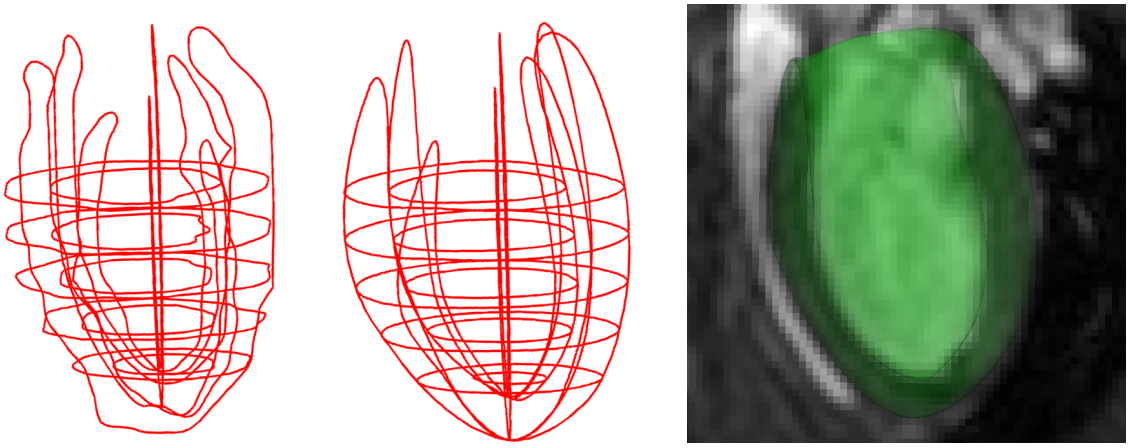

(a) Initial contours (b) Result contours (c) Result model

Figure 3.5: (a) The initial 2D contours mapped onto 3D anatomic space, (b) the result contours after deformation based on our framework and (c) the resulted 3D model embedded onto a long-axis image.

### 3.4.3 Evaluation

We test our reconstruction algorithm on mouse cardiac MR images. Sparse short- and long-axis images are acquired from the C57BL/6 mice. For each data, there are four to six short-axis slices that are parallel to each other with equal intervals, and four long-axis slices that are radially spaced every 45°. Their positions in the anatomic space are recorded during the acquisition.

We use a few strokes inside and outside the blood pool area, as shown in Fig. 3.4a, to initialize the segmentation, and get the blood pool area in Fig. 3.4e. This step is relatively stable due to the high intensity difference between the blood and heart wall. Then the region just outside the blood pool is set as the left ventricle. Graph cuts is used to produce a rough segmentation of the left ventricle on both short- and long-axis images. The result of this step often leaks out to other tissues due to the similar intensity among them (Fig. 3.4b, f). It consequently affects the corresponding boundaries refined by Metamorphs, which cannot correct the region with heavy leak (Fig. 3.4c, g). Our proposed deformable model overcome these problems with 3D shape constraints. It achieves better segmentation result in 2D images (Fig. 3.4d, h).

We apply our alternating reconstruction algorithm to generate 3D left ventricle model based on the initial 2D contours. It is noticeable in Fig. 3.5a that the contours from the short- and long-axis images do not intersect with each other based on only 2D information. Our model introduces a 3D shape model to regularize all the contours. It improves the the 2D segmentation results on different slices (Fig. 3.4d, h). Meanwhile, different from the initial contours projected into anatomic space, the our results balance their differences and make them consistent with each other (Fig. 3.5b). The 3D left ventricle model is also constructed based on our model. It is embedded into a long axis image in Fig. 3.5c. The model is smooth and match left ventricle wall in the image.

Our proposed framework for 3D left ventricle reconstruction uses sparse short- and long-axis images based on only one shape prior. Less MR images are required to acquire by using our method. This is not only very important for mouse cardiac imaging, but also desired for human data acquisition, since it will reduce the potential risk of strong magnetic field and improve the patient's comfort. In the future, we will test our framework on human cardiac MR data. Meanwhile, we will introduce a left ventricle detection module to substitute graph cuts-based initialization and build a fully automatic system.

## 3.5 Landmark motion tracking

Tagged MRI is widely used in clinical diagnosis to locate regions of dysfunction in the left ventricle wall [15]. It generates an MRI-visible tagging pattern on the cardiac muscle. The tagging lines deform with the tissue in vivo and provide kinematic information of the heart wall in a cardiac cycle. The motion of the material points can be reconstructed based on the combination of tag motion information from many images generated at different locations and different time points. This can be further used to estimate the mechanic properties of the cardiac muscle. As the first step of motion estimation, tagging line tracking plays a crucial role in improving accuracy of the cardiac motion analysis.

There have been many methods proposed for tagged MR image analysis [109]. MRI tagging produces line pattern with low image intensity on the MR images. Several methods have been proposed to extract the tagging lines based on low intensity. The deformable models [22, 82] are used to directly model the deformation of the tagging lines. They track the low intensity regions, and maintain the tagging line smoothness. Other methods estimate dense displacement field on the whole

image. Conventionally, it can be tracked with optical flow technique, while additional brightness adjusting is required to overcome the sharpness reducing of the MR image [30, 41]. The free form deformation is also used to find a deformation field based on cross-correlation between image patches [17], which is less sensitive to the brightness change.

The tagging line structure will produce peaks around the harmonic frequencies of the tag. The traditional MR image usually has only one peak in the frequency domain, which is near zero. The tagging pattern produces additional peaks at high frequencies. Harmonic phase (HARP) [75, 76] band-pass filters the images around the first harmonic. This intrinsically implies that the image can be modeled by sine waves locally at each pixel, whose frequency is similar to that of the initial tags. Since the frequencies and the orientations of the sine waves vary at different pixels, a relatively wide band-pass filter is usually used in HARP. Arts et al. proposed a local sine wave model (SinMod) [1] to estimate the frequency of each pixel on the direction perpendicular to the tags. This improves the robustness of the phase map under large deformation which comes along with large change of the frequency. Gabor filters are used to further estimate the orientation of the local sine wave [21]. A Gabor filter bank is a set of filters with parameters corresponding to various frequencies and orientations. By finding the optimized parameters that maximize filter responses, it improves the stability of the tagging line extraction under large deformation. However, the frequency and orientation are optimized independently at each pixel in [21]. As a result, the spatial discontinuity will occur in their estimation. Consequently, this will cause errors in displacement calculation.

In order to overcome this problem, we propose a new type of deformable models, which we term Gabor deformable models, to improve the results obtained by the local Gabor filters. Compared to HARP, which provides only one

best-estimated phase at each point, Gabor filters can provide various responses at one point based on their frequencies. The stronger response means that the filter matches better with the local sine wave. Meanwhile, the sine waves change smoothly on continuous tissues, so do the frequencies of their corresponding Gabor filters. This enables our deformable models to select the best local Gabor filter based on not only its response, but also its continuity. The smoothly changing Gabor filters further help to improve the smoothness of the phases. In addition, the frequency of a local Gabor filter can be used to estimate the period of the tagging patterns. This further constrains the distance between the tagging lines. Based on above-mentioned properties, we design our novel Gabor deformable models to track the tagging line motion on cardiac MR images. Extensive experiments have been designed to evaluate this method.

### 3.5.1 Tagging Line with Gabor Deformable Models

In this section, we will first introduce the Gabor filter and some of its promising properties. Then, we will present a tagging line tracking based on deformable models and extend it with Gabor filter.

#### Gabor Filter

Daugman first introduced Gabor filter to image analysis [27]. He found that the cells in the mammalian visual system can be modeled by Gabor functions. This discovery encourages more research on applying Gabor filter to various computer vision applications, like texture segmentation [112] and image enhancing [117].

Gabor filter is a product of an elliptical Gaussian kernel and a sinusoidal plan wave in the spatial domain. It can be written as

$$h(x,y) = s(x,y)g(x,y),$$

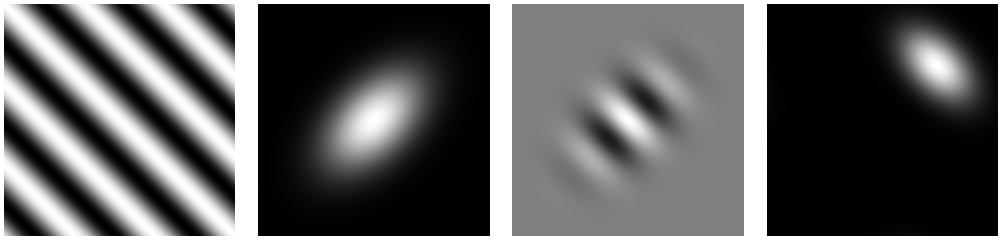

(a) (b) (c) (d)

Figure 3.6: A sample Gabor filter: (a) the real part of sinusoid, (b) the Gaussian envelope, (c) the real part of the Gabor function in space domain and (d) the magnitude of the Gabor filter in the frequency domain.

where $g(x, y)$ is a Gaussian function in Fig. 3.6a, known as envelope, $s(x, y)$ is a complex sinusoidal function in Fig. 3.6b, known as carrier. The 2D Gaussian function is defined as

$$g(x, y) = \frac{1}{2\pi\sigma_x\sigma_y} e^{-\left(\frac{x^2}{\sigma_x^2} + \frac{y^2}{\sigma_y^2}\right)},$$

where $\sigma_x$ and $\sigma_y$ are the sharpness of the Gaussian function. The complex sinusoidal function is defined as

$$s(x, y) = e^{-j2\pi(ux+vy)},$$

where $(u, v)$ is the frequency of the 2D complex sinusoid. The complex sinusoid only affects the argument of the filter. The magnitude of the filter is solely based on the Gaussian function, which monotonously decreases from the center. Meanwhile, the magnitude of the Gabor filter in frequency domain is also a Gaussian function centering at the frequency $(u, v)$ in Fig. 3.6d. This makes it satisfy the minimum space-bandwidth product per the uncertainty principle. It means that the Gabor filter achieves the best balance between the spatial and frequent domain support.

By adjusting the frequency and orientation of the Gabor filter, we can produce different responses at the same point. The strength of the response depends on the local tagging patterns. Stronger response means that the filter better fits the intrinsic frequency at this point. The tagging patterns usually vary on the whole

image, so do the Gabor filters with the optimized responses. Therefore, it is not the best choice to apply a global filter on the whole image, like HARP. In order to overcome the inconsistency of the frequency among pixels, a larger band-pass filter is designed in HARP to acquire the entire signal inside a reasonable frequency region. However, this introduces more noise into the phase estimation. Differently, the Gabor filter estimates the local frequency, which allows us to choose best filter at each point.

**Previous work: Intensity based Deformable Models**

Deformable models have been used in tagging line tracking. The tagging lines have low intensity in the MR images. This line pattern can be tracked by a set of deformable curves. Suppose that there are $m$ horizontal tagging lines on a cardiac image. The vertical tagging lines can be processed by rotating the image. The tagging lines are modeled by a set of splines. Each of them has $n$ control points that are evenly sampled along the horizontal direction. For a control point $(x_j^i, y_j^i)$, the horizontal coordinate $x_j^i$ is fixed and only the vertical coordinate $y_j^i$ moves during the deformation. The tagging lines deform based on the image information and the smoothness constraints. They are optimized by a combined energy function with image term $E_I$ and smoothness term $E_S$. The image term $E_I$ minimizes the intensities on all the control points, which is defined as

$$E_I = \sum_{i=1,j=1}^{m,n} I(x_j^i, y_j^i)^2.$$

The smoothness term $E_S$ regularizes the shape of the tagging lines by minimizing the first and second order derivatives of the splines. It is defined as

$$E_S = \alpha \sum_{i=1,j=2}^{m,n} \|y_j^i - y_{j-1}^i\|^2 + \beta \sum_{i=1,j=2}^{m,n-1} \|y_{j-1}^i - 2y_j^i + y_{j+1}^i\|^2,$$

where $\alpha$ and $\beta$ control the weights of the first and second order terms.

The intensity-based deformable models are sensitive to image noise. The tracking result may vibrate on a straight tagging line or even drift to its neighbors due to large deformation. Therefore, we integrate Gabor filter into the deformable models to improve the robustness of tagging line detection and constrain the gaps between tagging lines.

**Proposed New Method: Gabor Deformable Models**

Previous work used the best Gabor filters for each pixel to estimate their phases [21]. They produced a phase map similar to that from HARP. The points with a specific phase form the tagging lines. However, the lines generated based the above phase map often have branches due to the image noise. To deal with this problem, we employ a deformable model to optimize both the responses and the continuity of the Gabor filters along the tagging lines. On each control point, the Gabor filter is selected based on the phase and the magnitude of the response. This changes the image term $E_I$ to

$$E_I = \sum_{i=1,j=1}^{m,n} \{\| \arg(h(x_j^i, y_j^i, u_j^i, v_j^i)) - \phi_0\|^2 + \|h(x_j^i, y_j^i, u_j^i, v_j^i)\|^2\},$$

where $\arg(h(\cdot))$ is the phase of Gabor filter response, $\phi_0$ is the desired phase, and $\|h(\cdot)\|$ is the strength of the response. The response depends on both the position $(x_j^i, y_j^i)$ and the Gabor filter frequency $(u_j^i, v_j^i)$.

In addition to the point-wise response, the frequency of the Gabor filter is also required to change smoothly during the deformation. It is regularized in a similar way as the spline. The smoothness of the Gabor filter is defined as

$$\begin{aligned} E_S =& \alpha \sum_{i=1,j=1}^{m,n} \{\|u_j^i - u_{j-1}^i\|^2 + \|v_j^i - v_{j-1}^i\|^2\} \\ &+ \beta \sum_{i=1,j=1}^{m,n} \{\|u_{j-1}^i - 2u_j^i + u_{j+1}^i\|^2 + \|v_{j-1}^i - 2v_j^i + v_{j+1}^i\|^2\}. \end{aligned}$$

The frequency of the chosen Gabor filter is close to the frequency of the tagging pattern. It is the reciprocal of the distance between tagging lines. The higher the frequency means that the tagging lines are closer to each other, and the lower the frequency means that the tagging lines are further away from each other. We use the estimated frequency to constrain the distances between tagging lines. This introduces another term $E_D$ for tagging line gaps as

$$E_D = \sum_{i=1,j=1}^{m,n} \|(y_j^i - y_j^{i-1}) - \frac{1}{v_j^i}\|^2,$$

where the vertical distance $\|y_j^i - y_j^{i-1}\|$ should be similar to the estimation from the vertical frequency $v_j^i$. This effectively prevents two nearby splines sticking with each other. The combined energy with all above-mentioned terms can be defined as

$$E = E_I + E_S + E_D.$$

We minimize this energy function with block coordinate gradient descent (BCGD). The variables are separated into two blocks. The frequencies of the Gabor filters are solved based on fixed tagging line position. Then, we optimize the position of the tagging line based on fixed Gabor filter. Each iteration consists of making a gradient step with respect to each block in a cyclic order.

**Initialization**: The deformable models need a reasonable initialization. For the first frame, we assume that they only have small displacement from the initial tags generated from the magnetic field, which are a group of straight lines with equation distance in between. The gap between the lines is estimated by the reciprocal of the first harmonic frequency peak. In the following frames, the tagging lines are initialized based on those in the previous frame.

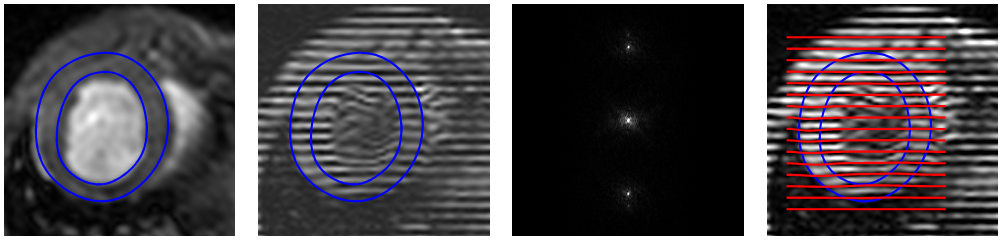

(a) Cine image (b) Tagged image (c) Frequency (d) Initial tags

Figure 3.7: The left ventricle is segmented on cine MR image. (a) and (b) are segmentation result on the first frame. The tagging lines on the first frame are then initialized based on the first harmonic peak after Fourier transform.

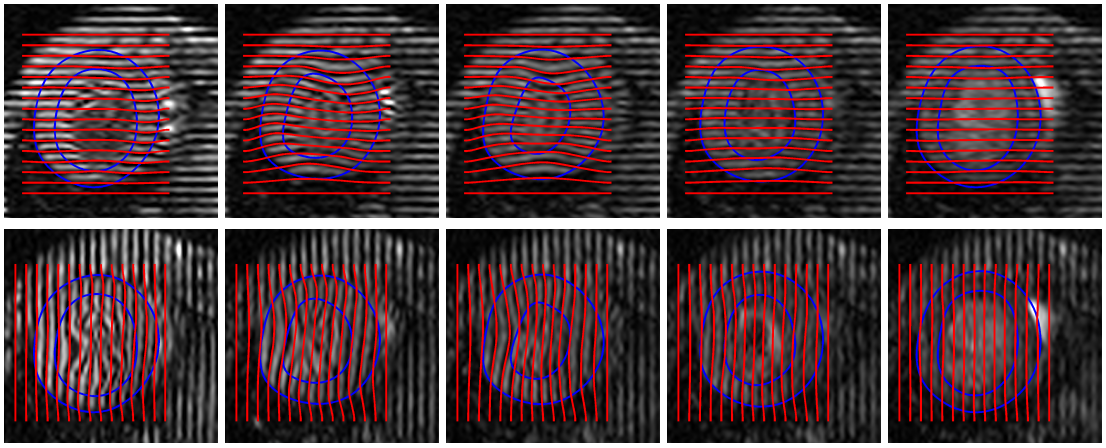

Figure 3.8: The tagging line extraction result on both horizontal and vertical tagged MR images in a cardiac cycle.

### 3.5.2 Evaluation

We applied our proposed method to track the LV motion of the mouse heart [131]. We carried out the experiments on 19 groups of short-axis MR image sequences in a cardiac cycle. They were acquired from different parts of the heart on three C57BL/6 mouse subjects. All the images were generated on a 4.7T Varian INOVA system. One group of image sequences is acquired at the same position. It contains one cine MR sequence and two tagged MR sequences with tagging lines perpendicular to each other. The image size were all $256 \times 256$, and the numbers of time frames varied from 11 to 15.

The left ventricle is manually segmented by experts. Then based on the first

harmonic peak in Fig. 3.7c, the tagging line are initialized on the first frame in Fig. 3.7d. The Gabor filter-based tracking algorithm is used to tagging line motion in the whole cardiac MR sequence. The tracking result is shown in Fig. 3.8. The tagging lines deforms based on the local Gabor filters inside the left ventricle wall. They maintain well both the spatial and temporal continuity following the heart motion.

A novel method is present here to extract the tagging line motion from tagged cardiac MR images. The Gabor filter is utilized to estimate the local displacement as well as tagging frequency. The continuity is enforced on both the displacement field and the Gabor filter. This enables us to estimate more accurately the tagging line motion. In the future, we will extend the tagging line tracking to the dense displacement field estimation. This will introduce more 2D constraints on the displacement. We also expect to add the influence of the adjacent slices to the model to reconstruct a 3D deformation model.

## 3.6 Meshless Deformable Models

The meshless models are used to deform the initial model based on the control points. They are widely used in problems with large deformations and nonlinear material behavior. Different from the traditional mesh-based approaches, the meshless model abandons the grid or mesh structures, and uses only the particles to represent the model [69]. Therefore, the complex and sensitive mesh generation process is eliminated.

### 3.6.1 Meshless volume representation

The meshless representation is used in our left ventricle model. In a discrete deformable model, the displacements are defined on all the nodes distributed in the

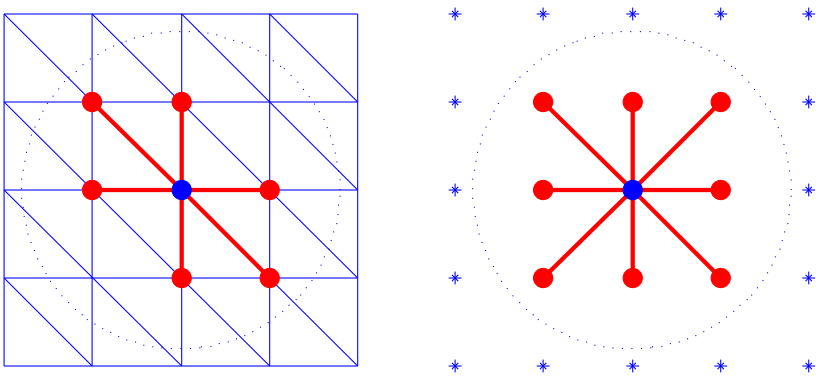

(a) Mesh model of grid (b) Meshless model of grid

Figure 3.9: The point set is represented as (a) mesh and (b) meshless models. The neighborhood is defined by the connectivity in mesh model, and the distance in meshless one.

models. The displacements of all the points are estimated based on the nodes. For example, in finite element method, the displacement of a point is defined by element contains it. In meshless models, the displacement of a point is defined based on its neighborhood. Given a point $i$ and its neighbor $j$, we use a polynomial kernel to compute the weight connecting them:

$$w_{ij} = W(|\mathbf{v}_j - \mathbf{v}_i|, h_i) \tag{3.9}$$

$$W(r,h) = \begin{cases} \frac{315}{64\pi h^9}(h^2 - r^2)^3 & \text{if } r < h \\ 0 & \text{otherwise.} \end{cases} \tag{3.10}$$

where $r$ is the distance from point $j$ to $i$, and $h$ is the support of the sphere kernel. The influence between point $i$ and $j$ becomes weaker as the distance is larger, and becomes zero when the distance is larger than $h_i$. Therefore, the neighbors of a point $i$ are all the points within distance $h_i$ (Fig.3.9b). However, in the mesh structure (Fig.3.9a), a degenerated mesh may have neighbor points with very large distance.

Consider a 3D meshless model with material points as $\mathbf{x} = (x, y, z)^T$. Each point has a displacement $\mathbf{u} = (u, v, w)^T$. The coordinates of a point before and

after the deformation are $\mathbf{x}$ and $\mathbf{x}+\mathbf{u}$, respectively. In order to computer strain, stress and elastic force on each point, we first need to calculate the gradient of the displacement field $\nabla\mathbf{u}$. We use moving least square algorithm (MLSA) with a linear basis to estimate the deformations. Let us consider the x-component $u$ of the displacement field $\mathbf{u}=(u,v,w)^T$, and the value $u_i$ at node $i$. Then, $u(\mathbf{x})$ can be defined as:

$$u(\mathbf{x})=\sum_{k=1}^{m}p_k(\mathbf{x})a_k(\mathbf{x})=\mathbf{p}^T(\mathbf{x})\mathbf{a}(\mathbf{x}) \tag{3.11}$$

where $\mathbf{p}(\mathbf{x})$ is basis functions, and $m$ is the number of bases. We use linear basis function in our work, while high order terms are also allowed in the model. $\mathbf{a}(\mathbf{x})$ is the unknown parameter vector that will be estimated. The error of this approximation is measured by the weighted sum of square differences between the estimated values $\tilde{u}_j$ and the measured values $u_j$:

$$e=\sum_j w(\|\mathbf{x}_j-\mathbf{x}\|_2)(\mathbf{p}^T(\mathbf{x})\mathbf{a}(\mathbf{x})-u_j)^2 \tag{3.12}$$

where node $j$ are the neighbors of point $\mathbf{x}$, and $w(\cdot)$ is the kernel function Eq.3.10. The unknowns $\mathbf{a}(\mathbf{x})$ are solved by least squares. Thus, the displacement field is:

$$u(\mathbf{x})=\sum_j(\mathbf{p}^TA^{-1}(\mathbf{x})B_j(\mathbf{x}))u_j=\sum_j\Phi_j(\mathbf{x})u_j \tag{3.13}$$

where

$$A(\mathbf{x})=\sum_j w(\|\mathbf{x}_j-\mathbf{x}\|_2)\mathbf{p}(\mathbf{x}_j)\mathbf{p}^T(\mathbf{x}_j) \tag{3.14}$$

$$B(\mathbf{x})=w(\|\mathbf{x}_j-\mathbf{x}\|_2)\mathbf{p}(\mathbf{x}_j) \tag{3.15}$$

and $\Phi_j$ is the shape function of node $j$. The x-component derivative of the shape function is defined as:

$$\Phi_{j,x}=(\mathbf{p}^TA^{-1}B_j)_{,x} \tag{3.16}$$

$$=\mathbf{p}_{,x}^TA^{-1}B_j+\mathbf{p}^T(A^{-1})_{,x}B_j+\mathbf{p}^TA^{-1}B_{j,x} \tag{3.17}$$

where

$$B_{j,x}(\mathbf{x}) = \frac{dw}{dx}(\|\mathbf{x}_j - \mathbf{x}\|_2)\mathbf{p}(\mathbf{x}_j) \tag{3.18}$$

and

$$A_{,x}^{-1} = -A^{-1}A_{,x}A^{-1} \tag{3.19}$$

$$= -A^{-1}\sum_j \frac{dw}{dx}(\|\mathbf{x}_j - \mathbf{x}\|_2)\mathbf{p}(\mathbf{x}_j)\mathbf{p}^T(\mathbf{x}_j)A^{-1} \tag{3.20}$$

The myocardium will produce internal forces due to the derivative of the displacement field $\nabla u = (u_{,x}, u_{,y}, u_{,z})$. The forces will prevent the heart from large deformation and finally deform the heart wall back to initial shape.

### 3.6.2 Meshless Model with Nonlinear Laplacian Kernel

Different from the traditional simulation methods, the meshless model abandons the grid or mesh structures, using only the particles to represent the model [69]. It is widely used in problems with large deformations and nonlinear material behavior. Meanwhile, the complex and sensitive mesh generation process is eliminated. The material point is considered as the center of the phyxel which is a sphere with radial decreasing mass distribution. Given a dense phyxel representation, any point on the model is expressed as the weighted average of all the phyxels whose ranges cover this position. The mechanical properties, like mass and density, are all able to be defined in this manner.

Many deformable models have been proposed under the meshless framework. Usually, some kinds of internal forces are used to express the interactions among the phyxels based on the special material properties. The myocardial wall is considered as nearly incompressible, which is experimentally proved that the volume change is no more than 4% [109]. So we propose a constraint that all the material points tend to keep the distances to the nearby points. Similar constraint has been used for surface mesh based deformation in [98] to preserve the surface detail,

while we use it to maintain the shape on 3D volume meshless model. In the neighborhood of any vertex $i$, the distance-preserve deformation can be approximated as rotation:

$$\mathbf{x}'_i - \mathbf{x}'_j = \mathbf{R}_i(\mathbf{x}_i - \mathbf{x}_j) + \varepsilon, \forall j \in \mathcal{N}(i). \tag{3.21}$$

where $\mathbf{x}_i$ and $\mathbf{x}'_i$ are the positions of the vertex $i$ at the initial and the following frame, $\mathbf{R}_i$ is the rotation matrix at the vertex $i$, and $\mathcal{N}(i)$ is the neighborhood of the vertex $i$. The actual movement of the point set may not be presented as rotation. However, a deformation under the proposed constraint can be archived by minimizing the error $\varepsilon$. Given the positions of the control points after deformation, positions of all the material points will be calculated by minimizing the following energy function:

$$\min_{\mathbf{x}',\mathbf{R}} \sum_{i=1}^{n} \sum_{j \in \mathcal{N}(i)} \omega_{ij} ||(\mathbf{x}'_i - \mathbf{x}'_j) - \mathbf{R}_i(\mathbf{x}_i - \mathbf{x}_j)||^2 \tag{3.22}$$
$$\text{s.t. } \mathbf{x}'_k = \mathbf{c}_k, k \in \mathcal{F}$$

where $\omega_{ij}$ is a fixed weight based on the positions of the two points in the initial frame, and $\mathcal{F}$ is the set of indices of the control points with position $c_k$. The energy term for each phyxel is related to the Laplacian coordinate change under rotation only. The Laplacian coordinate was also used in [110], where the scaling and rotation matrix was used for transformation. But only the linear components were estimated to approximate the rotation, which limits the method suitable for small deformation. The nonlinear model usually achieves better accuracy with more complex computation. In our work, the nonlinear system can be efficiently solved by iteratively optimizing the position and the rotation matrices.

Given the position $\mathbf{x}'$ after the deformation, the optimal rotation $\mathbf{R}_i$ can be solved separately for each vertex $i$. We define the weighted covariance matrix

Figure 3.10: Non-linear meshless deformation

**Input**: the positions of the initial points $\mathbf{x}$, and the control points $\mathbf{c}$
**Output**: the positions $\mathbf{x}'$ after deformation
precalculate the weight $\omega_{ij}$, and the initial guess $\mathbf{x}'_0$
**repeat**
  for each $i$, calculate local rotation $\mathbf{R}_i$ from $\mathbf{S}_i$ in (3.23)
  solve linear system (3.24) to get the new position $\mathbf{x}'$
  for all $k \in \mathcal{F}$, set $\mathbf{x}'_k$ as $\mathbf{c}_k$
**until** $\mathbf{x}'$ converges.

between the initial and deformed positions around the vertex $i$ as:

$$\mathbf{S}_i = \sum_{j \in \mathcal{N}(j)} \omega_{ij}(\mathbf{x}_i - \mathbf{x}_j)(\mathbf{x}'_i - \mathbf{x}'_j)^T \tag{3.23}$$

Supposing the singular value decomposition of $\mathbf{S}_i$ is $\mathbf{U}_i \blacksquare_i \mathbf{V}_i^T$, $\mathbf{R}_i$ can be derived as $\mathbf{R}_i = \mathbf{V}_i \mathbf{U}_i^T$ with changing the sign of some columns in $\mathbf{U}_i$, such that $\det(\mathbf{R}_i) > 0$.

Then with the updated optimal rotation matrix $\mathbf{R}$, the minimum of (3.22) can be achieved by the following linear functions for all the vertex $i$:

$$\sum_{j \in \mathcal{N}(i)} \omega_{ij}(\mathbf{x}'_i - \mathbf{x}'_j) = \sum_{j \in \mathcal{N}(i)} \frac{\omega_{ij}}{2}(\mathbf{R}_i + \mathbf{R}_j)(\mathbf{x}_i - \mathbf{x}_j) \tag{3.24}$$

All the linear functions can build a sparse linear system, with the Laplace operator applied to $\mathbf{x}'$. The control points will always keep their given positions, while the positions of the other points will be updated based on the solution of the linear system. Based on the above method, $\mathbf{x}'$ and $\mathbf{R}$ are solved iteratively. So with an initial guess of the positions $\mathbf{x}'_0$, we are able to solve the non-linear problem by algorithm 3.10.

### 3.6.3 Strain Analysis

The strain is a description of the relative displacement in the body. It is close related to the gradient of the displacement field $\nabla \mathbf{u}$, where $\mathbf{u}_i = \mathbf{x}'_i - \mathbf{x}_i$ is the displacement of points. Based on the moving least square method, the displacement field

for the point $i$ is expressed in its neighborhood as:

$$\nabla \mathbf{u}|_{\mathbf{x}_i} = \mathbf{A}^{-1} \left( \sum_j (\mathbf{x}_j - \mathbf{x}_i)(\mathbf{u}_j - \mathbf{u}_i)^T \omega_{ij} \right),$$

where $A = \sum_j (\mathbf{x}_j - \mathbf{x}_i)(\mathbf{x}_j - \mathbf{x}_i)^T \omega_{ij}$ is the moment matrix, which is based solely on the initial model. Then, the Jacobian matrix of the deformation is then defined as:

$$\mathbf{J} = \mathbf{I} + \nabla \mathbf{u}^T = \begin{bmatrix} u_{,x} + 1 & u_{,y} & u_{,z} \\ v_{,x} & v_{,y} + 1 & v_{,z} \\ w_{,x} & w_{,y} & w_{,z} + 1 \end{bmatrix} \tag{3.25}$$

The Green-Lagrangian strain tensor $\boldsymbol{\varepsilon}$ is:

$$\boldsymbol{\varepsilon} = \frac{1}{2}(\mathbf{J}^T \mathbf{J} - \mathbf{I}) = \frac{1}{2}(\nabla \mathbf{u} + \nabla \mathbf{u}^T + \nabla \mathbf{u} \nabla \mathbf{u}^T).$$

In the strain tensor $\varepsilon$, there are only six different terms due to symmetry. The diagonal terms are the normal strains on three perpendicular directions, and the others are the shear strains.

### 3.6.4 Experiments

**Experimental settings:** The C57BL/6 mice were examined on a 4.7T Varian INOVA system. Both of the SPAMM tagged images and cine image were acquired within the whole cardiac cycle. Two sets of tagged SA images were acquired with tagging planes perpendicular to each other in each slice. Then, four slices in LA views were chosen radially spaced every 45°. The tagging plane on the LA slices were parallel to the SA. This made the three tagging planes all perpendicular to each other, which is the minimum requirement for the reconstruction of the 3D motion for the heart. The non-tagged images were also acquired for both the LA and SA slices mentioned above at the same time step as the tagged ones, which were used for the segmentation of the heart boundary.

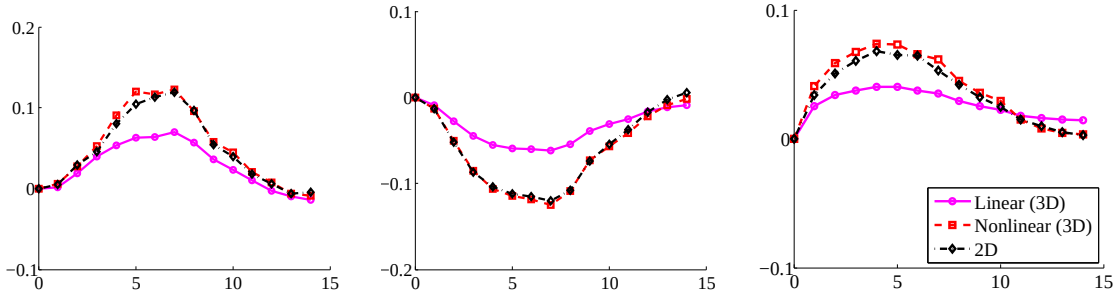


(a) $E_{rr}$ (b) $E_{cc}$ (c) $E_{rc}$

Figure 3.11: Comparing the 3D strains from the linear [110] and our nonlinear models with the 2D strains in a cardiac cycle, including radial stain ($E_{rr}$), circumferential strain ($E_{cc}$) and radial-circumferential strain ($E_{rc}$). The 2D strains are generated based on the movement of intersection points on the SA.

We compare the global strains calculated from our deformation method with that from the 2D mouse heart analysis in [133] and the linear 3D deformation method in [110]. In [133], the strains were calculated based on the movement of the intersection points on the SA slices. Thus, only the 2D SA strains are available. In [110], the LV model is deformed based on linear Laplacian kernel.

In Fig. 3.11, the radial, circumferential and radial-circumferential shear strains from the linear [110] and our nonlinear models are compared with the corresponding 2D strains from [133]. The resulting strains of the nonlinear model are similar to the 2D ones, with average difference 5%, while the differences from the linear model are around 40%. The reason is that the heart deformation can not be well simulated by the linear kernel. The nonlinear Laplacian kernel in our work is more accurate in this problem.

The strains related to longitudinal direction are not able to be estimated based on 2D intersection point movement. The 3D methods naturally present them. The strains outside the SA slices are shown in Fig. 3.12. Similar to the other strains, the nonlinear kernel gives larger strains. The magnitude of the strains from the linear kernel is less than 50% of that from nonlinear model. Similar to the SA results, the linear kernel tends to underestimate the magnitude of the strains.

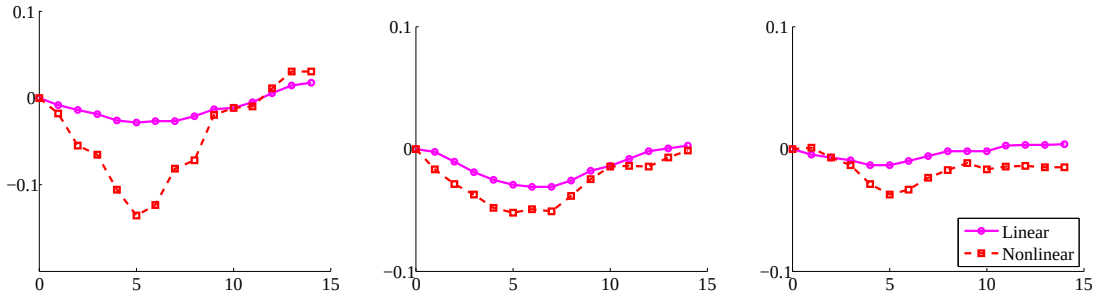


(a) $E_{ll}$ (b) $E_{rl}$ (c) $E_{cl}$

Figure 3.12: The comparison between 3D strains from the linear [110] and nonlinear models in a cardiac cycle, including longitudinal strain ($E_{ll}$), radial-longitudinal strain ($E_{rl}$) and circumferential-longitudinal strain ($E_{cl}$). Note that 2D strains cannot cover these directions.

All the methods are implemented using C++ on an Intel i7 2.80GHz computer with 8GB RAM. The computing time for the nonlinear deformation on 15 frames (a cardiac cycle) is around 40 seconds, which is comparable to the linear one. The similar preprocesses which construct the Laplacian matrices for both methods take up the majority of the computing time. In addition, the iterative method to solve nonlinear Laplacian kernel often converges in less than ten steps. Therefore, our nonlinear deformation improves the simulation accuracy without sacrificing the computational efficiency.

## 3.7 Conclusion

In this section, we present a comprehensive framework for LV motion analysis from the tagged MRI. The whole process is optimized to stably track the movement of the heart during the cardiac cycle. The sparse 2D MR slices with arbitrary orientations are combined to reconstruct a 3D LV model with single shape prior. The tagging lines are tracked with deformable models based on Gabor filter banks. The 3D meshless LV model is built and deformed based on the nonlinear Laplacian kernel. The experiments show that it can simulate the LV motion better than

the linear one. Based on the deformable model, any local strains can be easily calculated, which enables us to analyze many global and local properties of the ventricular wall. In the future, we will further test and apply our method on various diseased models such as myocardial infarction. We will refine the deformable model by adding more constraints from the contours and the tagging lines.

# Chapter 4
# Sparse Deformable Models

Deformable models integrate bottom-up information derived from image appearance cues and top-down prior knowledge of the shape. They have been widely used with success in medical image analysis. One limitation of traditional deformable models is that the information extracted from the image data may contain gross errors, which adversely affect the deformation accuracy. To alleviate this issue, we introduce a new family of deformable models that are inspired from compressed sensing, a technique for accurate signal reconstruction by harnessing some sparseness priors. In this section, we employ sparsity constraints to handle the outliers or gross errors, and integrate them seamlessly with deformable models. The proposed new formulation is applied to the analysis of cardiac motion using tagged magnetic resonance imaging (tMRI), where the automated tagging line tracking results are often very noisy due to the poor image quality. Our new deformable models track the heart motion robustly, and the resulting strains are consistent with those calculated from manual labels.

## 4.1 Introduction

Physics-based deformable models and their variations have been studied extensively in recent decades and are widely used in computer vision, computer graphics and medical image analysis [63, 65, 67, 74]. They are able to solve diverse types

of problems, such as, but not limited to, image segmentation [52], image registration [89, 91], shape reconstruction [66, 102], and motion analysis [64, 80]. The name "deformable models" is derived from nonrigid body mechanics, which describes how elastic objects respond to applied forces. Starting from an initial shape, the model is usually deformed by two types of forces, i.e., internal and external forces. The external force drives the model to fit the observations, while the internal force constrains the geometric flexibility of the shape. For example, in the image segmentation problem, the external force computed from the image intensity drives the model to the estimated boundary, while the internal force keeps the boundary smooth. In motion analysis (e.g., cardiac motions [20, 42, 46, 83, 109]) and shape manipulation problems [74], *control points* are employed as the external force to drive the model, and the internal force maintains the smoothness and preserves shape details. The control points are tracked along a motion sequence, and then an initial model is deformed to fit the control points in each following frame. This is often measured by the distances between the control points and the corresponding points on the initial model. In fact, in the context of motion analysis and shape manipulation, many previous methods [97, 110, 116, 132] use Euclidean distance or $L2$ norm as the distance metric for penalty functions. This assumes intrinsically that the errors of the target points follow a Gaussian distribution with small variances. Nevertheless, this is not always true in practice. Since the control points are usually derived from automated detections, they may contain not only Gaussian noise, but also some gross errors or outliers due to erroneous detections. Therefore, the accuracy of the traditional deformable models depends heavily on the accuracy of the control point detection.

In this section, we focus on improving the robustness of traditional deformable models, particularly for the problems of cardiac motion analysis. Inspired by the robust recovery power of the compressed sensing approach [11, 29], we propose

a new class of deformable models using sparse regularization. Recent research in compressed sensing shows that using an $L1$ norm can dramatically increase the probability of accurate signal recovery, even when there are both sparse outliers and moderate Gaussian noise [13]. Thus, we design a robust deformable model by integrating seamlessly an $L1$ norm regularization with a modified Laplacian deformable model [97, 124]. This new model is able to handle outliers or gross errors. In addition, it is designed as a convex optimization problem, and can be efficiently solved within a constrained solution space. However, when the variances of the Gaussian noise are large, solely using the $L1$ norm may cause overfitting problems due to its nature of pursuing the sparse structure [12]. Therefore, we propose a deformable model using hybrid norm regularization that is able to handle both the Gaussian errors and gross errors. We also generalize these two models in a unified formulation, which we call *Sparse Deformable Models*.

In the following section, we discuss the relevant work of deformable models and compressed sensing. Our proposed sparse deformable models (SDM) are presented in detail in section 4.3. In section 4.4, we validate our models on a clinically important and challenging problem, i.e., the left ventricle (LV) motion analysis in mouse cardiac tagged MRI. The experimental results demonstrate the robustness of our models on mouse heart motion tracking even with inaccurate results of control point detection. The last section draws conclusions on model advantages, and discusses directions of future work.

## 4.2 Related Work

### 4.2.1 Deformable Models

With the success of active contour models [52], many methods have been proposed to improve deformable models. Most of the work focuses on either internal force

or external force. In this section, we introduce some relevant papers on these two aspects.

*Internal forces* usually enforce the smoothness characteristics of deformable models, such as the local deformation similarity. An unconstrained deformable model may easily result in unrealistic shapes due to weak or misleading image cues. Therefore, the internal force is critical for robustness. The global parametric models (e.g., deformable superquadratics) were proposed to build models based on a few global shape parameters [3, 100]. Although these models reduce the degrees of freedom dramatically, they have difficulty in capturing the shape details. The local geometry properties can be used as constraints to solve these problems. For examples, splines were used on image deformation to constrain the smoothness of the deformation field [105]. A piecewise-smooth finite element model (FEM) was employed to represent the deformable boundary [32, 33], which achieved real-time myocardial segmentation in both ultrasound and MRI data. Laplacian coordinates [97] have been also a well-known measurement approach for the local similarity. Comparing with spline- and FEM-based methods, Laplacian coordinates allow more flexible shape representation. [97] employed them to constrain the smoothness and local similarity of the 2D mesh deformation in shape editing. [92] decomposed the Laplacian coordinates into components in the perpendicular and tangential directions, to formulate a detail-preserved internal force. In this section, we adapt the traditional Laplacian coordinates in a new setting of *3D volumetric and meshless* deformable models to enforce the smoothness and local shape similarity.

*External forces* match the model to the observations derived from the image appearance. They are usually categorized as short-range and long-range forces. The short-range forces are defined based on the local information in a small neighborhood. For example, in segmentation problems, they drive the contour to the

estimated boundary. The boundary may be defined by the intensity, gradient change, or high response of boundary detectors [52]. In registration problems, the source image is deformed to match the target image according to the appearance similarity [31]. The pixels are matched based on textures in their neighborhoods. The long-range forces deform the model to match pre-calculated landmarks [101] or satisfy model priors [25]. Region appearance features have also been used [50, 51, 134] to augment the deformable models by leveraging the image intensity statistics. They discriminate the inside and outside region based on their intensities and textures. Recently, dictionary learning was also used to learn appearance characters [48, 49]. Each pixel is classified into different regions based on their reconstruction residues under different dictionaries. Our deformable model uses control points as the external force, which is a natural choice for cardiac motion analysis.

### 4.2.2 Robust Shape Priors

Most deformable models assume that there is no outlier or gross error on the detected landmarks, while such errors are very common due to the image noise or weak appearance cues. Statistical shape models, such as active shape models [26] and their variants, can effectively handle outliers using shape priors. Some of them detect and eliminate the outliers explicitly before the deformation. [34] proposed a method to detect outliers by hypothesis testing based on the point distribution model. The detected outliers are removed or replaced based on the mean shape of the model. [85] proposed to detect the abnormal regions by registering with a standard atlas. The regions largely different from the normal intensities are determined to be outliers. [54] used a local shape dissimilarity measure, which is invariant to scaling, rotation and translation, to detect the outliers, and then displaced them based on the local valid points. Other researchers aimed to reduce the

effect of the outliers during the model deformation. [88] evaluated M-estimator, least median of squares and random sample consensus (RANSAC) [36] to handle outliers in active shape models. RANSAC showed the best performance in the quantitative evaluation. [28] utilized wavelet transformation to build a hierarchical shape model to improve the local robustness. The low-frequency bands carry global shape information, and the high-frequency bands serve local smoothness constraints. Besides shape priors, image atlas-based methods also naturally have the properties of handling segmentation errors [94]. Priors can also be based on data-specific properties, e.g., the relative positions of multiple components, which are modeled by formulating the relation explicitly [81] or learning shape priors from examples [79].

Recently, compressed sensing methods have been intensively investigated. These methods aim to reconstruct a signal that is known to be compressible with certain transformations based on sparse measurements. Such sparse methods have been widely used in computer vision and image processing communities to deal with gross errors or outliers. Particularly, the sparse constraints have been employed to model shape priors effectively [129, 130] and register shapes robustly [45]. In their settings, most of the control points generated from point detectors are roughly accurate, while a small number of points may contain large errors. These points are represented as sparse outliers and optimized with sparsity regularization.

Most above-mentioned methods rely on the use of training samples, which are not always available in practice for deformable models. In addition, they are based on the *static* images or shapes to form an over-complete dictionary and assume that the target model can be sparsely reconstructed by the dictionary. Different from these above-mentioned methods, we propose to seamlessly integrate sparsity priors with deformable models to handle outliers *adaptively and dynamically* for a sequence of images. Therefore, there is no need for training data.

## 4.3 Methodology

Consider a set of points $\mathcal{V}$, where each point has a neighborhood structure[1], and a subset of $\mathcal{V}$ as control points $\mathcal{V}_c$ that are computed from the observations (e.g., tagging line tracking results). Denote the homogeneous coordinate of the point $i$ as $\mathbf{v}_i = [x_i, y_i, z_i, 1]^T$ and its position after deformation as $\mathbf{v}'_i = [x'_i, y'_i, z'_i]^T$, where $i = 1, 2, \cdots, n$. Then the coordinates of all the deformed points are represented as:

$$\mathbf{V}' = [\mathbf{v}_1'^T \mathbf{v}_2'^T \cdots \mathbf{v}_n'^T]^T. \tag{4.1}$$

The goal of our deformable models is to track the motion of the whole shape, given the position $\mathbf{V}'_c$ of control points $\mathcal{V}_c$. Instead of calculating the deformed point positions $\mathbf{V}'$ directly, we optimize the deformations $T$ for each point. The deformed position $\mathbf{v}'_i$ then can be derived by the relation $\mathbf{v}'_i = T_i \mathbf{v}_i$. It is easier to incorporate the shape constraints into the deformations than the point positions. This will be further discussed in the internal force. The deformation of each point $i$ is parameterized by an affine $3 \times 4$ transformation matrix $T_i$, where the first three columns are linear transformation and the last column is translation.

In our model, the internal force preserves the local shape structure by using the Laplacian coordinates, and the external force minimizes the difference between the shape and the control points via our proposed sparse constraints.

### 4.3.1 Internal Force

Our internal force ensures the local similarity by regularizing the differences of the transformation matrices between neighboring points. Instead of measuring the matrix distance directly, we measure the difference by the deformation they

[1] Mesh- and meshless-based models are the most widely used shape representations. Our model works for both representations. The neighborhood is defined by the connectivity for the mesh model, or the distance for the meshless model.

generate. Specifically, if a point is deformed using the transformation matrices of its neighboring points, the resulting displacements should be similar. In other words, for a point $i$, its displacement after applying its own transformation matrix $T_i$ should be similar to applying its neighbor's transformation matrix $T_j$. Thus, the energy function of the internal force is:

$$E_{int} = \sum_{i \in \mathcal{V}} \sum_{j \in \mathcal{N}(i)} w_{ij} \| T_i \mathbf{v}_i - T_j \mathbf{v}_i \|_2^2, \tag{4.2}$$

where$\| \cdot \|_2$ denotes the entry-wise matrix $L2$ norm[2], and weight $w_{ij}$ is the strength of connection between points $i$ and $j$. In the meshless model, it is defined by a kernel function, such as the polynomial kernel [70]:

$$w(r,h) = \frac{315}{64\pi h^9} \begin{cases} (h^2 - r^2)^3 & \text{if } r < h \\ 0 & \text{otherwise,} \end{cases} \tag{4.3}$$

where $r$ is the distance between points $i$ and $j$, and $h$ is the support of the kernel, which means that the kernel is non-zero only when $r < h$. The function only contains the square term of $r$. Since $r$ is defined as the square root of $\sum r_k^2$, where $r_k$ is the distance in the $k$th direction, this kernel eliminates the requirement of square root calculation.

The unconstrained transformation matrix $T_i$ is able to deform the local structure arbitrarily. This may produce some unnatural and unreasonable shapes to minimize the energy. For example, if all transformation matrices are zero matrices, points will be transformed to the origin. Thus, the whole model degenerates to a single point and the internal energy is zero. Although this complete degeneration may not happen in most applications because of the external force from the control points, the deformable models with unconstrained transformation will still lose geometry details in directions with less control points information, e.g.,

[2] The matrix norms in this section are all entry-wise norms.

the direction perpendicular to the surface [73]. To alleviate this problem, we restrict $T_i$ to translations, rotations and isotropic scales. In particular, we disallow the anisotropic scaling, which will remove local shape details.

The translations are defined explicitly in the last column of $T_i$, and rotations and isotropic scales are both represented in the linear transformation, which also contains other types of transformation that we do not expect in our model, e.g., anisotropic scales. Therefore, we define a special type of linear transformation containing only rotations and isotropic scales. Rotations are represented by multiplication with an orthogonal matrix, which is represented as the matrix exponential of a skew-symmetric matrix $\exp(H)$. In particular, $3 \times 3$ skew-symmetric matrices emulate a cross product with a vector, i.e., $H\mathbf{x} = \mathbf{h} \times \mathbf{x}$. Based on this property, one can derive the following expansion of the exponential above:

$$\exp(H) = \alpha I + \beta H + \gamma \mathbf{h}^T \mathbf{h}, \tag{4.4}$$

where $I$ and $H$ are linear terms, while $\mathbf{h}^T\mathbf{h}$ is quadratic. Adding the isotropic scale $s$ to the transformation, the class of matrices for linear part becomes $T = s\exp(H)$. Here, we keep only the linear term of the matrices and form the approximately constrained transformation as:

$$T_i = \begin{pmatrix} s & -h_1 & h_2 & p_x \\ h_1 & s & -h_3 & p_y \\ -h_2 & h_3 & s & p_z \end{pmatrix}. \tag{4.5}$$

In this matrix, $s$ is the isotropic scalar, $\mathbf{h}$ contains the non-zero parts of the skew-symmetric matrix, and $\mathbf{p}$ is the translation part. It is a good linear approximation for rotations with small angles.

Within this setting, we expect to find $T_i$ satisfies Eq.4.5, while minimizing the internal energy. In Eq.4.2, $T_i$ only appears in the structure $T_i\mathbf{v}_k$, where $k = i$ or in the neighborhood of point $i$. $T_i$ is a matrix and $\mathbf{v}_k$ is a vector in this function. In

order to enforce the constraint, we reformulate it to a function of $\mathbf{t}_i = (s_i, \mathbf{h}_i, \mathbf{p}_i)^T$, which is the vector of the unknowns in $T_i$. Thus, we substitute $T_i\mathbf{v}_k$ with $A_k\mathbf{t}_i^T$, where $A_k$ contains the position of $\mathbf{v}_k$. It is defined as:

$$A_k = \begin{pmatrix} v_{k_x} & 0 & v_{k_z} & -v_{k_y} & 1 & 0 & 0 \\ v_{k_y} & -v_{k_z} & 0 & v_{k_x} & 0 & 1 & 0 \\ v_{k_z} & v_{k_y} & -v_{k_x} & 0 & 0 & 0 & 1 \end{pmatrix}. \tag{4.6}$$

Thus, the internal force is reformed as

$$E_{int} = \sum_{i \in \mathcal{V}} \sum_{j \in \mathcal{N}(i)} w_{ij} \| A_i\mathbf{t}_i - A_i\mathbf{t}_j \|_2^2. \tag{4.7}$$

Since this is a summation of the quadratic forms of the transformation matrices $\mathbf{t}_i$, we can represent the energy function as a quadratic form of all the unknown transformations $\mathbf{t}$. In order to form the internal force, we encode the point position matrix $A_i$ into matrix $K_i$ as

$$K_i = M_i \otimes A_i, \tag{4.8}$$

where $\otimes$ is the Kronecker product, and $M_i$ is a $m_i \times n$ node-arc matrix of $\mathbf{v}_i$, where $m_i$ is the number of its neighbors. For each neighbor $\mathbf{v}_j$, there is one row in $M_i$ where the $i$th element is $w_{ij}$ and the $j$th element is $-w_{ij}$, while the other elements are all zeroes:

$$M_i = \begin{array}{c} \\ \cdots \\ \\ \end{array} \begin{array}{c} \overset{i\text{th column}}{} \\ w_{ij} \\ \vdots \end{array} \begin{array}{c} \\ \cdots \\ \\ \end{array} \begin{array}{c} \overset{j\text{th column}}{} \\ -w_{ij} \\ \vdots \end{array} \begin{array}{c} \\ \cdots \\ \\ \end{array}, j \in \mathcal{N}(\mathbf{v}_i). \tag{4.9}$$

$K_i\mathbf{t}$ is the difference of the displacements based on different transformations of the neighborhood of point $i$. We concatenate the matrix $K_i$ for all the points to form the matrix $K = [K_1^T K_2^T \cdots K_n^T]^T$. Thus, the energy function of the internal force (Eq.4.2) is formulated as:

$$E_{int} = \| K\mathbf{t} \|_2^2. \tag{4.10}$$

This energy function is a quadratic form of all the independent transformation unknowns. By solving this function, we directly get the transformation matrices for all the points, which contain only translation, rotation and isotropic scale. There is no need to regularize each transformation explicitly to the three types above. This setting of internal force is able to ensure the smoothness of the whole shape and preserve the local similarity. In addition, this internal force is intentionally designed as a convex optimization problem, so it can be coupled seamlessly with our sparsity-based external forces.

### 4.3.2 External Force

Besides the shape constraint from the internal force, the deformable model also aims to match the observations. For example, a point $i$ on the model is expected to fit the position of corresponding control point $\mathbf{v}'_i$ after deformation $\mathbf{t}_i$. In other words, $\mathbf{v}'_i = A_i\mathbf{t}_i$, where $A_i$ is the position of point $i$ defined above. We concatenate the point coordinates $A_i$ into an $3n \times 7n$ sparse matrix:

$$D = \begin{bmatrix} A_1 & & & \\ & A_2 & & \\ & & \ddots & \\ & & & A_n \end{bmatrix}, \tag{4.11}$$

where $\mathbf{V}' = D\mathbf{t}$ is the model deformation based on the transformation parameters $\mathbf{t}$. We use a control point indicator $c$ to select the rows of $D$ and $\mathbf{V}'$ corresponding to the control points. Thus, this deformable model is defined as:

$$\arg\min_{\mathbf{t}}\{\|K\mathbf{t}\|_2^2 + \lambda\|D_c\mathbf{t} - \mathbf{V}'_c\|_2^2\}, \tag{4.12}$$

where $\lambda$ is the stiffness weight, which controls how much the model is able to deform to match the control points. Larger $\lambda$ results in a better fitting, but the deformed shape may not be smooth. The $L2$ norm is used as a penalty function

in this formulation. This is also known as a Laplacian deformable model (LDM). Similar settings have been used in many applications, such as shape editing [97, 98] and cardiac modeling [111]. However, it may not be the most proper metric for certain problems, especially when there are gross errors or outliers.

**Sparsity Constraint Using $L1$ Norm**

Gross errors may easily happen in medical imaging problems, such as the erroneous detections in a noisy image. The $L2$ norm in Eq.4.12 follows a Gaussian distribution for residuals. It may overfit these sparse outliers, and hence adversely affect the deformation accuracy. It is desirable to model such sparse outliers during the deformation. The $L0$ norm counts the number of non-zero elements and can model such sparse errors exactly. Therefore, we can use it to capture the sparse outliers:

$$\begin{aligned} &\arg\min_{\mathbf{t}} \|K\mathbf{t}\|_2^2 \\ &s.t. \|D_c\mathbf{t} - \mathbf{V}_c'\|_0 < k, \end{aligned} \tag{4.13}$$

where $\|\cdot\|_0$ is the $L0$ norm and $k$ is the pre-defined maximum number of outliers. However, the $L0$ norm is non-convex, and solving an $L0$ norm problem is NP-hard. Although greedy methods [62, 104] can be employed to solve such problem, we do not know the sparsity number, i.e., the number of outliers, and different data may have different sparsity numbers. Therefore, in practice it is hard to use an $L0$ norm as the sparsity constraint in deformable models. Recent developments in compressed sensing [11] show that minimizing an $L1$ norm problem can produce a nearly identical sparse solution as using the $L0$ norm. Thus, we use convex relaxation to define a sparse deformable model based on the $L1$ norm (we use SDM-$L1$ to stand for Sparse Deformable Models with $L1$ norm regularization):

$$\arg\min_{\mathbf{t}} \{\|K\mathbf{t}\|_2^2 + \lambda\|D_c\mathbf{t} - \mathbf{V}_c'\|_1\}, \tag{4.14}$$

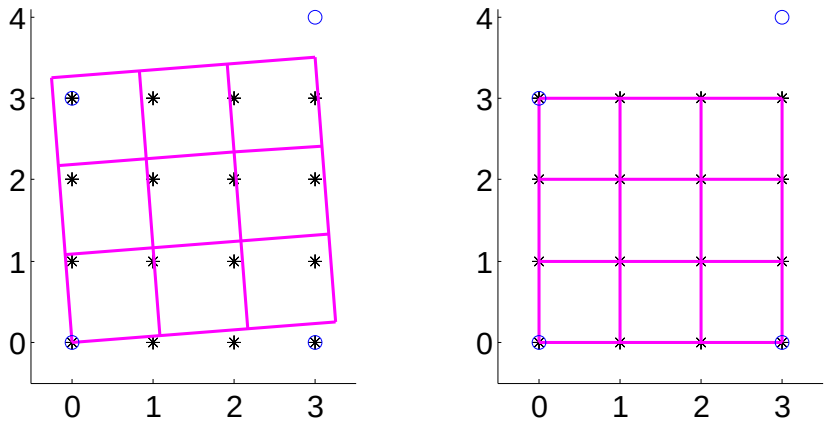


(a) $L2$ norm (b) $L1$ norm

Figure 4.1: The toy sample of the deformable model using $L2$ and $L1$ norm regularization. The circles are the observed control points with outliers. We fit a grid to control points. The stars are the desired result (ground truth).

where $\lambda$ is a constant and controls how sparse the outliers are. Different from sparsity number $k$, this $\lambda$ is more flexible as this is a soft constraint.

To illustrate intuitively the effectiveness of method, we test it on a toy example of shape deformation (Fig. 4.1). The initial model is a $4 \times 4$ grid with four-direction connection. Four corners are chosen as the control points, and the top-right one is an outlier, as shown in Fig. 4.1a. The deformable model aims to fit these four points while maintaining the original grid shape. The result using the $L2$ norm is adversely affected by the outlier, since the quadratic form of the energy function results in a large penalty on this outlier. We obtain a much more accurate result by using the $L1$ norm, since the linear constraint has a higher tolerance for gross errors.

### Sparsity Constraint Using Both $L1$ and $L2$ Norms

Similar sparsity constraints have been successfully applied in many applications, such as face recognition [114], background subtraction [43], and shape prior modeling [129]. However, in deformable models, the observations may still contain

Gaussian errors with large variations. Solely using the $L1$ norm may not be able to handle them well. Therefore, we combine both $L1$ and $L2$ norms, which assist our sparse deformable models to handle more general cases (we use SDM-$L1/L2$ to stand for the Sparse Deformable Model with both $L1$ and $L2$ norm regularization):

$$\arg\min_{\mathbf{t},\mathbf{e}}\{\|K\mathbf{t}\|_2^2 + \lambda\left(\|D_c\mathbf{t} - \mathbf{V}_c' - \mathbf{e}\|_2^2 + \gamma\|\mathbf{e}\|_1\right)\}, \tag{4.15}$$

where $\mathbf{e}$ represents the gross errors and is constrained by the $L1$ norm, and $\gamma \in [0,1]$ controls how sparse $\mathbf{e}$ is. The new model combines the advantages of both $L1$ and $L2$ norms, and is able to handle both gross errors and traditional Gaussion errors with large variations. In fact, this model is closely related to the other models by adjusting the parameters $\lambda$ and $\gamma$. If $\gamma$ is extremely large, $\mathbf{e}$ will be all zeros. Thus, the model degenerates to a method with only an $L2$ norm, as in Eq.4.12, and it is sensitive to gross errors. If $\lambda$ is extremely large and $\gamma$ is small, the deformation errors will be approximately equal to $\mathbf{e}$. Thus, the model is similar to the one with only sparse constraints, as in Eq.4.14. It will be robust to the outliers, but cannot handle large Gaussian noise. Therefore, Eq.4.15 is actually a general form of these models. In addition, it is also closely related to the Huber norm, which has been used in statistics for robust estimation. It is defined as:

$$\rho(x) = \begin{cases} x^2 & |x| \le \gamma \\ 2\gamma|x| - \gamma^2 & |x| > \gamma. \end{cases} \tag{4.16}$$

The Huber norm is similar to the $L2$ norm when the errors are smaller than $\gamma$, and similar to the $L1$ one when the errors are larger than $\gamma$. Therefore, it effectively models both the Gaussian noise and the outliers. Using the notation of the Huber norm, SDM-$L1/L2$ can be rewritten as:

$$\arg\min_{\mathbf{t}}\{\|K\mathbf{t}\|_2^2 + \lambda\|D_c\mathbf{t} - \mathbf{V}_c'\|_{\text{Huber}}\}. \tag{4.17}$$

Besides handling different types of errors, another benefit of this deformable model is the convexity and the continuous first-order derivative. Therefore, the

above problem can be solved efficiently using our proposed algorithm introduced below.

**Optimization Framework**

Although the above problem can be solved by the standard convex optimization algorithms, such as interior point method [39], we propose an effective optimization algorithm that fully utilizes the special structure of this problem. We alternately optimize two variables $\mathbf{t}$ and $\mathbf{e}$. These two subproblems both have analytical solutions. They can be solved efficiently in each iteration. The results converge quickly in our experiments. We initialize the gross error $\mathbf{e}$ as zero and apply our alternating algorithm to the problem. In the first step, when $\mathbf{e}$ is fixed, the problem is reduced to the conventional $L2$ norm regularization:

$$\arg\min_{\mathbf{t}}\{\|K\mathbf{t}\|_2^2 + \lambda\|D_c\mathbf{t} - \mathbf{V}_c' - \mathbf{e}\|_2^2\}. \tag{4.18}$$

It can be solved by least square minimization. In the second step, $\mathbf{t}$ is fixed, and the optimization problems for each term $e_i$ of the outlier $\mathbf{e}$ are independent:

$$\arg\min_{e_i}\{\left((D_c\mathbf{t})_i - \mathbf{V}_{ci}' - e_i\right)^2 + \gamma|e_i|\}, \tag{4.19}$$

where $(D_c\mathbf{t})_i$ is the $i$th element of the vector $D_c\mathbf{t}$. The minima for the two parts can be achieved at $(D_c\mathbf{t})_i - \mathbf{V}_{ci}'$ and 0, respectively. The minimum of the energy function must lie between them, since both of them are convex. Therefore, $e_i$ has the same sign as $(D_c\mathbf{t})_i - \mathbf{V}_{ci}'$. After determining the sign of $e_i$, the problem reduces to a constrained quadratic function of $e_i$, and the solution is:

$$e_i = \begin{cases} \max\{0, (D_c\mathbf{t})_i - \mathbf{V}_{ci}' - \gamma/2\} & \text{if } (D_c\mathbf{t})_i - \mathbf{V}_{ci}' \geq 0 \\ \min\{0, (D_c\mathbf{t})_i - \mathbf{V}_{ci}' + \gamma/2\} & \text{otherwise.} \end{cases} \tag{4.20}$$

Since there are analytical solutions for both of the sub-steps in our algorithm,

the energy function will monotonically decrease to a minimum solution. The convexity of the whole problem makes sure that this is the global solution of the problem.

## 4.4 Experiments

### 4.4.1 Validation on Synthetic Data

Our methods were validated on synthetic 3D volumes with pre-defined deformation. Three methods were compared: 1) Laplacian deformable models (LDM) [97, 110], 2) sparse deformable models with $L1$ norm regularization (SDM-$L1$), and 3) sparse deformable models with both $L1$ and $L2$ norm regularization (SDM-$L1/L2$). First, an LV volume model was generated, with the internal points evenly distributed in short- and long-axis directions. Ten percent of short-axis slices with equal intervals were chosen as the control points. Then random global transformations were applied to this model, such as scaling, rotation and twisting. Two types of errors were also applied to the deformed model to simulate the noisy tracking results. Gaussian noise was added to all control points, and a few points were selected randomly and large displacements were applied to simulate gross errors. Based on the displacements of the control points, deformable models were employed to reconstruct the displacements of the other points. The deformable models were tested under different parameter setting and different noise intensities. In each parameter setting, we randomly generated 1000 samples and calculated the mean and variance of deformation errors.

We first analyzed the deformation errors when changing the coefficient $\gamma$, reflecting the balance between the $L1$ and $L2$ norms (Fig. 4.2a). The deformation error is large when $\gamma$ is close to zero, and reduces dramatically when $\gamma$ is a little larger. Since SDM-$L1/L2$ is similar to SDM-$L1$ when $\gamma$ is small, it indicates that

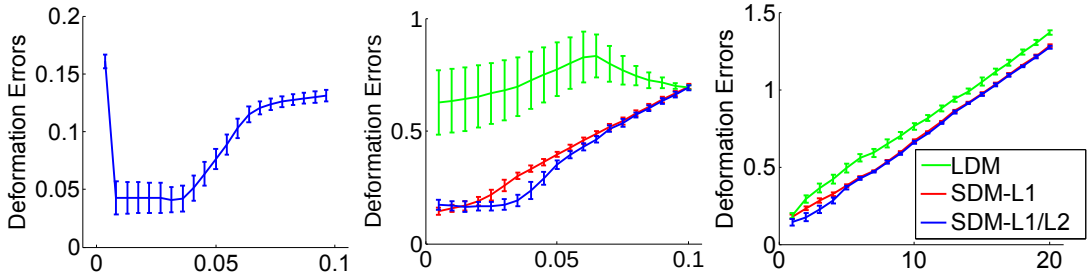


(a) $L1$ coefficient: $\gamma$ (b) $\sigma$ of Gaussian error (c) Number of outliers

Figure 4.2: (a) shows the deformation errors related to the coefficient $\gamma$ of the $L1$ norm. (b) and (c) show the deformation errors of different deformable models (errors are measured in millimeters). They are compared under different Gaussian noise variances and numbers of outliers, respectively. SDM-$L1/L2$ out-performs the other two most of the time, while the SDM-$L1$ norm is better when the Gaussian noise intensity is small.

SDM-$L1$ cannot handle Gaussian error properly. As $\gamma$ becomes even larger, the mean error increases again. It becomes stable when $\gamma$ is large enough, which is similar to the result of LDM. The results show that SDM-$L1/L2$ outperforms the other models that use only one type of norm. Theoretically, the model achieves the best result when the threshold $\gamma$ is similar to the variance of Gaussian noise. However, it is hard to measure the noise variance exactly in real data. Therefore, we set it to one tenth of the median of the neighborhood distances empirically and it shows good results.

We also tested our sparse deformable model under different noise intensities. First, we increased the variance of Gaussian noise with fixed outliers. In Fig. 4.2b, SDM-$L1$ performs the best when the noise intensity is low. As the variance increases, SDM-$L1/L2$ outperforms the others. LDM is always the worst, due to the

Table 4.1: Quantitative evaluation of deformation errors (Unit: mm).

| Method | Average | Min | Max | Median |
|---|---|---|---|---|
| LDM | 1.036 | 0.724 | 1.635 | 0.927 |
| SDM-$L1$ | 2.107 | 0.437 | 3.580 | 2.069 |
| SDM-$L1/L2$ | 0.482 | 0.341 | 0.719 | 0.469 |

outliers. It shows that our model is more stable when handling moderate Gaussian noise. Then we tested the models with different numbers of outliers. In Fig. 4.2c, the errors of all models increase almost linearly with the number of outliers. SDM-$L1/L2$, which is still the best among them, performs better than SDM-$L1$ when there are a few outliers. They achieve similar errors when the outliers are dominant. Both of the experiments show that SDM-$L1/L2$ is more stable under different noisy conditions.

### 4.4.2 Motion Analysis of Mouse LV

We also tested our method on mouse myocardial strain analysis. The strain computation is especially sensitive to tracking outliers. Even when there are only small amounts of outliers in deformation, the strains on points near these outliers will be highly affected. To obtain the ground truth, we manually labeled the tagging lines in each 2D image, and then used the tag motion to drive a 3D LV volume model based on the finite element method (FEM). This approach is very accurate. However, manual labeling is time-consuming and tedious, and FEM is not very efficient. In this experiment, we used this method as a reference, and compared our models using automatic tagging line tracking results that contain outliers. We compared the LDM, SDM-$L1$ and SDM-$L1/L2$. Table 4.1 shows the deformation errors of different models on 17 datasets. SDM with the combined norm has smallest average error owing to its robustness to outliers. Meanwhile, the results of SDM-$L1$ are much less stable than other two methods. The reason is perhaps that there is strong Gaussian noise in real data.

To further analyze the regional LV motion, we divide the LV into 17 segments, based on the standardized myocardial segmentation of the American Heart Association [16]. The heart was first sectioned into apical, mid-cavity, and basal parts perpendicular to the left ventricular long axis. Each part was further segmented

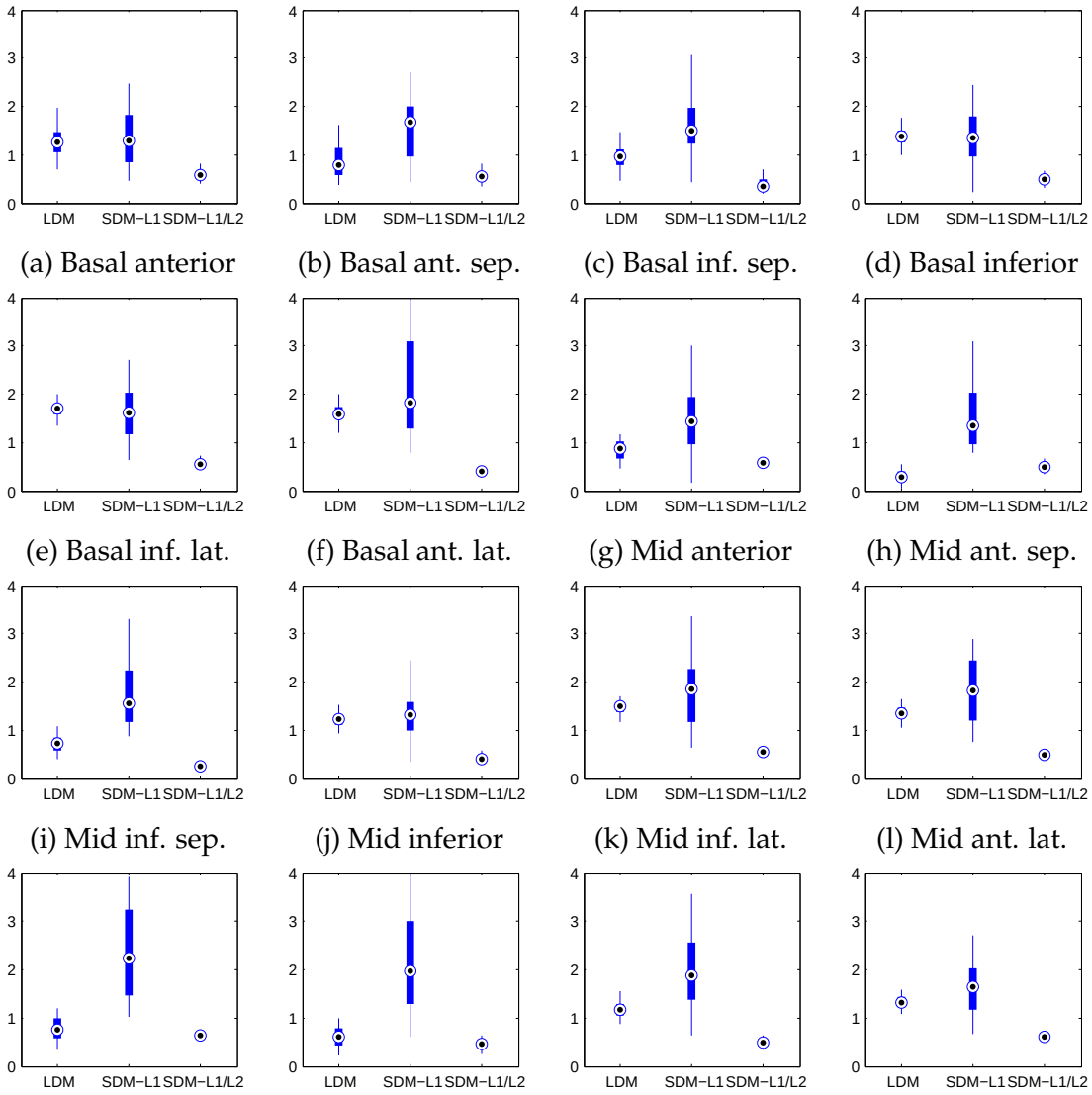


(a) Basal anterior (b) Basal ant. sep. (c) Basal inf. sep. (d) Basal inferior

(e) Basal inf. lat. (f) Basal ant. lat. (g) Mid anterior (h) Mid ant. sep.

(i) Mid inf. sep. (j) Mid inferior (k) Mid inf. lat. (l) Mid ant. lat.

(m) Apical ant. (n) Apical septal (o) Apical inferior (p) Apical lateral

Figure 4.3: Box plot of the errors for different deformable models. In each box plot, the central mark is the median, the edges of the box are the 25th and 75th percentiles, and the whiskers extend to the extreme data points. The unit of Y-Axis is millimeters. X-axis shows three compared methods: LDM, SDM-$L1$ and SDM-$L1/L2$.

based on different short-axis directions. We compared the deformation errors on all the segments. Fig. 4.3 shows 16 of them (excepting the true apex segment). The results show that SDM-$L1/L2$ always has the best accuracy, i.e., small average deformation errors and standard deviation. In contrast, SDM-$L1$ has the worst

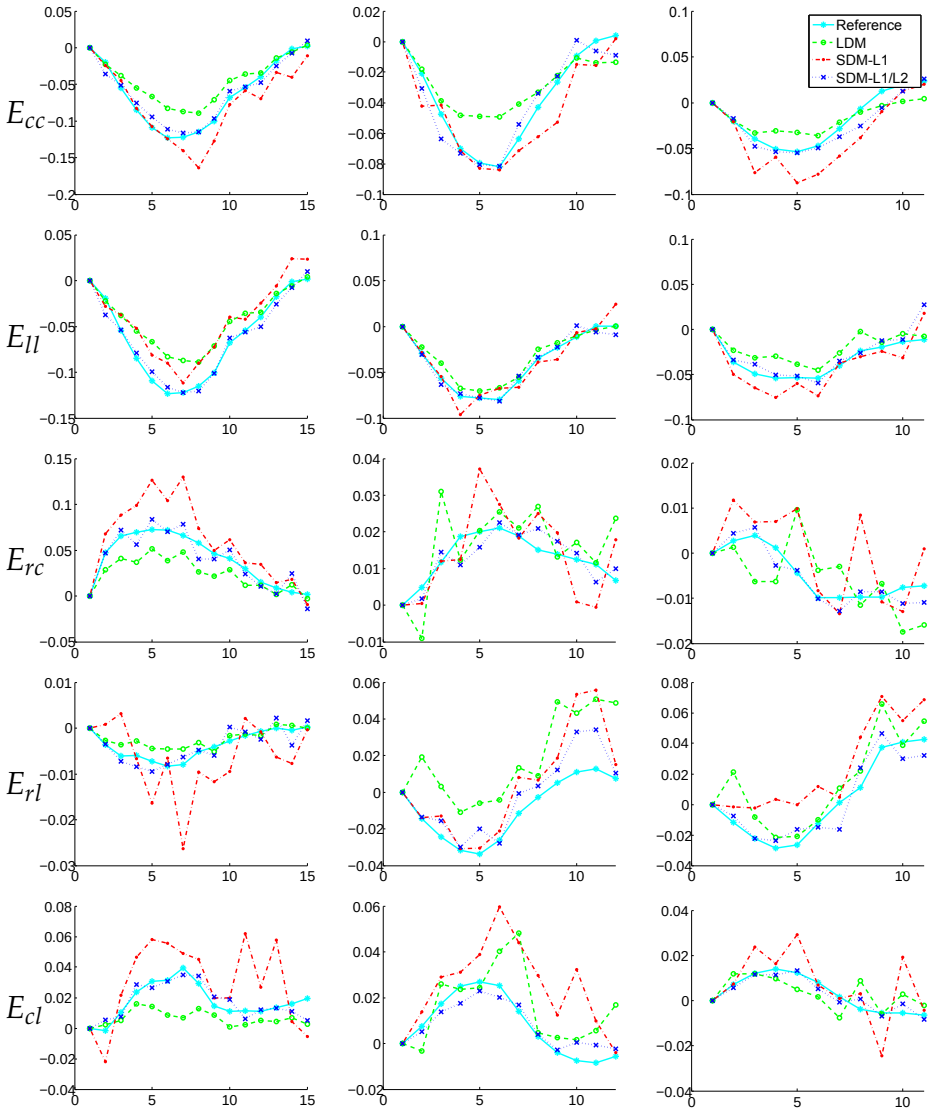


Figure 4.4: Comparison of the strains generated from different deformable models with the reference model in three mouse cardiac data. Each column represents one dataset, and each row represents one type of strain. In each figure, y-axis is the strain, and x-axis means the frame in a cardiac cycle.

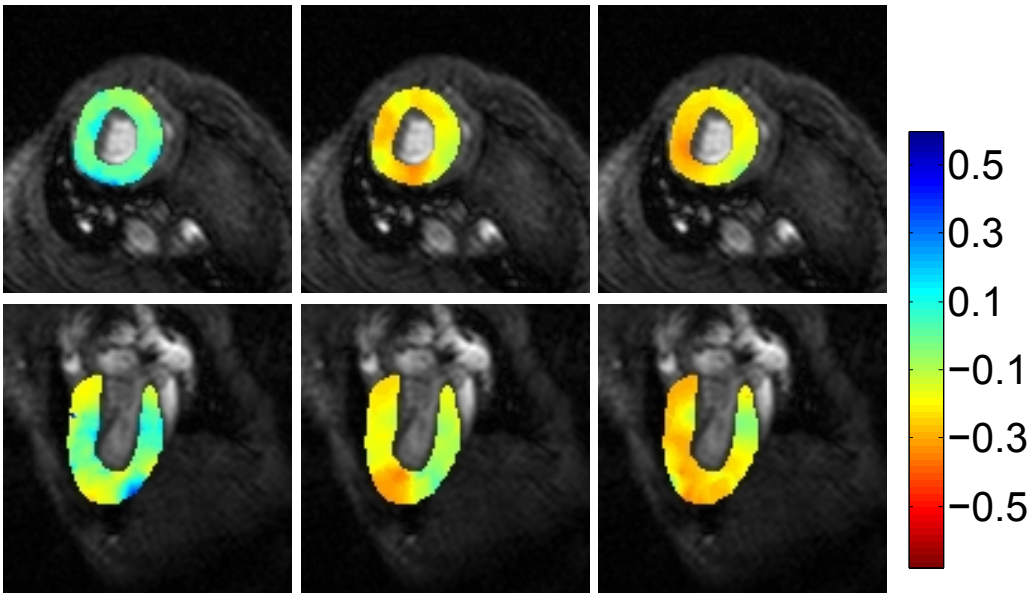


Figure 4.5: The first row is the short-axis slice, and the second row is the long-axis slice. The three columns are colored by the radial, circumferential and longitudinal strains, respectively.

accuracy in both aspects. Comparing among different parts based on the short-axis directions, the lateral parts have relatively larger errors than the septal parts. This may because the lateral parts have larger movements. Comparing along the long-axis direction, the basal part has relative larger errors in all the methods. The reason is that there are no short-axis slices in this part. All the point movements are calculated based on the control points from the middle part. The free ends at the basal boundaries produce more errors than other parts. The errors are smaller in the middle and apical parts in the results of LDM and SDM-$L1/L2$ due to the dense control points. However, they are still large for SDM-$L1$ in these parts. This shows that using the $L1$ norm alone cannot represent the noisy tracking errors well, and the $L2$ norm is necessary in handling this data.

We also computed the myocardial strains over a cardiac cycle, which are commonly used to describe the strength of the heart motion. The strains were decomposed into radial, circumferential, and longitude directions, and the shear strains

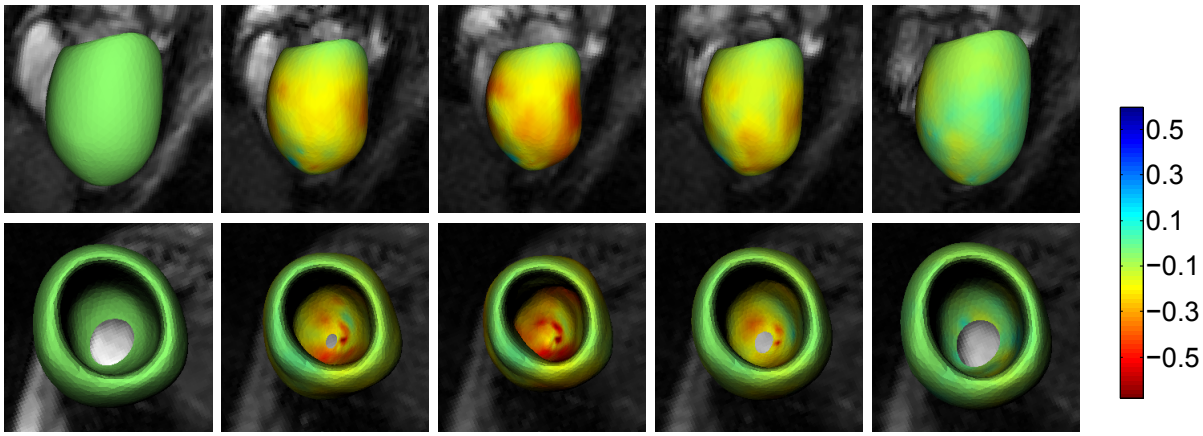


Figure 4.6: The deformations of the LV on a cardiac cycle are colored by the circumferential strain.

among them. Fig. 4.4 provides the comparisons of the strains generated with different deformable models on several mouse datasets. The rows correspond to different types of strains, and the columns correspond to different mice. Each figure contains the strains generated from different models in a cardiac cycle. The numbers of frames in the cardiac cycles may be different in each mouse because of the acquisition procedures. The first column is from a healthy mouse, and the other two are from mice with myocardial infarctions. It is shown that the strains generated from the healthy mouse are larger than those from the unhealthy ones. For each individual dataset, the strains generated from the automatically tracked tagging lines are less stable than that from manually labeled ones, due to the tracking errors. The strains based on LDM are relatively smooth, but this method tends to underestimate the strains. The results from SDM-$L1$ have the worst stability because of its nature to pursue the sparsest solution. Since the control points contain both outliers and strong Gaussian noise, the $L1$ norm alone cannot handle Gaussian noise stably. The results from SDM-$L1/L2$ best match the reference strains. This shows that our model performs well in the LV motion tracking, even with inaccurate control points.

The LV strain is estimated on dense sample points. Based on these motion

results, strains at arbitrary positions inside the LV can be calculated by linear interpolation. In order to analyze the local heart motion properties, strains at the end of systole are projected onto short- and long-axis slices in Fig. 4.5. We show the radial, circumferential, and longitudinal strains on the LV in the MR images. The strains change smoothly in each slice. Generally, the lateral side has larger strain than the septal side. The reason is that the right ventricle motion restricts the septal side motion.

We also visualize the strains on the external and internal surfaces of the LV. Since the points of the surface mesh are all in the initial volume model, where the strains are calculated, we use them as samples and linearly interpolate the strains on the LV surface. The circumferential strains are shown locally on the LV external and internal surfaces in Fig. 4.6. They indicate larger contraction near the endocardium than the epicardium. The high strain area starts from the apical endocardium and expands quickly toward the base, which is similar to human hearts.

## 4.5 Conclusions

In this section, we introduce a group of sparse deformable models. Benefitted from the sparsity techniques, these deformable models are able to handle outliers or gross errors. Therefore, they are robust to deal with noisy images or tracking errors. We have validated these methods on both synthetic data and the mouse cardiac motion tracking. Both qualitative and quantitative results demonstrate that our methods outperform and are more robust than previous ones. It is also noteworthy that the applications of our proposed methods are not limited to cardiac motion analysis. It is flexible enough for many other medical image problems.

In the future, we plan to extend the deformable models by using structured

priors. The LV is conventionally separated into 17 segments. This inspires us to add group constraints to the current sparse model. The group sparsity and other structure sparsity constraints will further improve the robustness of the model. The current regularization term is only related to the external force based on noisy observations. It is also possible to extend the other parts of the model. The problem with modeling arbitrary internal forces is that the resulting model may not be a convex problem. The traditional finite difference method can be employed to find a local minimum, while the performance can then be further analyzed.

# Chapter 5
# Conclusions

In this thesis, we present a group of sparse methods for cardiac MRI reconstruction and analysis. These methods tackle several different problems from data acquisition to further image processing. The key idea among all the methods is exploiting the sparse properties inside the data. In the MRI reconstruction problem, the group sparse structure is identified and utilized to optimize the signals from multiple coils together. In the 3D LV model reconstruction problem, the sparse 2D slices with arbitrary orientations are combined to model a full 3D shape. In the LV motion tracking problem, the tracking error is regularized with sparse constraint due to the non-Gaussian distribution of tagging line tracking error. The sparseness is a key idea for many signal processing methods. It has already been widely used for data compression, signal reconstruction, and etc. The simplified sparse representation is a good way to explore the intrinsic property of the data. It is potentially to be used extensive in general data analysis.

The main challenge for utilizing sparse method comes from the following two aspects. First, how to identify the sparse properties of the data. Second, how to efficient solve the optimization problem based on the sparse properties. After a decade of development, the idea of sparseness is not limited to the number of non-zero terms. More studies focus on the relation and distribution of these non-zero terms. The structure sparsity is a more interesting problem, which further investigates the intrinsic data property. The additional property usually can further compress the data. Therefore, the sparseness of the data can be further considered

as the compressibility of the data. The extension of the problem definition makes it harder to be solved generally. The optimization problem for the naive sparse constraints have been studied for a long time. The simple structure sparse problems, like group sparse, also have suitable method to solve. However, the more general structure sparse problem, like the clustered sparse structure, may not have a good optimization method. More research is still needed to find good optimization algorithms for various sparse regularization problems.

The development of cardiac MRI poses a series of new problems for further research. They are dramatically different from conventional natural image processing in many aspects. The image presents the 2D slice inside the object instead of the surface. The signal is acquired from the k-space sampling instead of the image space. The MR image intensity naturally decay and blur along time following the property of magnetic field. All these properties open a new area for computer vision study. Therefore, we have proposed a group of algorithm to solve various problems. The sparse methods have been used in different ways to help solving these problems.

The sparse methods already have significant contribution to the recent development of MRI reconstruction and analysis. The study started from some surprising empirical observation, while it fast evolved into a complete research area with solid theoretical proof and wide clinical applications. It is a great pleasure to witness and participate the golden age of sparse method. After the introduction of compressed sensing theory, the related methods have been applied to nearly every application of computer vision and medical image analysis. The develop in recent years not only utilizes the advantage of sparse methods, but also discovers the drawback. This is the necessary process for a new method to become a common tool. In the further, although sparse methods may not be the super star for solving the new problems, they will still be a key component for many algorithms, which

explore the sparsity in some aspects. Like many established algorithms, the sparse methods will help developing more useful algorithms in the further.

# Bibliography

[1] T. Arts, F.W. Prinzen, T. Delhaas, J.R. Milles, A.C. Rossi, and P. Clarysse. Mapping displacement and deformation of the heart with local sine-wave modeling. *IEEE Transactions on Medical Imaging*, 29(5):1114–1123, may 2010. ISSN 0278-0062. 31, 46

[2] L Axel and L Dougherty. MR imaging of motion with spatial modulation of magnetization. *Radiology*, 171(3):841–845, 1989. 27

[3] Eric Bardinet, Laurent D. Cohen, and Nicholas Ayache. Tracking and motion analysis of the left ventricle with deformable superquadrics. *Medical Image Analysis*, 1(2):129–149, 1996. ISSN 1361-8415. doi: http://dx.doi.org/10.1016/S1361-8415(96)80009-0. 66

[4] A. Beck and M. Teboulle. Fast gradient-based algorithms for constrained total variation image denoising and deblurring problems. *IEEE Transactions on Image Processing*, 18(11):2419–2434, 2009. ISSN 1057-7149. doi: 10.1109/TIP.2009.2028250. 22

[5] Amir Beck and Marc Teboulle. A fast iterative shrinkage-thresholding algorithm for linear inverse problems. *SIAM Journal on Imaging Sciences*, 2(1):183–202, 2009. doi: 10.1137/080716542. 21

[6] T. Belytschko, Y. Krongauz, D. Organ, M. Fleming, and P. Krysl. Meshless methods: An overview and recent developments. *Computer Methods in Applied Mechanics and Engineering*, 139(1-4):3–47, 1996. ISSN 0045-7825. doi: 10.1016/S0045-7825(96)01078-X. 32

[7] C. Bilen, Yao Wang, and I.W. Selesnick. High-speed compressed sensing reconstruction in dynamic parallel MRI using augmented lagrangian and parallel processing. *IEEE Journal on Emerging and Selected Topics in Circuits and Systems*, 2(3):370–379, 2012. ISSN 2156-3357. doi: 10.1109/JETCAS.2012.2217032. 17

[8] Martin Blaimer, Felix Breuer, Matthias Mueller, Robin M Heidemann, Mark A Griswold, and Peter M Jakob. SMASH, SENSE, PILS, GRAPPA: How to choose the optimal method. *Topics in Magnetic Resonance Imaging*, 15(4):223–236, 2004. 17

[9] Y. Boykov, O. Veksler, and R. Zabih. Fast approximate energy minimization via graph cuts. *IEEE Transactions on Pattern Analysis and Machine Intelligence*, 23(11):1222–1239, 2001. ISSN 0162-8828. doi: 10.1109/34.969114. 41

[10] Yuri Boykov and Marie-Pierre Jolly. Interactive organ segmentation using graph cuts. In Scott L. Delp, Anthony M. DiGoia, and Branislav Jaramaz, editors, *Medical Image Computing and Computer-Assisted Intervention*, volume 1935 of *Lecture Notes in Computer Science*, pages 276–286. Springer Berlin Heidelberg, 2000. ISBN 978-3-540-41189-5. doi: 10.1007/978-3-540-40899-4_28. 41

[11] E.J. Candes, J. Romberg, and T. Tao. Robust uncertainty principles: exact signal reconstruction from highly incomplete frequency information. *IEEE Transactions on Information Theory*, 52(2):489–509, February 2006. ISSN 0018-9448. doi: 10.1109/TIT.2005.862083. 4, 12, 64, 74

[12] E.J. Candes and T. Tao. Decoding by linear programming. *IEEE Transactions on Information Theory*, 51(12):4203–4215, December 2005. ISSN 0018-9448. doi: 10.1109/TIT.2005.858979. 4, 12, 13, 65

[13] E.J. Candes and T. Tao. Near-optimal signal recovery from random projections: Universal encoding strategies? *IEEE Transactions on Information Theory*, 52(12):5406–5425, December 2006. ISSN 0018-9448. doi: 10.1109/TIT.2006.885507. 4, 65

[14] E.J. Candes and M.B. Wakin. An introduction to compressive sampling. *Signal Processing Magazine, IEEE*, 25(2):21–30, March 2008. ISSN 1053-5888. doi: 10.1109/MSP.2007.914731. 14

[15] Ernesto Castillo, Joao A. C. Lima, and David A. Bluemke. Regional myocardial function: Advances in MR imaging and analysis. *Radiographics*, 23:127–140, 2003. 27, 45

[16] Manuel D. Cerqueira, Neil J. Weissman, Vasken Dilsizian, Alice K. Jacobs, Sanjiv Kaul, Warren K. Laskey, Dudley J. Pennell, John A. Rumberger, Thomas Ryan, and Mario S. Verani. Standardized myocardial segmentation and nomenclature for tomographic imaging of the heart: A statement for healthcare professionals from the cardiac imaging committee of the council on clinical cardiology of the American heart association. *Circulation*, 105(4):539–542, 2002. ISSN 1071-3581. doi: 10.1067/mnc.2002.123122. 80

[17] R. Chandrashekara, R.H. Mohiaddin, and D. Rueckert. Analysis of 3-D myocardial motion in tagged MR images using nonrigid image registration. *Medical Imaging, IEEE Transactions on*, 23(10):1245–1250, 2004. ISSN 0278-0062. doi: 10.1109/TMI.2004.834607. 46

[18] Chen Chen, Yeqing Li, and Junzhou Huang. Calibrationless parallel MRI with joint total variation regularization. In Kensaku Mori, Ichiro Sakuma, Yoshinobu Sato, Christian Barillot, and Nassir Navab, editors, *Medical Image Computing and Computer-Assisted Intervention*, volume 8151 of *Lecture Notes in Computer Science*, pages 106–114. Springer Berlin Heidelberg, 2013. ISBN 978-3-642-40759-8. doi: 10.1007/978-3-642-40760-4_14. 17, 18, 24, 25

[19] Siqi Chen, Daniel Cremers, and Richard J. Radke. Image segmentation with one shape prior – A template-based formulation. *Image and Vision Computing*, 30(12):1032–1042, 2012. ISSN 0262-8856. doi: http://dx.doi.org/10.1016/j.imavis.2012.09.005. 37

[20] Ting Chen, J. Babb, P. Kellman, L. Axel, and D. Kim. Semiautomated segmentation of myocardial contours for fast strain analysis in cine displacement-encoded MRI. *IEEE Transactions on Medical Imaging*, 27(8):1084–1094, Aug 2008. ISSN 0278-0062. doi: 10.1109/TMI.2008.918327. 64

[21] Ting Chen, Xiaoxu Wang, Sohae Chung, Dimitris Metaxas, and Leon Axel. Automated 3D motion tracking using Gabor filter bank, robust point matching, and deformable models. *IEEE Transactions on Medical Imaging*, 29(1):1–11, 2010. 31, 46, 50

[22] Yasheng Chen and A.A. Amini. A MAP framework for tag line detection in SPAMM data using Markov random fields on the B-spline solid. *IEEE Transactions on Medical Imaging*, 21(9):1110–1122, 2002. ISSN 0278-0062. doi: 10.1109/TMI.2002.804430. 45

[23] J. S. Chuang, A. Zemljic-Harpf, R. S. Ross, L. R. Frank, A. D. McCulloch, and J. H. Omens. Determination of three-dimensional ventricular strain distributions in gene-targeted mice using tagged MRI. *Magnetic Resonance in Medicine*, 64(5):1281–1288, 2010. 31

[24] Cybèle Ciofolo and Maxim Fradkin. Segmentation of pathologic hearts in long-axis late-enhancement MRI. In Dimitris Metaxas, Leon Axel, Gabor Fichtinger, and Gábor Székely, editors, *Medical Image Computing and Computer-Assisted Intervention*, volume 5241 of *Lecture Notes in Computer Science*, pages 186–193. Springer Berlin Heidelberg, 2008. ISBN 978-3-540-85987-1. doi: 10.1007/978-3-540-85988-8_23. 36

[25] L.D. Cohen and I. Cohen. Finite-element methods for active contour models and balloons for 2-D and 3-D images. *IEEE Transactions on Pattern Analysis and Machine Intelligence*, 15(11):1131–1147, Nov. 1993. ISSN 0162-8828. 67

[26] T.F. Cootes, C.J. Taylor, D.H. Cooper, and J. Graham. Active shape models – Their training and application. *Computer Vision and Image Understanding*, 61(1):38–59, Apr. 1995. ISSN 1077–3142. 67

[27] John G. Daugman. Uncertainty relation for resolution in space, spatial frequency, and orientation optimized by two-dimensional visual cortical filters. *Journal of the Optical Society of America A*, 2(7):1160–1169, 1985. doi: 10.1364/JOSAA.2.001160. 47

[28] C. Davatzikos, Xiaodong Tao, and Dinggang Shen. Hierarchical active shape models, using the wavelet transform. *IEEE Transactions on Medical Imaging*, 22(3):414–423, 2003. ISSN 0278-0062. doi: 10.1109/TMI.2003.809688. 68

[29] D. L. Donoho. Compressed sensing. *IEEE Transactions on Information Theory*, 52(4):1289–1306, April 2006. ISSN 0018-9448. doi: 10.1109/TIT.2006.871582. 64

[30] L. Dougherty, J.C. Asmuth, A.S. Blom, L. Axel, and Rakesh Kumar. Validation of an optical flow method for tag displacement estimation. *IEEE Transactions on Medical Imaging*, 18(4):359–363, 1999. ISSN 0278-0062. doi: 10.1109/42.768845. 31, 46

[31] Qi Duan, Elsa D. Angelini, Susan L. Herz, Christopher M. Ingrassia, Kevin D. Costa, Jeffrey W. Holmes, Shunichi Homma, and Andrew F. Laine. Region-based endocardium tracking on real-time three-dimensional ultrasound. *Ultrasound in Medicine & Biology*, 35(2):256–265, 2009. ISSN 0301-5629. doi: http://dx.doi.org/10.1016/j.ultrasmedbio.2008.08.012. 67

[32] Qi Duan, Elsa D. Angelini, and Andrew F. Laine. Surface function actives. *Journal of Visual Communication and Image Representation*, 20(7):478 – 490, 2009. ISSN 1047-3203. doi: http://dx.doi.org/10.1016/j.jvcir.2009.06.002. 66

[33] Qi Duan, Elsa D. Angelini, and Andrew F. Laine. Real-time segmentation by active geometric functions. *Computer Methods and Programs in Biomedicine*, 98(3):223–230, 2010. ISSN 0169-2607. doi: http://dx.doi.org/10.1016/j.cmpb.2009.09.001. 66

[34] N. Duta and M. Sonka. Segmentation and interpretation of MR brain images: An improved active shape model. *IEEE Transactions on Medical Imaging*, 17(6):1049–1062, December 1998. ISSN 0278-0062. 67

[35] RR Edelman and S Warach. Magnetic resonance imaging. *The New England journal of medicine*, 328(11):785–791, March 1993. ISSN 0028-4793. doi: 10.1056/nejm199303183281109. 3

[36] Martin A. Fischler and Robert C. Bolles. Random sample consensus: A paradigm for model fitting with applications to image analysis and automated cartography. *Communications of the ACM*, 24(6):381–395, June 1981. ISSN 0001-0782. 68

[37] Maxim Fradkin, Cybele Ciofolo-Veit, Benoit Mory, Gilion Hautvast, and Marcel Breeuwer. Fully automatic segmentation of short and long axis cine cardiac MR. In *12th Annual SCMR Scientific Sessions*, volume 11 of *Journal of Cardiovascular Magnetic Resonance*. 2009. 36

[38] R. A. Gingold and J. J. Monaghan. Smoothed particle hydrodynamics: Theory and application to non-spherical stars. *Monthly Notices of the Royal Astronomical Society*, 181:375–389, 1977. 32

[39] M. Grant and S. Boyd. Graph implementations for nonsmooth convex programs. In V. Blondel, S. Boyd, and H. Kimura, editors, *Recent Advances in*

*Learning and Control*, Lecture Notes in Control and Information Sciences, pages 95–110. Springer-Verlag Limited, 2008. 77

[40] Mark A. Griswold, Peter M. Jakob, Robin M. Heidemann, Mathias Nittka, Vladimir Jellus, Jianmin Wang, Berthold Kiefer, and Axel Haase. Generalized autocalibrating partially parallel acquisitions (GRAPPA). *Magnetic Resonance in Medicine*, 47(6):1202–1210, 2002. ISSN 1522-2594. doi: 10.1002/mrm.10171. 21

[41] Sandeep N. Gupta and Jerry L. Prince. On variable brightness optical flow for tagged MRI. In Yves Bizais, Christian Barillot, and Robert Di Paola, editors, *Information Processing in Medical Imaging*, volume 3 of *Computational Imaging and Vision*, pages 323–334. Springer, 1995. ISBN 978-0-7923-3593-1. 46

[42] Idith Haber, Dimitris N Metaxas, and Leon Axel. Three-dimensional motion reconstruction and analysis of the right ventricle using tagged MRI. *Medical Image Analysis*, 4(4):335–355, 2000. 64

[43] Jun He, L. Balzano, and A. Szlam. Incremental gradient on the grassmannian for online foreground and background separation in subsampled video. In *IEEE Conference on Computer Vision and Pattern Recognition*, pages 1568–1575. 2012. ISSN 1063-6919. doi: 10.1109/CVPR.2012.6247848. 75

[44] GJ Heatlie and K Pointon. Cardiac magnetic resonance imaging. *Postgraduate medical journal*, 80(939):191–22, January 2004. ISSN 0032-5473. doi: 10.1136/pmj.2003.010355. 3

[45] Hidekata Hontani, Takamiti Matsuno, and Yoshihide Sawada. Robust nonrigid ICP using outlier-sparsity regularization. In *IEEE Conference on Computer Vision and Pattern Recognition*, pages 1025–1032. Jun. 2012. ISSN 1063-6919. 68

[46] Zhenhua Hu, Dimitris Metaxas, and Leon Axel. In vivo strain and stress estimation of the heart left and right ventricles from MRI images. *Medical Image Analysis*, 7(4):435–444, 2003. ISSN 1361-8415. doi: http://dx.doi.org/10.1016/S1361-8415(03)00032-X. Medical Image Computing and Computer Assisted Intervention. 64

[47] Junzhou Huang, Shaoting Zhang, and Dimitris Metaxas. Efficient MR image reconstruction for compressed MR imaging. *Medical Image Analysis*, 15(5):670 – 679, 2011. ISSN 1361-8415. doi: http://dx.doi.org/10.1016/j.media.2011.06.001. Special Issue on the 2010 Conference on Medical Image Computing and Computer-Assisted Intervention. 19

[48] Xiaojie Huang, Donald P. Dione, Colin B. Compas, Xenophon Papademetris, Ben A. Lin, Alda Bregasi, Albert J. Sinusas, Lawrence H. Staib, and James S.

Duncan. Contour tracking in echocardiographic sequences via sparse representation and dictionary learning. *Medical Image Analysis*, (0):–, 2013. ISSN 1361-8415. doi: http://dx.doi.org/10.1016/j.media.2013.10.012. 67

[49] Xiaojie Huang, Donald P. Dione, BenA. Lin, Alda Bregasi, Albert J. Sinusas, and James S. Duncan. Segmentation of 4D echocardiography using stochastic online dictionary learning. In Kensaku Mori, Ichiro Sakuma, Yoshinobu Sato, Christian Barillot, and Nassir Navab, editors, *Medical Image Computing and Computer-Assisted Intervention*, volume 8151 of *Lecture Notes in Computer Science*, pages 57–65. Springer Berlin Heidelberg, 2013. ISBN 978-3-642-40759-8. doi: 10.1007/978-3-642-40760-4_8. 67

[50] Xiaolei Huang and Dimitris N. Metaxas. Metamorphs: Deformable shape and appearance models. *IEEE Transactions on Pattern Analysis and Machine Intelligence*, 30(8):1444–1459, 2008. ISSN 0162-8828. doi: 10.1109/TPAMI.2007.70795. 67

[51] S. Jehan-Besson, M. Barlaud, G. Aubert, and O. Faugeras. Shape gradients for histogram segmentation using active contours. In *IEEE International Conference on Computer Vision*, pages 408–415 vol.1. 2003. doi: 10.1109/ICCV.2003.1238375. 67

[52] Michael Kass, Andrew Witkin, and Demetri Terzopoulos. Snakes: Active contour models. *International Journal of Computer Vision*, 1:321–331, Jan. 1988. ISSN 0920-5691. 64, 65, 67

[53] Juha Koikkalainen, Mika Pollari, Jyrki Lötjönen, Sari Kivistö, and Kirsi Lauerma. Segmentation of cardiac structures simultaneously from short- and long-axis MR images. In Christian Barillot, David R. Haynor, and Pierre Hellier, editors, *Medical Image Computing and Computer-Assisted Intervention*, volume 3216 of *Lecture Notes in Computer Science*, pages 427–434. Springer Berlin Heidelberg, 2004. ISBN 978-3-540-22976-6. doi: 10.1007/978-3-540-30135-6_52. 37

[54] K. Lekadir, R. Merrifield, and Guang-Zhong Yang. Outlier detection and handling for robust 3-D active shape models search. *IEEE Transactions on Medical Imaging*, 26(2):212–222, feb. 2007. ISSN 0278-0062. 67

[55] G. R. Liu. *Mesh Free Methods: Moving Beyond the Finite Element Method*. CRC Press, 2002. 32

[56] Jun Liu, Lei Yuan, and Jieping Ye. An efficient algorithm for a class of fused lasso problems. In *Proceedings of the 16th ACM SIGKDD International Conference on Knowledge Discovery and Data Mining*, pages 323–332. ACM, New York, NY, USA, 2010. ISBN 978-1-4503-0055-1. doi: 10.1145/1835804.1835847. 22

[57] Wei Liu, Marvin W. Ashford, Junjie Chen, Mary P. Watkins, Todd A. Williams, Samuel A. Wickline, and Xin Yu. MR tagging demonstrates quantitative differences in regional ventricular wall motion in mice, rats, and men. *American journal of physiology. Heart and circulatory physiology*, 291(5):2515–2521, 2006. 31

[58] M. Lustig, D.L. Donoho, J.M. Santos, and J.M. Pauly. Compressed sensing MRI. *IEEE Signal Processing Magazine*, 25(2):72–82, March 2008. ISSN 1053-5888. doi: 10.1109/MSP.2007.914728. 4

[59] Michael Lustig, David Donoho, and John M. Pauly. Sparse MRI: The application of compressed sensing for rapid MR imaging. *Magnetic Resonance in Medicine*, 58(6):1182–1195, 2007. ISSN 1522-2594. doi: 10.1002/mrm.21391. 4, 13, 19

[60] Michael Lustig and John M. Pauly. SPIRiT: Iterative self-consistent parallel imaging reconstruction from arbitrary k-space. *Magnetic Resonance in Medicine*, 64(2):457–471, 2010. ISSN 1522-2594. doi: 10.1002/mrm.22428. 21

[61] Angshul Majumdar and Rabab K. Ward. Calibration-less multi-coil MR image reconstruction. *Magnetic Resonance Imaging*, 30(7):1032–1045, 2012. ISSN 0730-725X. doi: http://dx.doi.org/10.1016/j.mri.2012.02.025. 18, 24, 25

[62] S.G. Mallat and Z. Zhang. Matching pursuits with time-frequency dictionaries. *IEEE Transactions on Signal Processing*, 41(12):3397–3415, 1993. ISSN 1053-587X. doi: 10.1109/78.258082. 74

[63] T. McInerney and D. Terzopoulos. Deformable models in medical image analysis. In *Proceedings of the Workshop on Mathematical Methods in Biomedical Image Analysis*, pages 171 –180. jun 1996. doi: 10.1109/MMBIA.1996.534069. 63

[64] D. Metaxas and D. Terzopoulos. Constrained deformable superquadrics and nonrigid motion tracking. In *IEEE Computer Society Conference on Computer Vision and Pattern Recognition*, pages 337–343. Jun 1991. ISSN 1063-6919. doi: 10.1109/CVPR.1991.139712. 64

[65] Dimitris Metaxas. *Physics-based modeling of nonrigid objects for vision and graphics*. Ph.D. thesis, University of Pennsylvania, 1992. 63

[66] Dimitris Metaxas and Demetri Terzopoulos. Shape and nonrigid motion estimation through physics-based synthesis. *IEEE Transactions on Pattern Analysis and Machine Intelligence*, 15(6):580–591, 1993. 64

[67] Dimitris N. Metaxas. *Physics-based deformable models: Applications to computer vision, graphics, and medical imaging*. Kluwer Academic Publishers, Norwell, MA, USA, 1st edition, 1996. ISBN 0792398408. 63

[68] Dariush Mozaffarian, Emelia J Benjamin, Alan S Go, Donna K Arnett, Michael J Blaha, Mary Cushman, Sarah de Ferranti, Jean-Pierre Desprs, Heather J Fullerton, Virginia J Howard, Mark D Huffman, Suzanne E Judd, Brett M Kissela, Daniel T Lackland, Judith H Lichtman, Lynda D Lisabeth, Simin Liu, Rachel H Mackey, David B Matchar, Darren K McGuire, Emile R Mohler, Claudia S Moy, Paul Muntner, Michael E Mussolino, Khurram Nasir, Robert W Neumar, Graham Nichol, Latha Palaniappan, Dilip K Pandey, Mathew J Reeves, Carlos J Rodriguez, Paul D Sorlie, Joel Stein, Amytis Towfighi, Tanya N Turan, Salim S Virani, Joshua Z Willey, Daniel Woo, Robert W Yeh, Melanie B Turner, and American Heart Association Statistics Committee and Stroke Statistics Subcommittee. Heart disease and stroke statistics–2015 update: a report from the american heart association. *Circulation*, 131(4):e29–322, January 2015. ISSN 0009-7322. doi: 10.1161/cir.0000000000000152. 1

[69] M. Müller, R. Keiser, A. Nealen, M. Pauly, M. Gross, and M. Alexa. Point based animation of elastic, plastic and melting objects. In *Proceedings of the 2004 ACM SIGGRAPH/Eurographics symposium on Computer animation*, SCA '04, pages 141–151. Eurographics Association, Aire-la-Ville, Switzerland, 2004. ISBN 3-905673-14-2. 53, 56

[70] Matthias Müller, David Charypar, and Markus Gross. Particle-based fluid simulation for interactive applications. In *Proceedings of the 2003 ACM SIGGRAPH/Eurographics symposium on Computer animation*, SCA '03, pages 154–159. Eurographics Association, Aire-la-Ville, Switzerland, Switzerland, 2003. ISBN 1-58113-659-5. 70

[71] A. Myronenko and Xubo Song. Point set registration: Coherent point drift. *IEEE Transactions on Pattern Analysis and Machine Intelligence*, 32(12):2262–2275, 2010. ISSN 0162-8828. 30, 34, 42

[72] B. Nayroles, G. Touzot, and P. Villon. Generalizing the finite element method: Diffuse approximation and diffuse elements. *Computational Mechanics*, 10(5):307–318, 1992. ISSN 0178-7675. doi: 10.1007/BF00364252. 32

[73] Andrew Nealen, Takeo Igarashi, Olga Sorkine, and Marc Alexa. Laplacian mesh optimization. In *Proceedings of the 4th international conference on Computer graphics and interactive techniques in Australasia and Southeast Asia*, GRAPHITE '06, pages 381–389. ACM, New York, NY, USA, 2006. ISBN 1-59593-564-9. doi: 10.1145/1174429.1174494. 71

[74] Andrew Nealen, Matthias Muller, Richard Keiser, Eddy Boxerman, and Mark Carlson. Physically based deformable models in computer graphics. *Computer Graphics Forum*, 25(4):809–836, 2006. ISSN 1467-8659. doi: 10.1111/j.1467-8659.2006.01000.x. 63, 64

[75] Nael F. Osman, William S. Kerwin, Elliot R. Mcveigh, and Jerry L. Prince. Cardiac motion tracking using CINE harmonic phase (HARP) magnetic resonance imaging. *Magnetic Resonance in Medicine*, 42:1048–1060, 1999. 46

[76] Nael F. Osman, Elliot R. McVeigh, and Jerry L. Prince. Imaging heart motion using harmonic phase MRI. *IEEE Transactions on Medical Imaging*, 19(3):186–202, 2000. ISSN 0278-0062. 31, 46

[77] R. Otazo, Li Feng, H. Chandarana, T. Block, L. Axel, and D.K. Sodickson. Combination of compressed sensing and parallel imaging for highly-accelerated dynamic MRI. In *9th IEEE International Symposium on Biomedical Imaging*, pages 980–983. 2012. ISSN 1945-7928. doi: 10.1109/ISBI.2012.6235721. 17

[78] Ricardo Otazo, Daniel Kim, Leon Axel, and Daniel K. Sodickson. Combination of compressed sensing and parallel imaging for highly accelerated first-pass cardiac perfusion MRI. *Magnetic Resonance in Medicine*, 64(3):767–776, 2010. ISSN 1522-2594. doi: 10.1002/mrm.22463. xi, 17, 18, 19, 23, 25

[79] N. Paragios. A level set approach for shape-driven segmentation and tracking of the left ventricle. *IEEE Transactions on Medical Imaging*, 22(6):773–776, June 2003. ISSN 0278-0062. doi: 10.1109/TMI.2003.814785. 68

[80] N. Paragios and R. Deriche. Geodesic active contours and level sets for the detection and tracking of moving objects. *IEEE Transactions on Pattern Analysis and Machine Intelligence*, 22(3):266–280, mar 2000. ISSN 0162-8828. doi: 10.1109/34.841758. 64

[81] Nikos Paragios. A variational approach for the segmentation of the left ventricle in cardiac image analysis. *International Journal of Computer Vision*, 50(3):345–362, 2002. ISSN 0920-5691. doi: 10.1023/A:1020882509893. 68

[82] Jinah Park, D. Metaxas, A.A. Young, and L. Axel. Deformable models with parameter functions for cardiac motion analysis from tagged MRI data. *IEEE Transactions on Medical Imaging*, 15(3):278–289, 1996. ISSN 0278-0062. doi: 10.1109/42.500137. 45

[83] Jinah Park, Dimitri Metaxas, and Leon Axel. Analysis of left ventricular wall motion based on volumetric deformable models and MRI-SPAMM. *Medical Image Analysis*, 1(1):53–71, 1996. 64

[84] Caroline Petitjean and Jean-Nicolas Dacher. A review of segmentation methods in short axis cardiac MR images. *Medical Image Analysis*, 15(2):169–184, 2011. ISSN 1361-8415. doi: http://dx.doi.org/10.1016/j.media.2010.12.004. 36

[85] Marcel Prastawa, Elizabeth Bullitt, Sean Ho, and Guido Gerig. A brain tumor segmentation framework based on outlier detection. *Medical Image Analysis*, 8(3):275–283, 2004. ISSN 1361-8415. doi: http://dx.doi.org/10.1016/j.media.2004.06.007. 67

[86] Klaas P. Pruessmann, Markus Weiger, Markus B. Scheidegger, and Peter Boesiger. Sense: Sensitivity encoding for fast MRI. *Magnetic Resonance in Medicine*, 42(5):952–962, 1999. ISSN 1522-2594. 16, 17

[87] P. Radau, Y. Lu, K. Connelly, G. Paul, A. Dick, and G. Wright. Evaluation framework for algorithms segmenting short axis cardiac MRI. *MICCAI Workshop: Cardiac MR Left Ventricle Segmentation Challenge*, 2009. 36

[88] Mike Rogers and Jim Graham. Robust active shape model search. In Anders Heyden, Gunnar Sparr, Mads Nielsen, and Peter Johansen, editors, *European Conference on Computer Vision*, volume 2353 of *Lecture Notes in Computer Science*, pages 289–312. Springer Berlin / Heidelberg, 2006. ISBN 978-3-540-43748-2. 68

[89] D. Rueckert, L.I. Sonoda, C. Hayes, D.L.G. Hill, M.O. Leach, and D.J. Hawkes. Nonrigid registration using free-form deformations: Application to breast MR images. *IEEE Transactions on Medical Imaging*, 18(8):712–721, 1999. 64

[90] C.E. Shannon. Communication in the presence of noise. *Proceedings of the IRE*, 37(1):10–21, Jan 1949. ISSN 0096-8390. doi: 10.1109/JRPROC.1949.232969. 7, 8

[91] Dinggang Shen and C. Davatzikos. HAMMER: Hierarchical attribute matching mechanism for elastic registration. *IEEE Transactions on Medical Imaging*, 21(11):1421–1439, 2002. ISSN 0278-0062. doi: 10.1109/TMI.2002.803111. 64

[92] Tian Shen, Xiaolei Huang, Hongsheng Li, E. Kim, Shaoting Zhang, and Junzhou Huang. A 3D Laplacian-driven parametric deformable model. In *IEEE International Conference on Computer Vision*, pages 279–286. Nov. 2011. ISSN 1550-5499. 66

[93] Wenzhe Shi, Xiahai Zhuang, Haiyan Wang, S. Duckett, D.V.N. Luong, C. Tobon-Gomez, KaiPin Tung, P.J. Edwards, K.S. Rhode, R.S. Razavi, S. Ourselin, and D. Rueckert. A comprehensive cardiac motion estimation framework using both untagged and 3-d tagged mr images based on non-rigid registration. *Medical Imaging, IEEE Transactions on*, 31(6):1263 –1275, june 2012. ISSN 0278-0062. doi: 10.1109/TMI.2012.2188104. 31

[94] Navid Shiee, Pierre-Louis Bazin, Jennifer L Cuzzocreo, Ari Blitz, and Dzung L Pham. Segmentation of brain images using adaptive atlases with application to ventriculomegaly. In *Information Processing in Medical Imaging*, pages 1–12. Springer, 2011. 68

[95] Peter J. Shin, Peder E. Z. Larson, Michael A. Ohliger, Michael Elad, John M. Pauly, Daniel B. Vigneron, and Michael Lustig. Calibrationless parallel imaging reconstruction based on structured low-rank matrix completion. *Magnetic Resonance in Medicine*, 72(4):959–970, 2014. ISSN 1522-2594. doi: 10.1002/mrm.24997. 18

[96] Daniel K. Sodickson and Warren J. Manning. Simultaneous acquisition of spatial harmonics (SMASH): Fast imaging with radiofrequency coil arrays. *Magnetic Resonance in Medicine*, 38(4):591–603, 1997. ISSN 1522-2594. doi: 10.1002/mrm.1910380414. 16

[97] O. Sorkine, D. Cohen-Or, Y. Lipman, M. Alexa, C. Rössl, and H.-P. Seidel. Laplacian surface editing. In *Proceedings of the 2004 Eurographics/ACM SIGGRAPH symposium on Geometry processing*, SGP '04, pages 175–184. ACM, 2004. ISBN 3-905673-13-4. 64, 65, 66, 74, 78

[98] Olga Sorkine and Marc Alexa. As-rigid-as-possible surface modeling. In *Proceedings of the fifth Eurographics symposium on Geometry processing*, pages 109–116. Eurographics Association, Aire-la-Ville, Switzerland, Switzerland, 2007. ISBN 978-3-905673-46-3. 56, 74

[99] Jasjit S Suri. Computer vision, pattern recognition and image processing in left ventricle segmentation: The last 50 years. *Pattern Analysis & Applications*, 3(3):209–242, 2000. ISSN 1433-7541. doi: 10.1007/s100440070008. 36

[100] D. Terzopoulos and D. Metaxas. Dynamic 3D models with local and global deformations: Deformable superquadrics. In *International Conference on Computer Vision*, pages 606–615. Dec. 1990. 66

[101] D. Terzopoulos and D. Metaxas. Dynamic 3D models with local and global deformations: Deformable superquadrics. *IEEE Transactions on Pattern Analysis and Machine Intelligence*, 13(7):703–714, Jul. 1991. ISSN 0162-8828. 67

[102] D. Terzopoulos, A. Witkin, and M. Kass. Constraints on deformable models: Recovering 3D shape and nonrigid motion. *Artificial Intelligence*, 36(1):91–123, 1988. 64

[103] Robert Tibshirani. Regression shrinkage and selection via the lasso. *Journal of the Royal Statistical Society. Series B (Methodological)*, 58(1):pp. 267–288, 1996. ISSN 00359246. 16

[104] J.A. Tropp and A.C. Gilbert. Signal recovery from random measurements via orthogonal matching pursuit. *Information Theory, IEEE Transactions on*, 53(12):4655–4666, 2007. ISSN 0018-9448. doi: 10.1109/TIT.2007.909108. 74

[105] N.J. Tustison and A.A. Amini. Biventricular myocardial strains via nonrigid registration of AnFigatomical NURBS models. *IEEE Transactions on Medical Imaging*, 25(1):94–112, Jan. 2006. ISSN 0278-0062. doi: 10.1109/TMI.2005.861015. 66

[106] Mehmet Üzümcü, Rob J. van der Geest, Milan Sonka, Hildo J. Lamb, Johan H. C. Reiber, and Boudewijn P. F. Lelieveldt. Multiview active appearance models for simultaneous segmentation of cardiac 2- and 4-chamber long-axis magnetic resonance images. *Investigative Radiology*, 40(4):195–203, 2005. 36

[107] Mustafa G. Uzunbas, Shaoting Zhang, Kilian M. Pohl, Dimitris Metaxas, and Leon Axel. Segmentation of myocardium using deformable regions and graph cuts. In *International Symposium on Biomedical Imaging: From Nano to Macro.*, pages 254–257. 2012. ISSN 1945-7928. doi: 10.1109/ISBI.2012.6235532. 33, 41, 42

[108] Hans C. van Assen, Mikhail G. Danilouchkine, Alejandro F. Frangi, Sebastián Ordás, Jos J. M. Westenberg, Johan H. C. Reiber, and Boudewijn P. F. Lelieveldt. SPASM: A 3D-ASM for segmentation of sparse and arbitrarily oriented cardiac MRI data. *Medical Image Analysis*, 10(2):286–303, 2006. ISSN 1361-8415. doi: http://dx.doi.org/10.1016/j.media.2005.12.001. 37

[109] Hui Wang and Amir A. Amini. Cardiac motion and deformation recovery from MRI: A review. *IEEE Transactions on Medical Imaging*, 31(2):487–503, 2012. ISSN 0278-0062. 28, 30, 45, 56, 64

[110] Xiaoxu Wang, Ting Chen, Shaoting Zhang, Dimitris Metaxas, and Leon Axel. LV motion and strain computation from tMRI based on meshless deformable models. In Dimitris Metaxas, Leon Axel, Gabor Fichtinger, and Gbor Szkely, editors, *International Conference on Medical Image Computing and Computer Assisted Intervention*, volume 5241 of *Lecture Notes in Computer Science*, pages 636–644. Springer Berlin / Heidelberg, 2008. ISBN 978-3-540-85987-1. xii, xiii, 57, 60, 61, 64, 78

[111] Xiaoxu Wang, D. Metaxas, Ting Chen, and L. Axel. Meshless deformable models for LV motion analysis. In *IEEE Conference on Computer Vision and Pattern Recognition*, pages 1–8. 2008. ISSN 1063-6919. 74

[112] Thomas P. Weldon, William E. Higgins, and Dennis F. Dunn. Efficient gabor filter design for texture segmentation. *Pattern Recognition*, 29(12):2005–2015, 1996. ISSN 0031-3203. doi: http://dx.doi.org/10.1016/S0031-3203(96)00047-7. 47

[113] Ken C.L. Wong, Linwei Wang, Heye Zhang, Huafeng Liu, and Pengcheng Shi. Meshfree implementation of individualized active cardiac dynamics. *Computerized Medical Imaging and Graphics*, 34(1):91–103, 2010. ISSN 0895-6111. doi: 10.1016/j.compmedimag.2009.05.002. 32

[114] J. Wright, A.Y. Yang, A. Ganesh, S.S. Sastry, and Yi Ma. Robust face recognition via sparse representation. *IEEE Transactions on Pattern Analysis and Machine Intelligence*, 31(2):210–227, 2009. ISSN 0162-8828. doi: 10.1109/TPAMI.2008.79. 75

[115] Chenyang Xu and Jerry L. Prince. Snakes, shapes, and gradient vector flow. *IEEE Transactions on Signal Processing*, 7(3):359–369, 1998. ISSN 1057–7149. doi: 10.1109/83.661186. 40

[116] Ping Yan, Albert Sinusas, and James S. Duncan. Boundary element method-based regularization for recovering of LV deformation. *Medical Image Analysis*, 11(6):540–554, 2007. ISSN 1361-8415. doi: http://dx.doi.org/10.1016/j.media.2007.04.007. 64

[117] Jianwei Yang, Lifeng Liu, Tianzi Jiang, and Yong Fan. A modified gabor filter design method for fingerprint image enhancement. *Pattern Recognition Letters*, 24(12):1805–1817, 2003. ISSN 0167-8655. doi: http://dx.doi.org/10.1016/S0167-8655(03)00005-9. 47

[118] A.A. Young, D.L. Kraitchman, L. Dougherty, and L. Axel. Tracking and finite element analysis of stripe deformation in magnetic resonance tagging. *IEEE Transactions on Medical Imaging*, 14(3):413–421, sep 1995. ISSN 0278-0062. 30

[119] Alistair A. Young, Brent A. French, Zequan Yang, Brett R. Cowan, Wesley D. Gilson, Stuart S. Berr, Christopher M. Kramer, and Frederick H. Epstein. Reperfused myocardial infarction in mice: 3D mapping of late gadolinium enhancement and strain. *Journal of Cardiovascular Magnetic Resonance*, 8(5):685–692, 2006. 31

[120] Yang Yu, Jingjing Liu, Dimitris Metaxas, and Leon Axel. 3d mouse left ventricle reconstruction using sparse mr images with arbitrary orientations. In *Second International Workshop on Sparsity Techniques in Medical Imaging*. 2014. v

[121] Yang Yu, Shaoting Zhang, Junzhou Huang, Leon Axel, and Dimitris Metaxas. Sparse deformable models. In *IEEE 10th International Symposium on Biomedical Imaging*. 2013. v

[122] Yang Yu, Shaoting Zhang, Junzhou Huang, Dimitris Metaxas, and Leon Axel. Sparse deformable models with applications to mouse lv motion analysis using tagged mri. In *First International Workshop on Sparsity Techniques in Medical Imaging*. 2012. v

[123] Yang Yu, Shaoting Zhang, Junzhou Huang, Dimitris Metaxas, and Leon Axel. Sparse deformable models with application to cardiac motion analysis. In James C. Gee, Sarang Joshi, Kilian M. Pohl, William M. Wells, and Lilla Zöllei, editors, *Information Processing in Medical Imaging*, volume 7917 of *Lecture Notes in Computer Science*, pages 208–219. Springer Berlin Heidelberg, 2013. ISBN 978-3-642-38867-5. doi: 10.1007/978-3-642-38868-2_18. v

[124] Yang Yu, Shaoting Zhang, Junzhou Huang, Dimitris Metaxas, and Leon Axel. Sparse deformable models with application to cardiac motion analysis. In *Information Processing in Medical Imaging*, pages 208–219. Springer, 2013. 65

[125] Yang Yu, Shaoting Zhang, Kang Li, Dimitris Metaxas, and Leon Axel. Deformable models with sparsity constraints for cardiac motion analysis. *Medical Image Analysis*, 18(6):927–937, 2014. ISSN 1361–8415. doi: http://dx.doi.org/10.1016/j.media.2014.03.002. Sparse Methods for Signal Reconstruction and Medical Image Analysis. v

[126] Yang Yu, Shaoting Zhang, Zhennan Yan, Song Chen, Rong Zhou, and D. Metaxas. Mouse lv 3d motion and strain analysis using tagged mri. In *IEEE 10th International Symposium on Biomedical Imaging*, pages 1190–1193. April 2013. ISSN 1945-7928. doi: 10.1109/ISBI.2013.6556693. v

[127] E A Zerhouni, D M Parish, W J Rogers, A Yang, and E P Shapiro. Human heart: tagging with MR imaging – a method for noninvasive assessment of myocardial motion. *Radiology*, 169(1):59–63, 1988. 27

[128] Shaoting Zhang, Yiqiang Zhan, Maneesh Dewan, Junzhou Huang, Dimitris N. Metaxas, and Xiang Sean Zhou. Towards robust and effective shape modeling: Sparse shape composition. *Medical Image Analysis*, 16(1):265–277, 2012. ISSN 1361-8415. doi: http://dx.doi.org/10.1016/j.media.2011.08.004. 37

[129] Shaoting Zhang, Yiqiang Zhan, Maneesh Dewan, Junzhou Huang, Dimitris N. Metaxas, and Xiang Sean Zhou. Towards robust and effective shape modeling: Sparse shape composition. *Medical Image Analysis*, 16(1):265–277, 2012. ISSN 1361-8415. 68, 75

[130] Shaoting Zhang, Yiqiang Zhan, and Dimitris N. Metaxas. Deformable segmentation via sparse representation and dictionary learning. *Medical Image Analysis*, 16(7):1385 – 1396, 2012. 68

[131] Jia Zhong, Wei Liu, and Xin Yu. Characterization of three-dimensional myocardial deformation in the mouse heart: An MR tagging study. *Journal of Magnetic Resonance Imaging*, 27(6):1263–1270, 2008. 31, 35, 52

[132] Kun Zhou, Jin Huang, John Snyder, Xinguo Liu, Hujun Bao, Baining Guo, and Heung-Yeung Shum. Large mesh deformation using the volumetric graph laplacian. *ACM Transactions on Graphics*, 24(3):496–503, July 2005. ISSN 0730-0301. doi: 10.1145/1073204.1073219. 64

[133] Rong Zhou, Stephen Pickup, Jerry D. Glickson, Craig H. Scott, and Victor A. Ferrari. Assessment of global and regional myocardial function in the mouse using cine and tagged MRI. *Magnetic Resonance in Medicine*, 49(4):760–764, 2003. 27, 31, 60

[134] Song-Chun Zhu and A. Yuille. Region competition: Unifying snakes, region growing, and Bayes/MDL for multiband image segmentation. *IEEE Transactions on Pattern Analysis and Machine Intelligence*, 18(9):884–900, 1996. ISSN 0162-8828. doi: 10.1109/34.537343. 67